Fall 2016

Development of Autonomous Surface Vessels for Hydrographic Survey Applications

Damian Manda
University of New Hampshire, Durham

DEVELOPMENT OF AUTONOMOUS SURFACE VESSELS FOR HYDROGRAPHIC SURVEY APPLICATIONS

BY

DAMIAN MANDA

BS, University of Colorado, 2010

THESIS

Submitted to the University of New Hampshire

in Partial Fulfillment of the Requirements for the Degree of

Master of Science

in

Ocean Engineering, Ocean Mapping

September, 2016

This thesis has been examined and approved in partial fulfillment of the requirements for the degree of Master of Science in Ocean Engineering by:

Thesis Director, Dr. May-Win Thein,
Associate Professor of Mechanical Engineering
and Ocean Engineering

Andy Armstrong,
Co-Director, Joint Hydrographic Center
Affiliate Professor of Ocean Engineering
and Marine Sciences and Earth Sciences

Dr. Martin Renken,
Lead Engineer, Naval Undersea Warfare Center

on 5/12/2016.

Original approval signatures are on file with the University of New Hampshire Graduate School.

ACKNOWLEDGEMENTS

The author would like to thank the Naval Engineering Education Consortium for financial support of this research project over the past 2 years. The NOAA Office of Coast Survey has provided general funding for Mr. Manda's degree and the ability to pursue the program at the University of New Hampshire. The NOAA Office of Unmanned Systems provided the EMILY vehicle for use in field testing. The NOAA Hydrographic Systems and Technologies Branch (HSTB) provided resources for the purchase of a sonar system for installation on the EMILY vehicle to be used in testing the path planning. Without this support, many aspects of this research would not have been possible.

The author would also like to thank the crew of NOAA Ship *Thomas Jefferson* and Teledyne Oceanscience for providing time and resources to allow experimentation on multiple Z-Boat platforms. In addition to the assistance provided by the thesis committee, UNH Center for Coastal and Ocean Mapping research scientist Val Schmidt and research project engineer Andy McLeod were integral to successful Z-Boat deployments at UNH and provided valuable feedback for the research at many opportunities.

The constant support, feedback and guidance of thesis director Dr. May-Win Thein facilitated the completion of this ambitious research. The opportunity as her student to attend conferences, mentor undergraduates and collaborate with others in the field were greatly appreciated and led to additional insight into the academic process and ocean engineering field outside the classroom environment.

TABLE OF CONTENTS

LIST OF TABLES

LIST OF FIGURES

LIST OF SYMBOLS

τ_m — Time constant of modeled heading system (s)

τ_s — Time constant of vessel for reaching steady-state rate of turn (s)

K_{pm} — Proportionality constant of modeled heading system (unitless)

K_s — Proportionality constant of vessel between rate of turn and rudder angle (unitless)

δ — Rudder angle ($^\circ$)

ψ_m — Heading of the modeled system ($^\circ$)

ψ_r — Desired heading when making a turn (deg)

ψ_p — Heading of the vessel (measured) (deg)

$\dot{\psi}$ — Heading rate-of-turn (ROT), how quickly the vessel is turning

ζ — Damping ratio, a factor governing overshoot in a system response (unitless)

ω_n — Natural frequency of a system (rad/s)

L — Length of a vessel (m)

U — Speed of a vessel (m/s)

$\mathbf{I}$ — The identity matrix.

ABSTRACT

DEVELOPMENT OF AUTONOMOUS SURFACE VESSELS FOR HYDROGRAPHIC SURVEY APPLICATIONS

by

Damian Manda

University of New Hampshire, September 2016

Autonomously navigating surface vessels have a variety of potential applications for ocean mapping. The use of small vessels for coastal mapping is investigated through development of hardware and software that form a complete system for survey operations. The hardware is selected to minimize cost while providing flexibility for installation on different platforms. MOOS-IvP open-source autonomy software enables independent operation of the vessel and provides for human monitoring. Custom applications allow the sensors and actuators of the hardware platforms to interface with MOOS-IvP.

An autonomy behavior is developed that replicates current human driven survey acquisition, in which the boat plans paths automatically to achieve full survey coverage with a swath sonar system. With initial input of a survey boundary and depths from the onboard sonar system, subsequent paths are planned to be offset based on the collected data. This behavior is tested in simulation and field experiments.

A model reference adaptive control system for the heading of the vessel is investigated for improved reliability of vessel operation in a variety of conditions and over the full range of operation speeds. Simulations tests verify the adaptation of two types of controllers. A new method for speed control to increase endurance and decrease engine wear is also proposed and simulated.

Together, these developments form an easily configurable system that provides automated hydrographic survey capability to a vessel with minimal human involvement for optimal performance.

INTRODUCTION

Marine vessels were one of the first applications of both unmanned systems and automated control. Their operation in less constrained environments than on land, but with simpler design requirements than aerial vehicles led to early experiments. Some of the first took place in the 1860's with developments of rudimentary torpedoes [3] and steam based ship steering systems [4]. The development of the North-seeking electronic gyrocompass in 1908 and spreading application of powered steering mechanisms spurred advancement in the development of control systems, and Sperry patented the first widely used automated controller in 1911 [4]. Minorsky improved the operation of these controllers, developing an early form of the Proportional, Integral, Derivative (PID) controllers used in many applications today [5].

Subsequent advances were driven by military applications, including target drones and minesweeping vessels [6]. All of these vessels were unmanned and could follow commands either from a plan or remote control, but did not have decision based behavior capabilities. Throughout this period, automated heading control for long transits became widespread and was available on most commercial and research vessels, where the headings were selected by the officers of the watch. Modern large ship autopilots remain very similar in capability to these early models, being able to follow tracks and headings but not assimilate other information and react to a changing environment. Dynamic positioning systems installed on vessels with the need to accurately station keep improve the positioning capability beyond heading, but still follow human directed plans.

The first truly autonomous surface vessels (ASVs) emerged in the late 1980s and early 1990s with the introduction of GPS positioning. The *Owl* vessels designed for the US Navy by companies that later became Navtec Inc. are often cited as the first operationally deployed ASV [3], [6]. These vessels were jet ski to small Rigid Hull Inflatable type boats with onboard sensing and navigation systems and have been mimicked by many other efforts leading into the present day. However,

the situational awareness, ability to complete complex missions and operational robustness only marginally improved until the early 2010s [3]. Recent work in autonomous land vehicles and aircraft allow them to operate for long periods of time in complex situations without human guidance, but marine vehicles have not received as much attention. This is potentially because of the same reasons that made early development more simple, the operation space is less constrained than in land navigation, but must remain on a single vertical surface. In addition, most interactions are unstructured and human mariners often negotiate passing arrangements contrary to the international standard Collision Regulations (COLREGS).

Until the early 2010s, most unmanned systems outside the Navy were isolated research efforts. In recent years, a number of commercial ASV manufacturers have begun producing models for applications in the oil and gas industry, environmental monitoring and seafloor mapping. Examples of these include the up to 7 m, diesel powered C-Worker produced by ASV Global [7] and the smaller, battery powered Teledyne Oceanscience Z-Boat 1800 [8]. Other vessels target long duration deployment, such as the Liquid Robotics Wave Glider [9] and the Saildrone [10]. These vessels can be delivered as a ready-to-run package with integrated sensing systems, path following autonomy and operator interfaces. The Saildrone and Wave Glider are designed to operate for indefinite periods of time, and therefore contain redundant, fault tolerant systems for long duration autonomy.

In addition to vessel advancements, the ecosystem necessary to fit autonomous vessels into marine operations have been subject to recent developments. Many research efforts have targeted vessels enacting COLREGS compliant maneuvers, using a variety of methods including multi-objective optimization [11], velocity obstacles [12], 4D space models [13] and fuzzy logic [14]. The infrastructure necessary to support navigation of many vessels is being investigated through projects like the Sea Traffic Management validation study by the European Union and Swedish Maritime Administration [15]. Large companies such as Rolls Royce are also beginning to expand on their visions of where these projects could evolve in the future, with centralized control of an autonomous vessel fleet [16].

For hydrographic surveying, autonomous underwater vehicles (AUVs) were introduced in the 1990s and became more feasible for routine surveys in the following decade. AUVs take advantage of submergence to survey closer to the seafloor and are more decoupled from surface conditions than traditional marine vessels, but still have major limitations in positioning and operational endurance and are typically very expensive as a result of the additional engineering burden for submerged vehicles. Many of these costs and concerns can be greatly reduced through the use of small autonomous surface vessels. Global Navigation Satellite System (GNSS) reception allows for cheaper navigation systems, hull sealing only needs to withstand wave action, and absolute reliability in operation is not paramount since the vessel can still be recovered if it malfunctions or is depleted of power. Air breathing gasoline or diesel engines or generators facilitate improved operating time and batteries can be much more easily swapped than with a pressure sealed hull.

For these reasons, increased interest in the use of ASVs for survey operations has led to a need software that allows flexible configuration and deployment in the field. In addition to the general maritime ecosystem and situational advancements, hydrography requires specialized navigation and path planning in order to map the seafloor to desired levels of coverage. Previous work on path planning mostly focuses on either filling areas with parallel lines, which can be fixed spacing such as in Hodo et al [17] or divided into regions based on depth such as in Galceran and Carreras [18]. These methods involve prior knowledge of the depths and obstacles within the survey region to function correctly. Methods targeting previously uncharacterized areas have been developed for single beam surveys by Wilson and Williams [19] and swath sonar surveys by Bourgeois [1]. These approaches enable the vessel to automatically respond to detected depths while surveying, allowing less human preparation time for deployment and more flexible use. This type of path planning was used as the basis for this research.

This research creates a system that is capable of converting any surface vessel for use in autonomous operations, and is customized for a number of small vessels. An autonomy system is implemented that allows basic operation in a variety of behaviors. A hydrographic survey path planning algorithm is implemented that achieves full coverage in previously unsurveyed regions.

In order to accurately follow the paths, an adaptive control system is developed that improves performance in wave and current conditions over traditional PID control.

CHAPTER 1

VESSEL HARDWARE AND ELECTRONICS

The hardware underlying the autonomous control system consists of primarily commercially available components that interact to make navigation decisions and drive the control surfaces of the ASV. Variants of this hardware are currently being used by multiple parallel development efforts at the University of New Hampshire for implementation on different research ASVs, as well as on NOAA's commercially produced ASVs. This rapid duplication and integration is made possible by the low-cost, mass-produced availability and the flexibility of the hardware system for interfacing with a variety of devices. Two major versions are implemented for this research. One is a full system capable of interfacing with low level hardware and providing monitoring and manual control capabilities, while the other is designed to add autonomy to vessels with existing remote control survey infrastructure.

1.1 Vessels

Two models of small commercially produced ASVs were specifically targeted for the autonomy retrofit in this research. In addition to these installations, versions of the hardware system were installed on two boats as part of undergraduate senior projects. These vessels were used to test some autonomy and control algorithms for this research, and demonstrate the simultaneous operation of multiple vessels.

1.1.1 Hydronalix Hurricane EMILY

The Hurricane EMILY vessel is based on the Hydronalix EMILY surf rescue boat, a remote controlled life buoy that can be deployed at beaches and rivers. The Hurricane version is designed

for data collection on the ocean surface from within a hurricane, and therefore has multiple sealed compartments, can self-right if flipped, and contains a gasoline engine for long duration missions [20]. Ten vessels of this type were produced for the NOAA Unmanned Aerial Systems program, of which one is used in this research for the purpose of designing a customizable autonomous system.

The EMILY vessel is 1.6 m long by 0.4 m wide, and can be carried and deployed by two people. Propulsion is provided by a waterjet driven by the two stroke gas engine, which has an electric starter system powered by a dedicated 12 V lead acid battery. Electronics are powered separately by a Lithium Polymer (Li-Po) battery pack consisting of four individual 5000 mAh, 14.8 V packs. The stock Hurricane EMILY contains a basic autonomy system that can navigate between waypoints and transfer data to a shoreside terminal using the Cloud Cap Techonology Piccolo commercial autonomy system. This, along with electronics to support the environmental sensors is housed in a water-resistant enclosure that is replaced by the system described in Section 1.2. Hurricane EMILY contains sensors for wind speed and direction, air and water temperature and barometric pressure. This data is stored onboard using a single board Gumstix computer and can be transmitted periodically over an Iridium Short Burst Data connection. The EMILY vessel is shown in Figures 1.1 and 1.2.

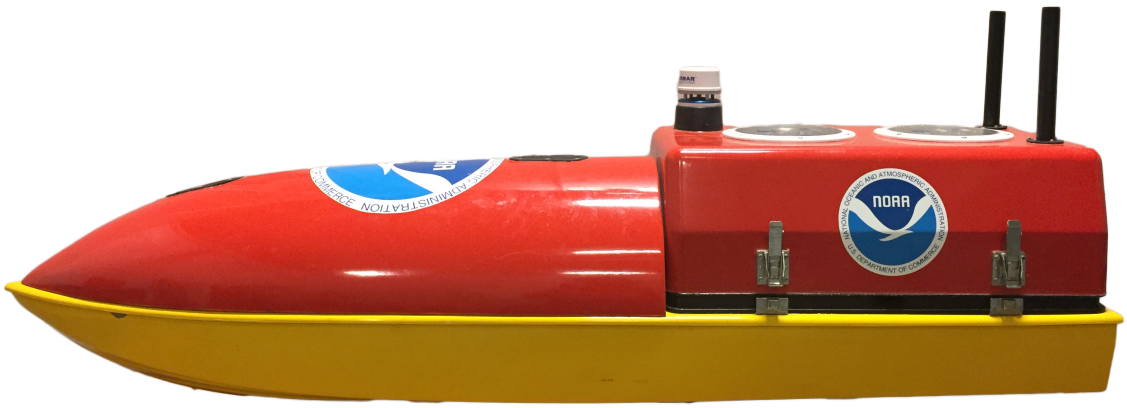

Figure 1.1: Profile view of Hurricane EMILY vessel.

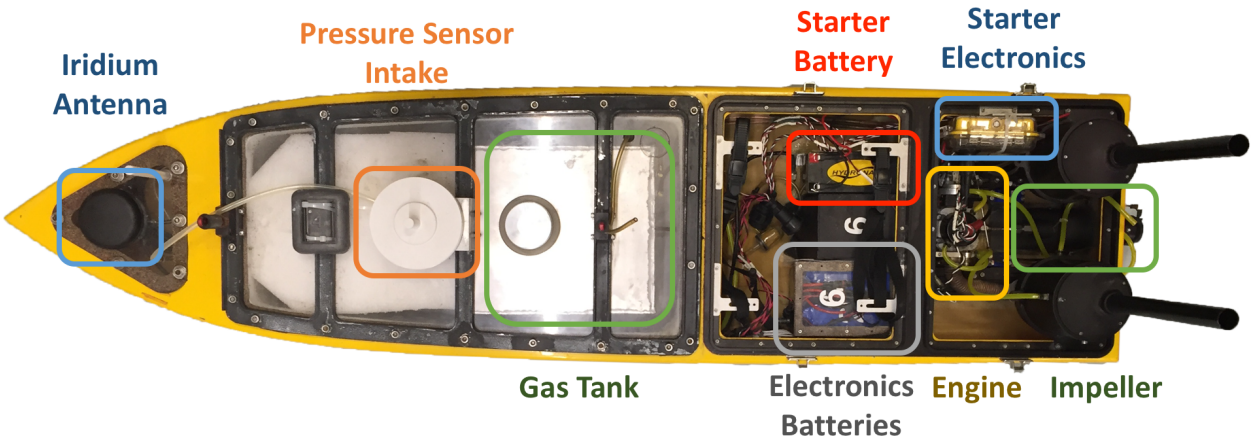

Figure 1.2: Overhead view of Hurricane EMILY vessel with covers removed, showing location of components. Autonomy control box fits in compartment above batteries, secured with the straps shown.

1.1.2 Teledyne OceanScience Z-Boat 1800

The Teledyne OceanScience Z-Boat 1800 is a small ASV designed for underwater data collection with sonar systems. Several variants are produced, including a rugged 1800-RP version designed to fit the needs of the NOAA Ship *Thomas Jefferson* and a custom manufacturer demo model outfitted with a multibeam sonar system that are used in this research.

The Z-Boat is 1.8 m long by 0.9 m wide vessel that weighs up to 68 kg in the rugged configuration [8], [21]. It is propelled by two external electric brushless motor thrusters, which are actuated to provide turning. The internal hardware consists of modules providing different functionality, including a central Command and Control Module (CCM), data and wireless transfer switch, onboard computing and sonar processing. This modular system allows flexibility in configuration and the boat can be operated in a remote control mode with only the CCM. Power for all system components and the thrusters is provided by 24 V lithium ion or nickel metal hydride battery packs. A *Thomas Jefferson* Z-Boat 1800-RP is shown in Figure 1.3.

The Z-Boat can store simple sonar data onboard, record it with hydrographic sofware when equipped with the onboard computing module, or transfer the data back to shore over a wireless connection that provides a range up to 1500 m. The *Thomas Jefferson* Z-Boats are equipped with Teledyne Odom CV-100 single beam sonar systems, and the multibeam Z-Boat used in this

Figure 1.3: Profile view of Z-Boat 1800-RP.

research contains a Teledyne Odom MB1 sonar. The sonars are configured and operated over the wireless data link. The multibeam Z-Boat is shown in Figure 1.4. Note that this version does not have the rugged antenna mounts or hatch covers of the 1800-RP model.

Figure 1.4: Custom multibeam demo Z-Boat for Teledyne OceanScience.

For positioning information, the *Thomas Jefferson* Z-Boats use a Trimble SPS-461 dual antenna GNSS receiver, while the multibeam Z-Boat uses a Hemisphere H320 OEM dual GNSS solution.

Both systems are capable of improving positioning with RTK correctors, which can be transferred over Wi-Fi or cell connections.

1.1.3 UNH Developed ASVs

During development of the retrofit hardware of Section 1.2, three vessels were constructed or modified for autonomous operation by undergraduate senior project teams. The first vessel was completely constructed at UNH. This vessel did not operate successfully, but allowed initial experimentation with some of the hardware later used in this research.

A second vessel (ASV2) used the hull and propulsion system from an Atomik Racing Catamaran hobby RC boat. This vessel is 1.4 m long by 0.4 m beam and has a mass of 6 kg before modifications. The retrofit system uses the most of the hardware configuration from the full system of Section 1.2, but the positioning is provided by an Adafruit Ultimate GPS unit and orientation by a SparkFun 9 DOF Razor IMU. With the exception of the GPS and Wi-Fi antennas and IMU, the hardware is contained in the cockpit portion toward the stern of the vessel. ASV2 is shown in Figure 1.5.

Figure 1.5: Undergraduate ASV2, including mast for antennas.

The largest vessel used in this research is a retrofit of a 2.9 m long by 1.2 m beam Bass Hunter EX catamaran style fishing boat [22]. This boat has a mass of 61 kg unloaded, which allows two or three people to handle deployment. The boat was retrofit with a feedback steering system, controllable propulsion through H-Bridges and the capability for human remote control or autonomous

operation [23]. The autonomy is provided through the same hardware as ASV2, with the addition of an Arduino Mega 2560 to monitor the steering system and a garage door style remote transmitter for switching between human and autonomous control. ASV3 is shown in Figure 1.6.

Figure 1.6: Undergraduate ASV3, in storage configuration with propulsion and sonar systems retracted.

ASV3 is large enough to fit a human passenger, which can help monitor the systems during autonomous testing. This is shown in the underway example in Figure 1.7.

Figure 1.7: Undergraduate ASV3, underway for sonar data collection with the author aboard.

1.2 Full Retrofit System

The complete system is designed to add autonomy and remote human control capability to any existing vessel that provides a mechanism for propulsion and steering control. It is designed to interface with the Hurricane EMILY ASV as well as hobby radio control (RC) boat kits. This system contains all of the components necessary for both the vessel and a shore or ship station used to monitor the operation remotely.

1.2.1 Processing and Autonomy Execution

The Mission Oriented Operating System with Interval Programming Helm (MOOS-IvP) autonomy software and supporting applications forming the core of the system can run most modern Unix based operating systems (Linux variants and Mac OS X). This software is discussed further in Chapter 2. For the integrated package, a compact, low cost, and low power draw device is most desirable for the target small vessels. A BeagleBone Black embedded Linux computer was initially selected for this role but later replaced by the higher performance Raspberry Pi 2 Model B (RPi2) after its release. The RPi2 (Figure 1.8a) is selected for this project due to its low cost ($35), large development community and ability to run Ubuntu Linux. The RPi2 contains a quad core 900 MHz Arm Cortex-A7 (ARMv7) architecture processor and 1 GB of RAM. All permanent data storage is located on a removable MicroSD memory card, which can be duplicated for rapid development of multiple command modules. The RPi2 can communicate externally with integrated Ethernet, 4 USB 2.0 ports, and a header providing 3.3 V TTL serial, SPI and I2C capability [24]. These protocols permit native integration with a wide variety of sensors and data transfer to other networked computers for monitoring and command interfaces. Since the initial development, the Raspberry Pi Foundation has released a Raspberry Pi 3 Model B, which increases the processing capability and adds built in WiFi and Bluetooth connectivity, but maintains the same cost. The Raspberry Pi 3 can be a drop in replacement for the RPi2 used during testing, serving to further increase processing power and system capabilities.

Multiple versions of Linux designed for ARM computers are available for the RPi2. For this project, Ubuntu 14.04 is chosen, which uses the 3.18 Linux kernel for the current RPi2 version. This was the latest long term service release at the time of initial development, and therefore provided best compatibility with third party programs and drivers. Selection of a mainstream Linux distribution simplifies compatibility with applications and drivers and increases the ease of transitioning the developed autonomy system to other platforms that support Ubuntu or Debian Linux based operating systems. The switch from initial development on the BeagleBone Black benefited from this ability to use the same operating system on both devices.

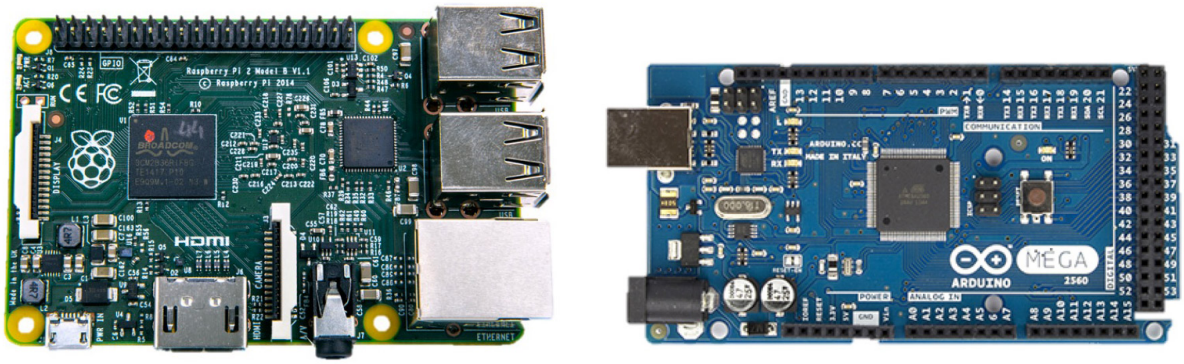

(a) Raspberry Pi 2 (b) Arduino Mega 2560

Figure 1.8: Autonomy processing computer and microcontroller

A separate microcontroller is chosen to interact with the physical systems on the boat and interpret human remote control input. Since a dedicated microcontroller is more suitable for timing sensitive tasks, such as Pulse Width Modulation (PWM) output and pulse length detection, this choice enables robust operation without interference from processor intensive autonomy determinations. The Arduino Mega 2560 (Figure 1.8b) was selected as the microprocessor platform due to existing usage within the University of New Hampshire, the large community of Arduino developers, an operating voltage of 5 V for broad compatibility, and the capability to natively handle more serial data streams and interrupts than other Arduino platforms. The Mega 2560 uses an Atmel ATmega2560 processor running at 16 MHz and has 4 serial UARTs, up to 15 PWM outputs, and 6 hardware interrupts. It also supports communication with other devices via SPI and I2C as well as

many analog and digital inputs [25]. While the full I/O capacity is not used in the applications of this thesis, it provides additional flexibility for future complex integrations.

The RPi2 communicates autonomy commands with the Arduino via a USB connection and can accept input from sensors interfaced with the Arduino to provide feedback for control systems and autonomous decisions. The PWM outputs allow the driving of stepper and servo motors, and interrupts are used for timing of pulse length input from a hobby RC receiver. In EMILY, two waterproof hobby servos are used to control the throttle of a gas engine and output nozzle angle of a jet drive system (the rudder). The same configuration is also implemented with an electronic speed controller and servo actuated rudder on hobby RC boats.

1.2.2 Wireless Communication

The retrofit autonomy system is designed to be a complete package for operation of a surface vessel, so remote control and data transfer functionality is necessary in addition to the on-vessel control hardware. Long distance Wi-Fi is used for communication between the autonomy system and a shore or ship-based monitoring station. The choice of the widespread 802.11n protocol for wireless transfer allows for the use of consumer equipment, and although output power is then limited to 1 W, this provides a sufficient range for communication within line of sight. The standard Wi-Fi also allows laptops to connect to the base station with their built in hardware, simplifying monitoring from multiple computers. The ASV has a 5 dBi omnidirectional antenna for a wider beam width to allow reliable connections with possible vehicle dynamics, while the more stationary shore station antenna has a 12 dBi omnidirectional antenna. This means that the signal from vehicle to shore is likely to be lost first, allowing the vehicle to still be commanded back into range when the return signal starts to fail. If additional range performance is desired where the wave conditions are anticipated to be calm, a 10 dBi gain antenna is interchangeable for use on the ASV.

The implemented system uses a Ubiquiti Bullet BM5HP 802.11n (Figure 1.10a) capable USB Wi-Fi adapter for the ASV and shore station. The Bullet has an Ethernet interface which simplifies

connection to the RPi2 and is found to provide a more reliable connection than USB based alternatives due to the Bullet itself managing the connection versus the operating system driver. This also allows other Ethernet capable devices, such as sonar systems, to pass data directly over the connection to shore. The shore station can be any available Mac or Linux computer using another Bullet configured as an access point. The autonomy system can also connect to infrastructure Wi-Fi networks for testing in the office or research environment. Wi-Fi radios operating at 5 GHz are chosen to reduce the possibility for interference with the 2.4 GHz human control radios described later in this chapter.

Tests range performance of the wireless communication system were conducted on land between the shore station with an antenna height of 3 m and a roving laptop to simulate the vessel with an antenna height of about 1.5 m. The higher gain 10 dBi antenna was used for the roving station. The results are presented in Figure 1.9, were the speeds are seen to reduce with distance until the signal is lost around 700 m from the base station.

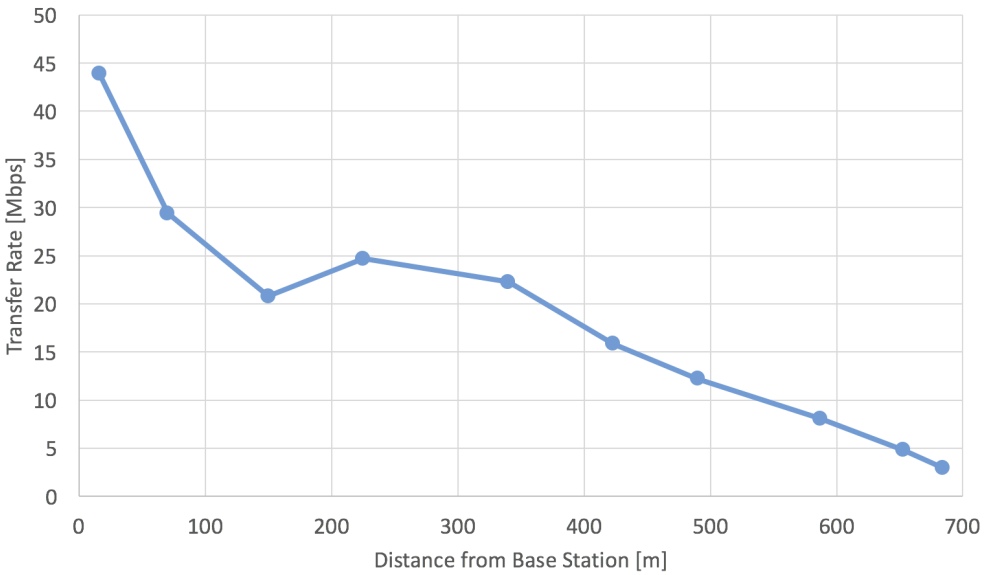

Figure 1.9: Range performance of long distance Wi-Fi system

Local communication among the MOOS applications running on the RPi2 and transmissions to the shore station were analyzed with the `nethogs` and `iftop` command line tools. While running the lawnmower pattern simulation, before deployment local communication was 35 KB/s, while

adding the shoreside monitoring passed 2 KB/s over the Wi-Fi. When deployed, the local traffic increased to 50 KB/s and with shoreside to 4 KB/s. This traffic is much lower than maximum single stream 802.11n throughput of 9 MB/s at full signal strength [26] and allows for data transmission from other equipment and reduced-signal, long-distance monitoring. Even the lowest speed mode of 802.11n far exceeds these data rates at about 900 KB/s. At the furthest data point where a reliable signal existed in Figure 1.9 at a distance of 684 m, the data rate is 2.98 Mbps or 373 KB/s, which would permit the monitoring data to be passed.

(a) Ubiquiti Bullet BM5HP and 12 dBi, 10 dBi, and 5 dBi antennas. Bullet not to scale with antennas.

(b) Futaba 6J and R2006GS

Figure 1.10: Wireless data transfer and control hardware.

In addition to the Wi-Fi for data transfer and autonomous monitoring, a standard hobby radio control transmitter and receiver provides human override control of the ASV system, which is useful for launch and retrieval as well as recovery from undesired behaviors. The Futaba 6J 6-channel system with R2006GS receiver (Figure 1.10b) is chosen for its low cost while having enough channels to control required functionality. However, the system is designed such that any radio system providing standard servo (PWM) outputs can be used, as the Arduino interprets the inputs directly

from the receiver outputs for each channel. For the EMILY system, the RC controller provides throttle, rudder, and motor starting commands as well as a switch to select human or autonomous control. The same Arduino program has been successfully used with other hobby RC systems supplied with boats converted to ASVs. The range of most hobby RC controllers is sufficient to control the ASV within a distance where observation with the naked eye is reasonable, and thus does not require additional amplifiers or high gain antennas, which contributes to the simplicity and compact design of this self-contained hardware system.

1.2.3 Positioning and Depth Measurement

For the purpose of developing a complete hardware package that is usable for single beam sonar survey applications and for installation on the development ASV, a dedicated inertial navigation system (INS) is integrated. The CHRobotics GP9 GPS-Aided INS (Figure 1.11a) is selected for this purpose due to acceptable accuracy and ease of integration while at very low costs compared to similar systems. The GP9 is a Microelectromechanical system (MEMS) based inertial unit with temperature calibration, barometric compensation of heights, and an internal Kalman Filter to compensate for accelerometer and gyroscope drift using the GPS. It interfaces natively with the RPi2 using a 3.3V TTL serial connection, and the binary data format is decoded in the autonomy software. The power requirements are low enough that the GP9 can be directly powered from the RPi2 as well, simplifying installation. With a GPS signal, the GP9 has specified accuracies of 1° in roll, pitch, and heading and 2.5 m positioning accuracy at a 95% confidence interval [27], [28].

These accuracies are sufficient for International Hydrographic Organization (IHO) Order 1b uncertainty standards [29] when using single beam sonar, since beamwidths on a small system would be larger than the roll and pitch accuracies. The IHO is the worldwide governing body of ocean mapping and NOAA survey practices adhere to their standards. If the use of a multibeam sonar is desired on an ASV with this system, better positioning and orientation would be required but could still be achieved with a compact, low power MEMS system such as the SBG Ekinox, Applanix POS MV Surfmaster, or possibly even the SBG Ellipse-D in shallow water [30]. These

systems, however, are at least an order of magnitude more expensive than the GP9.

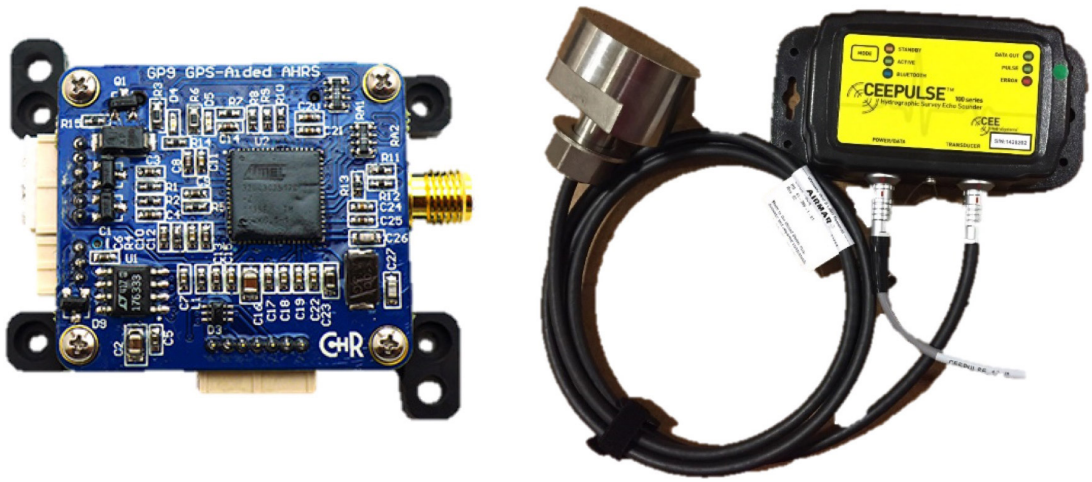

(a) ChRobotics GP9 GPS/IMU (b) CEEPulse Single Beam Sonar

Figure 1.11: Position and depth sensing equipment

The focus of the full system is general autonomy for surface vessels. Without loss of generality, hydrographic surveying is chosen to be the specific application for this research. To measure water depths, the CEE Hydrosystems CEEPulse (Figure 1.11b) is selected. The CEEPulse can operate in depths of 0.3 - 100 m, and supports automatic settings adjustment and bottom tracking, making it ideal for unmonitored applications in shallow water. The CEEPulse is used with a 9° beamwidth transducer, which allows fopr assumption that most vessel roll and pitch motions are within the beamwidth and therefore measurements do not need to be adjusted for attitude. The CEEPulse is IP68 waterproof rated and can transmit data to the RPi2 over Bluetooth, permitting flexibility in installation on retrofit vessels.

1.2.4 Power

The components of the first design iteration of the autonomy system were selected so as to be capable of being powered by a single 5 V DC power supply. The prevalence of USB based charging means 5 V regulated battery supplies are widespread in the form of rechargeable power banks, which could provide a simple method of powering the system. Unfortunately, due to the inter-

mittent current draw of servos, electrical interference in the EMILY system, and the change to Bullet Wi-Fi, a multi-voltage operation system is used instead. However, the goal of simplicity in integration is still achieved, as the final system requires only a single 9-24 V DC input. This falls within the range of standard 12 V marine batteries, as well as the 11.1-18.5 V Lithium Polymer (LiPo) batteries common in hobby RC boats. The EMILY boat has a 14.8 V battery pack that can also be used to power the autonomy system. A reduced system (later discussed in Section 1.3) is still capable of operating from a single 5 V battery pack.

For the full system, in the final version components operate on three voltages, each provided by a separate regulator. Assuming a 14.8 V input on EMILY, voltage regulator specifications and uses are provided in Table 1.1

Voltage [V]	Maximum Current [A]	Components
5	9	RPi2, GPS/INS, RC Receiver
9	2.5	Arduino
24	3	Bullet WiFi

Table 1.1: Specification and uses of voltage regulators

When integrating the autonomy system on EMILY, it was found that the electrical systems on board have noise and spikes in the ground when running the gasoline engine that cause the Arduino to malfunction if the PWM and digital outputs were directly connected to EMILY components. As a result, a secondary isolated power system was designed for these signals. This requires a separate battery pack, so the full system on EMILY requires two power inputs. This battery pack can be supplied with 4 AA batteries and mounted within the same case as the other components.

Power draws for each component in the vessel autonomy system are tested separately and presented in Table 1.2. The total draw under normal conditions is 8080 mW or about 8 W. The EMILY battery pack contains four 5000 mAh batteries at 14.8 V, for a total of 296 Wh. Therefore, under normal operations including a continuous link to the base station and sonar mapping, the autonomy electronics can run for almost 37 hours. This is much longer than the endurance of any battery powered vessel and more than most gasoline or diesel powered vessels so long duration operations will not be compromised by the autonomy system depleting the battery pack.

Component	Voltage	Maximum [mA]	Normal Operation [mA]	Normal Power Draw [mW]	Normal Operation Notes
Raspberry Pi 2	5	459	280	1400	Running MOOS mission
GP9	5	140	124	620	GPS locked
RC Receiver	5	30	21	105	Signal from transmitter
Servo (2 Total)	6	600	5	30	Holding position
Arduino	9	90	87	783	Running EMILY code
Bullet	24	133	133	3192	Data transfer active
CEEPulse	15	128	128	1920	Pinging
Total				8080	

Table 1.2: Autonomy hardware system component current and power draws.

1.2.5 System Integration

For integration into EMILY, the autonomy system components are mounted in a waterproof plastic enclosure with external connections for power, ethernet, GPS antenna and the interface cable to the EMILY hardware. A manual engine shutoff switch which is mounted externally to be accessible when the enclosure is closed, is provided in case of electronics failure. The GP9 INS is aligned with the container, which can be rigidly mounted and the orientation of the motion sensor referenced to the vessel. A diagram of the connections within the system on the vessel is shown in Figure 1.12.

As mentioned in Section 1.2.4, the signals interfaced directly to EMILY electronics were isolated using an optical isolator and separate power system. With this in place, the system operates reliably under both human RC and autonomous control. A custom circuit board was designed to provide the isolation functionality. The schematic for this board is shown in Figure 1.13. Input from the Arduino is routed to the opto-isolator integrated circuit (ILQ621GB), which then goes to the corresponding outputs, which go to the EMILY control system connector receptacle. The ILQ621GB is only able to supply 50 mA continuous current to the output, so an additional higher current transistor is necessary for the kill switch output, which draws more than that when enabled. The

The total cost of the autonomy system is minimized while allowing for flexibility in configuration for application to a variety of vessel platforms as explained above. The costs of the components are given in Table 1.3. This table also includes the shore station components for a total cost.

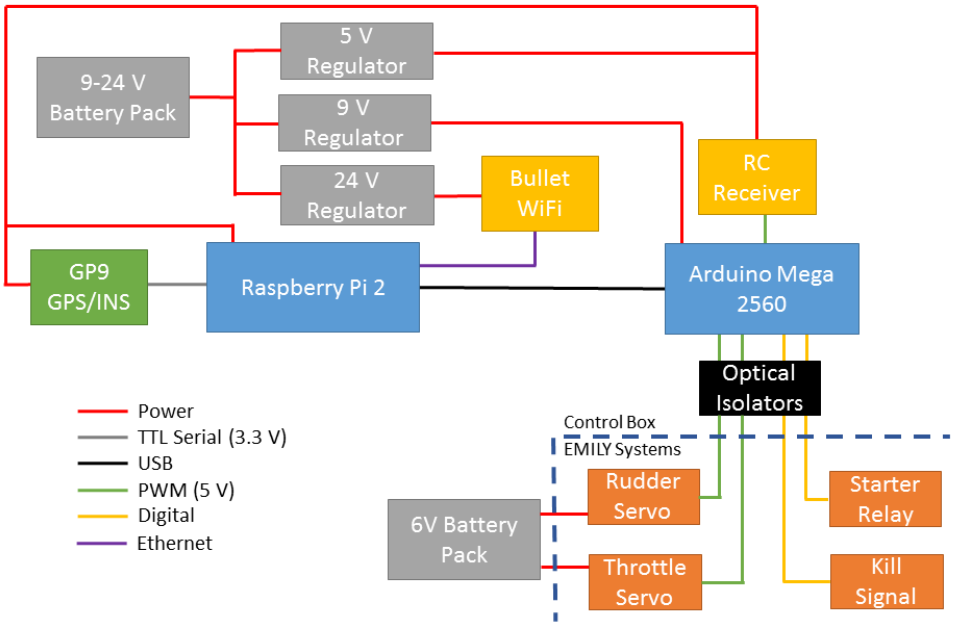

Figure 1.12: Block diagram of vessel autonomy system

	Device	Cost
ASV System		
Autonomy Computer	Raspberry Pi 2 Model B	$35
Microcontroller	Arduino Mega 2560	$46
GPS/INS	CHRobotics GP9	$399
Hobby RC System	Futaba 6J	$180
Long Distance Wi-Fi + Antenna	Ubiquiti Bullet M5HP, ROK8DBI 10 dBi	$88
Voltage Regulators	Pololu 5V & 9V Step-Down, 24V Step-Up	$57
Enclosure	BUD Industries NBB10263	$60
Plugs and Connectors	Bulgin PX0707/S/25, Sure Seal Power	$60
Signal Isolator Custom PCB	Advanced Circuits	$33
Misc Parts & Wires	Opto-Isolators, Transistors, Switch	$47
	Subtotal	*$1005*
Shore Monitoring System		
Long Distance Wi-Fi + Antenna	Ubiquiti Bullet M5HP, Air802 12 dBi 5 GHz	$153
Antenna Stand	Impact 9.6' Studio Light Stand	$36
	Total	*$1194*

Table 1.3: Autonomy hardware system components and costs.

The full system, when mounted in the box for installation on EMILY or another vessel, is shown in Figures 1.14 and 1.15. The voltage regulators are mounted to the lid to minimize interference

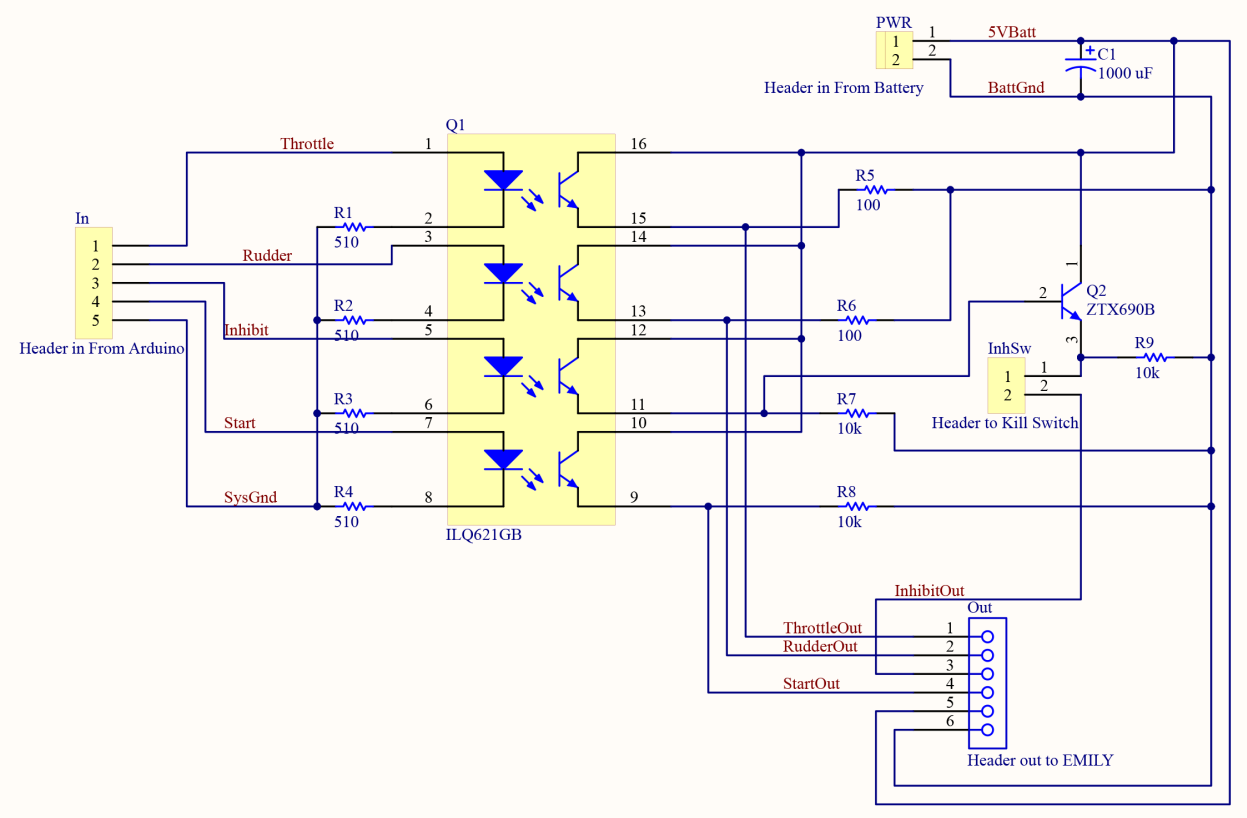

Figure 1.13: Schematic of EMILY control signal isolation board

with other electronics. In addition to the main compononents, the box includes a breadboard for ease of adaptation to new vessels if simple electronics or low current power distribution is needed.

This complete system is also used directly in testing for ASV3 for control systems and sonar mapping. For this method of operation, the EMILY battery box can be moved to ASV3, or the system can run directly from the 12 V lead acid marine batteries used for the propulsion system. Due to the effort for compatibility, the Arduino for the native electronics of ASV3 accepts the same commands as that in this system to control thrust and rudder angle. As such, since the box otherwise provides all necessary functionality for data transfer and autonomy, the USB cable is simply switched to connect to the RPi2 in the box.

To provide power and data transfer for the sonar system, a USB to RS232 converter is connected to the RPi2, and an additional power cable run from the main input distribution to the sonar power connector. Optionally, an ethernet switch may be added to distribute the Wi-Fi data from the Bullet

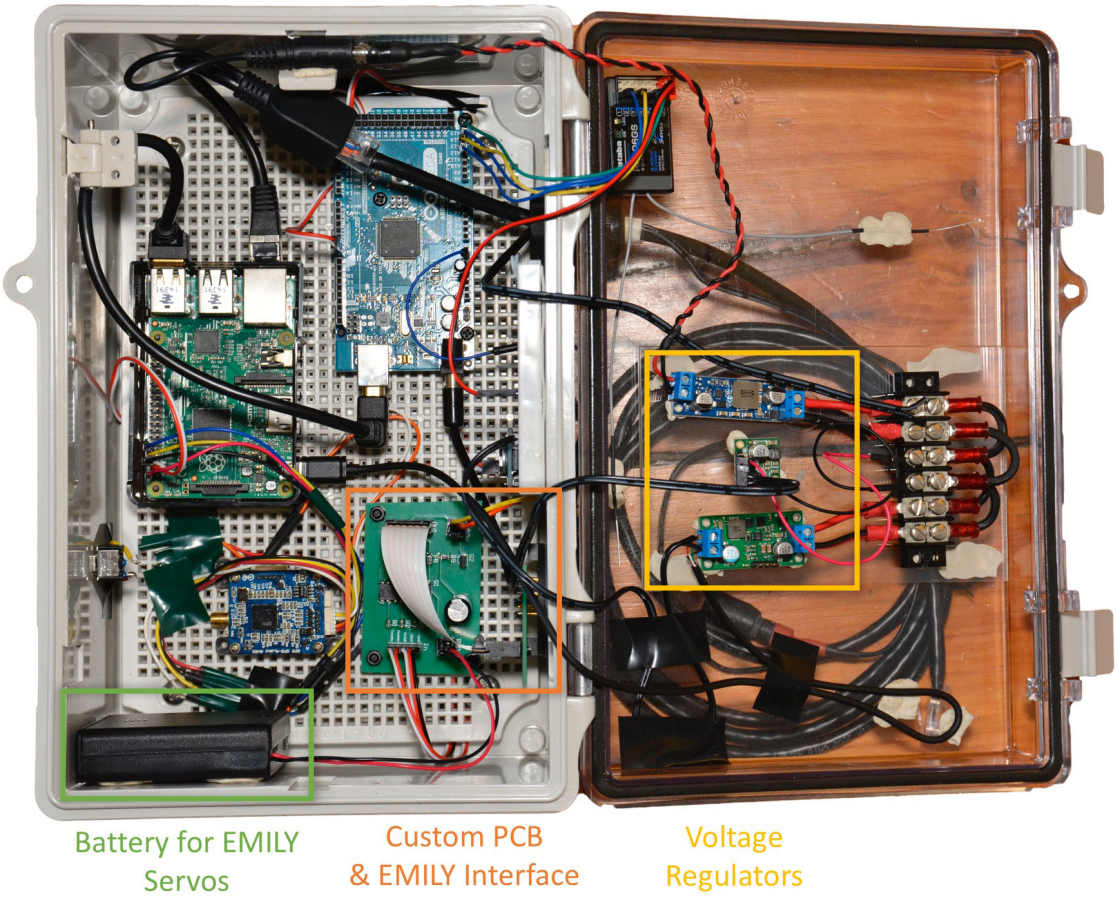

Figure 1.14: Complete autonomy retrofit hardware system for EMILY, marking components not previously pictured.

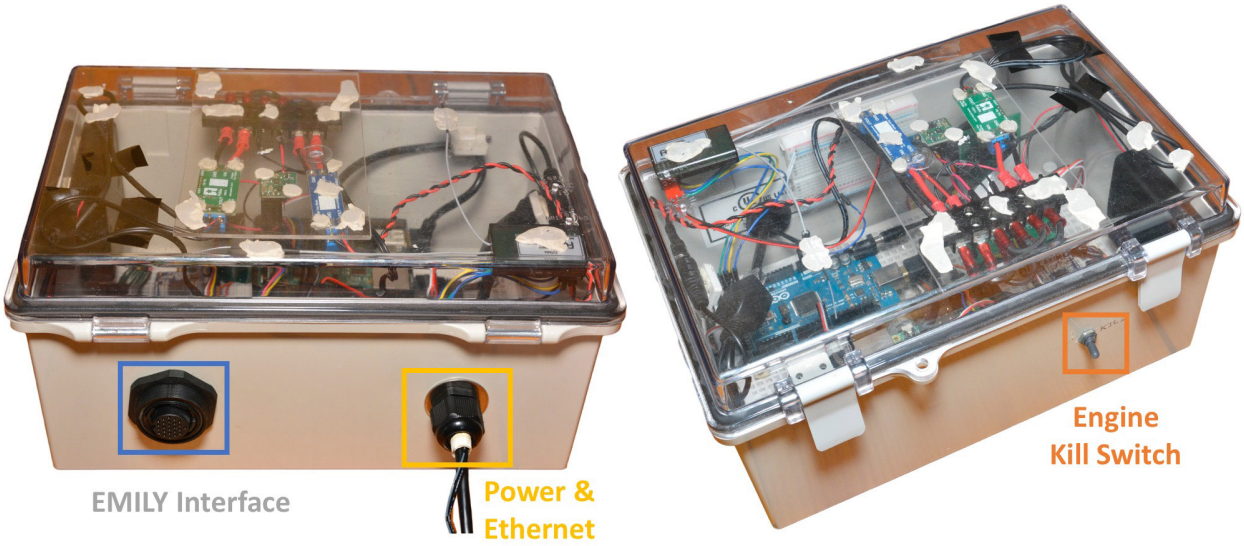

Figure 1.15: Exterior of the EMILY hardware box.

to multiple onboard computers, and draws power from the 5 V regulator. This additional wiring is fed through the penetration in the box where the EMILY control system connector is mounted for operation on EMILY.

1.3 Reduced System for Commercial Survey ASVs

When positioning and data transfer systems are already in place on a commercially designed ASV, implementing autonomous control with this system requires a significantly simplified set of electronics. In this research, specialized modules are developed for Teledyne Oceanscience Z-Boat 1800 systems using a subset of the components detailed above. The Z-Boat vessels provide a dual GNSS positioning and heading system, Ethernet routing for internal devices and data transfer to a monitoring station, power distribution, and an RS232 serial data input for throttle and rudder positioning commands. Given these systems, the autonomy module is only required to contain the RPi2 and a voltage regulator to convert the 12 V Z-Boat system to the 5 V necessary to run the RPi2. The module may also use a USB battery pack as an independent power source. A summary of the power and interfaces is given in Figure 1.16.

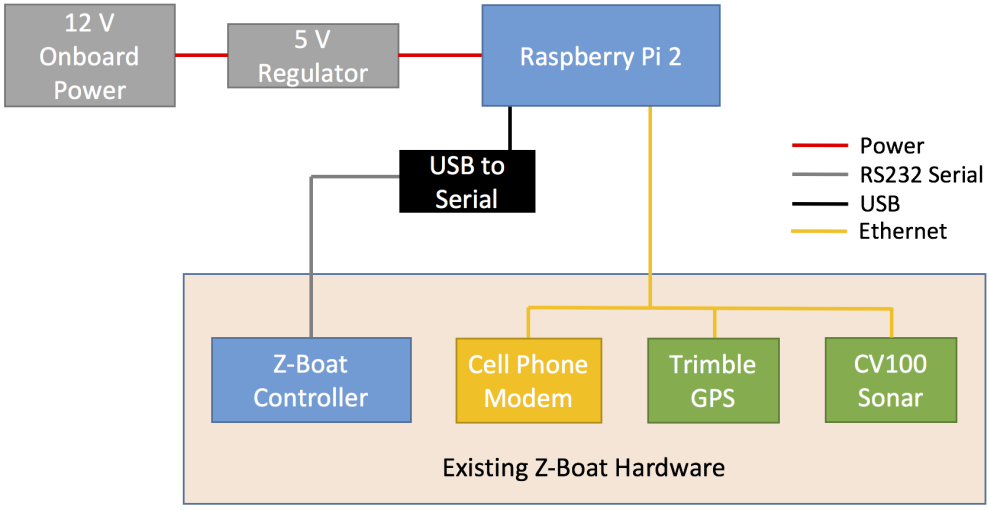

Figure 1.16: System diagram for Z-Boat module.

A waterproof housing box is designed with USB, Ethernet and power connectors for interfacing

with the existing Z-Boat systems, shown in Figure 1.17.

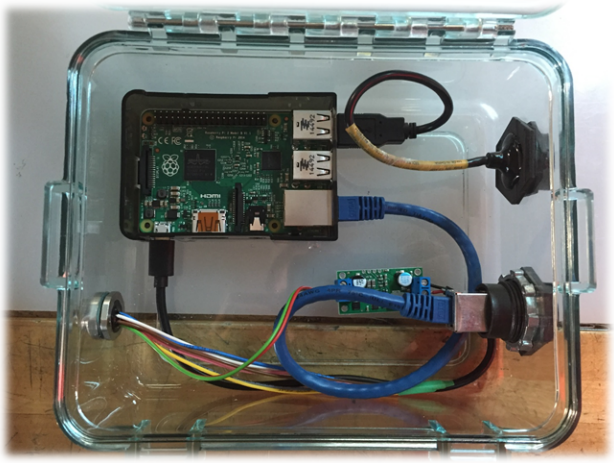

Figure 1.17: Simplified autonomy module for Z-Boat

This module was tested on specialized rugged Z-Boats designed for the NOAA Ship *Thomas Jefferson* and a multibeam sonar equipped test boat provided by Teledyne Oceanscience, which are described in Section 1.1.2. The cost of the complete autonomy module, including cables for connection to the Z-Boat power system and USB to RS232 converter for control command output was $223 when purchased in September 2015. Due to the low cost, three identical modules were purchased to operate the two *Thomas Jefferson* Z-Boats with one spare.

1.4 Direct Autonomy Installation

The autonomy software can run on a Linux or Mac OS X based computer, which provides flexibility for implementation on vessels with existing computing hardware. More mature platforms designed for remote controlled or autonomous hydrographic survey have onboard computers to aggregate and store data. These vessels also have the other required positioning and communications hardware such that autonomous functionality can be implemented without additional hardware. Since many existing commercial hydrographic software packages only support Microsoft Windows, this research also analyzes the software as tested on virtual machine environments running on Windows host operating systems. For these tests, Ubuntu 14.04 is installed in a virtual machine

hosted with Oracle VirtualBox VM software. By leveraging existing hardware, the cost and complexity of implementation can be further reduced and the processing power will often be higher than on the default embedded computer for the full system described in Section 1.2. The common operating system between the RPi2 and virtual machine facilitate rapid simultaneous development with corresponding software package availability and device configuration.

CHAPTER 2

AUTONOMY SOFTWARE AND OPERATION

The MOOS-IvP open source autonomy framework, which is maintained by MIT and Oxford forms the basis for the autonomy system [31]. The software compiles and runs on most Linux distributions and Mac OS X, including embedded ARM based systems such as the RPi2 in this application. MOOS (Mission Oriented Operating Suite) utilizes a centralized message-passing architecture (MOOSDB) which coordinates communication between multiple applications known as MOOSApps. MOOSApps can publish and subscribe to data streams without knowledge of any other running applications. In an autonomous vehicle, these postings consist of information about the status of subsystems, the position of the vehicle, and the environment in which it is operating.

MOOS uses TCP connections to transfer information, so the core MOOS process can be on the same computer as the applications or a different one across a network. MOOS also includes applications that add functionality for sharing information between MOOS databases, so that each maintains up-to-date copies of certain information when networked, while allowing multiple independent instances to run. This can facilitate interaction between different vehicles in a swarm, or in this case it is used for the monitoring station to interact with the vehicle without affecting autonomous operations if it is out of range.

The MOOS-IvP package comes with applications for common tasks and behaviors in marine autonomy and can be extended to interface with platform specific systems. The applications can be configured on the command line or with options provided in a human-readable structured text file defining the mission. The provided pAntler utility automatically launches and configures MOOSApps based on the mission file. Together, the MOOSDB and communicating MOOSApps form what is termed a MOOS community. MOOS-IvP provides simulation capabilities which allow testing of applications and behavior configurations with simulated vessel movements. Simulations

can be accelerated to multiples of real-time operation speed for rapid testing of full missions or reaction to long term processes.

Monitoring of simulations and vessels in the field is accomplished through the supplied graphical user interface (GUI) MOOSApp, pMarineViewer. An example of a waypoint mission running in the graphical interface is shown in Figure 2.1. An overhead view of the vessel and mission is provided, with the ability to display a background image or chart and points, lines, or polygons relevant to the mission. On the left side, a set of panes is provided for viewing the textual AppCasts that MOOSApps can send to provide feedback to the user on their operation. Red highlights indicate where a MOOSApp is posting an error, which directs the user to potential problems. The lower portion of the GUI provides information on the position and orientation of the vessel, as well as buttons to trigger modes within the mission. The actions of these buttons and additional actions in a drop down menu are configured in the mission file.

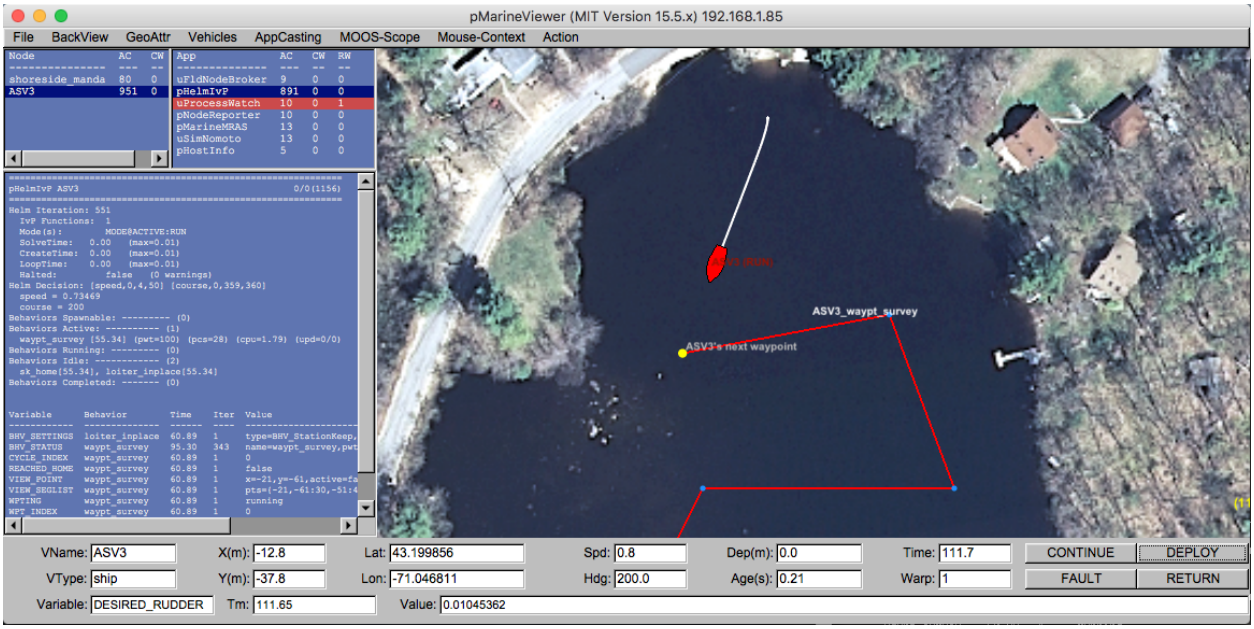

Figure 2.1: Graphical interface for monitoring MOOS missions, shown with waypoint behavior.

2.1 IvP Helm

A key MOOS application is the IvP (Interval Programming) helm, which defines the actual behaviors for autonomy and commands the heading and speed of the ASV. The MIT repository includes existing behaviors for waypoint navigation, collision avoidance, track and trail, and station keeping, along with simple constant heading and speed behaviors. The behaviors are configured in a text file (separate from the mission file) that sets the initial configuration options, which in turn contribute to how a heading and speed are determined for the behavior. Behaviors may also be updated from other MOOS applications. For example the waypoint navigation behavior is able to receive a new set of waypoints from a separate path planning MOOS application.

The IvP Helm includes the ability to build a hierarchical behavior structure, and facilities are exposed for development of custom behaviors. Behaviors define functions over the domains of speed and heading (and depth for underwater vessels), where the peaks of these represent optimal settings for the vessel. Multiple behaviors can be active simultaneously, and a weighted sum of their functions used to determine the path of the vessel. This is used for reactionary behaviors that are always active, but sometimes not contributing to the desired motion of the vessel, such as collision avoidance which modifies behavior only when other vessels are detected.

2.2 Implementation of MOOS-IvP for This Project

A basic behavior structure is used to form a consistent base for field testing missions in this research. This is shown in Figure 2.2, including details from the survey path planning mission detailed in Chapter 3. The survey portion of the mission can be changed to whatever behavior is desired for the primary operation, such as fixed pattern of waypoints, a timed testing routine or contact related behavior. In this structure, the states shown in yellow are modes to separate different behaviors, but only define which sub-level behaviors can be executed and do not directly control the actions of the vessel.

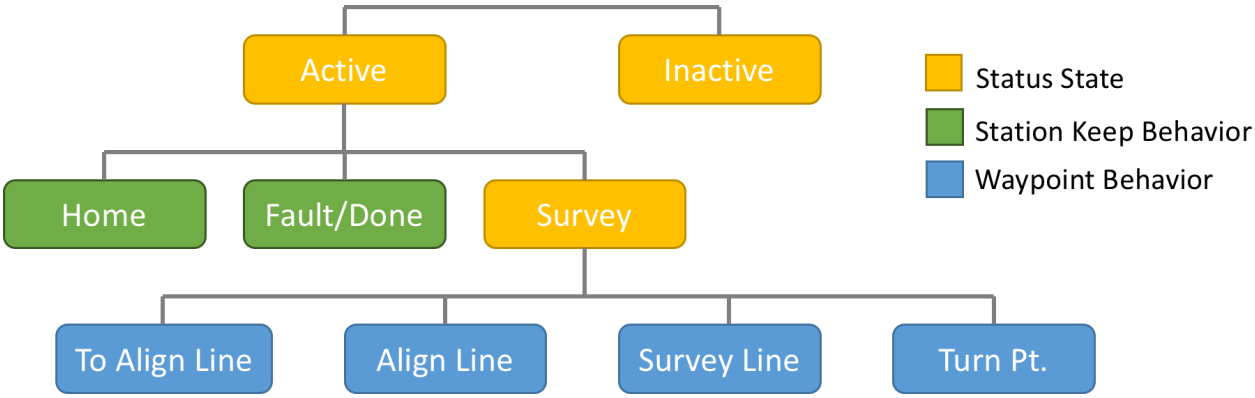

Figure 2.2: Basic behavior structure used for field testing, including details of survey behavior described in Chapter 3.

The **Inactive** state is only executed upon startup of the mission, and does not output any specific desired aspects for the vessel. This is used for initial deployment, when the vessel is human controlled. Once the autonomy system is activated through the user interface, all behaviors run in the **Active** mode. The default initial mode when in the active state is to immediately begin the designated **Survey** mode. The **Home** station keeping behavior can be activated at any time through the user interface, which causes the vessel to transit to a designated home location and hold position. The home location can be updated by clicking a point on the overview map, which can be used to direct the ASV to a specific place. The **Fault/Done** behavior can either be manually activated though the user interface, or triggered by events. This behavior activates a station keep at the current location of the ASV to keep it in place. The manual activation provides a way to halt operations if another behavior malfunctions, and it also serves to hold position once a survey operation completes.

For the implementation of the autonomy system, hydrographic survey behaviors, and deployment on the test ASV, custom MOOSApps are developed in this research. The interaction of the parts necessary to run standard autonomous behaviors and the core MOOS applications used in the autonomy system are presented in Figure 2.3. The sonar and mapping related applications developed for this thesis are discussed separately in Chapter 3, and the control system application pMarineMRAS in Chapter 4. The naming convention for MOOSApps includes a prefix denoting the type of application (p for general process, i for sensor interface, u for utility/simulation) which

is reflected in Figure 2.3.

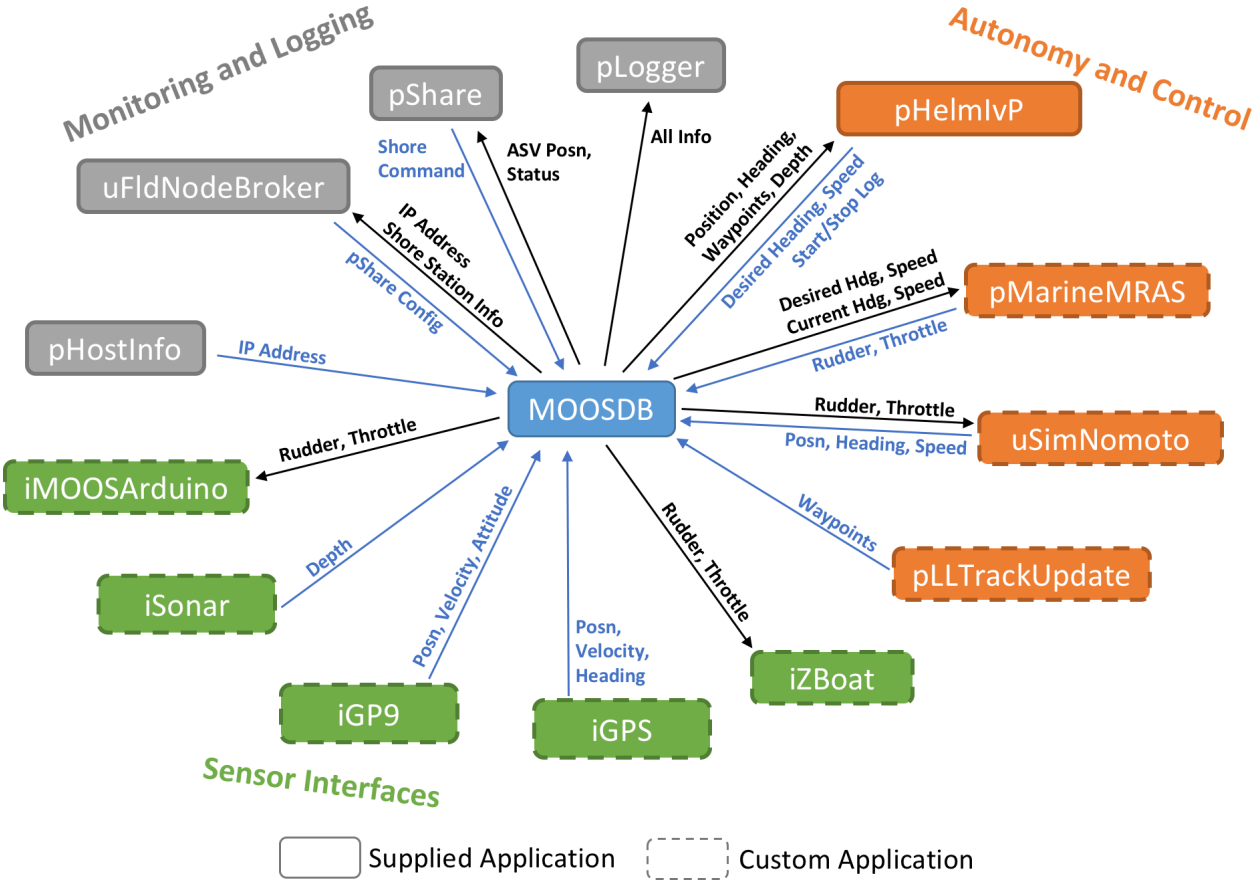

Figure 2.3: MOOS application diagram for core autonomy system

Typical operation of the vessel involves a MOOS community on the vessel that can operate all systems and execute the mission and a separate community on a shoreside computer that provides the graphical interface for monitoring and action based control. Information is passed between the communities using the pShare MOOSApp. The pShare application passes specified variables between communities using UDP, providing tolerance to connection dropouts. In this research, pShare is automatically configured by helper MOOSApps, which provide the IP address information about the computer (pHostInfo) and automatic detection of vessels and shore stations (uFldNodeBroker and uFldShoreBroker). The interaction of these MOOSApps is shown in Figure 2.4. The automatic configuration increases flexibility in running multiple shore stations or ASVs without modifying the mission file. It also provides options for selecting whether variables are passed from the shore station to single or all ASVs, so that their behavior can be managed

during field operations.

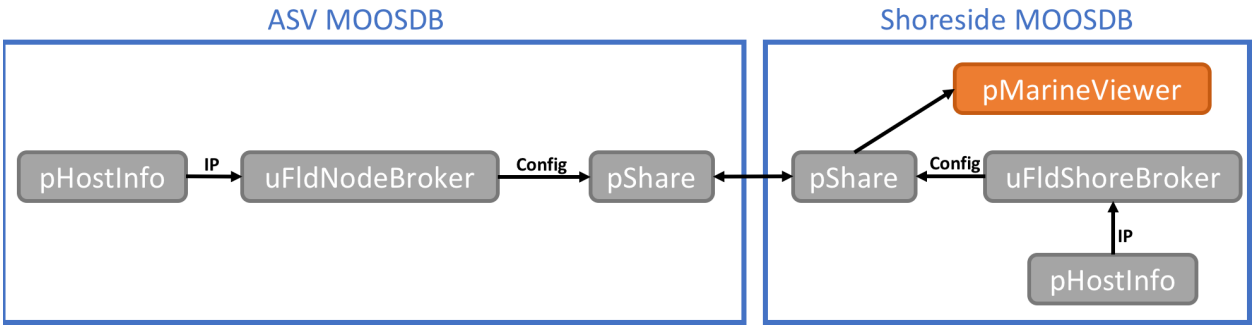

Figure 2.4: Flow of information in automatic configuration and communication between ASV and shore station.

Further automation of launching MOOS communities is provided by shell scripts that automatically build missions. The complete mission for this research is broken into modules with configurations for each MOOSApp, which are then assembled into the mission file using the `nsplug` command line utility. This program interprets variable substitutions and conditional statements within mission files that permit one mission to be easily adapted for different regions or operations. Mission generation scripts are then designed to rapidly develop new missions based on templates, or switch between vessels and simulation. This can be used to designate new operation regions or quickly switch control settings between different ASVs. A script also configures both the terrain simulator and vessel mapping component for path planning mission tests as described in Section 3.4.2. This allows new areas to be easily tested to verify the performance of the path planning algorithm.

2.3 Custom MOOSApps

Each of the component applications can be configured to meet the needs of a specific installation, both in terms of vessel systems and the processing hardware. The functionality of the general use custom MOOSApps developed for this thesis are described in the following sections. Those specific to the control system (pMarineMRAS) and survey path planning (pSurveyPath) are discussed in Chapters 4 and 3 respectively.

iGP9

The GP9 interface driver (iGP9) configures the GP9 GPS/INS and outputs the required data on startup. It then parses the data stream and posts the information to MOOS variables. The GP9 is already equipped with filters for real-time orientation data while in motion, so no additional filters are applied. An existing driver for the Robotic Operating System (ROS) for a similar device by the same manufacturer was ported to the MOOS environment to form the basis for this driver. As a result, a ROS version of this driver is also available. The GP9 interface provides location, roll, pitch, and heading.

iGPS

The GPS interface driver (iGPS) parses NMEA 0183 data that is commonly output by GPS devices. It is capable of connecting to both serial data streams and network data. The network data allows passing of positioning information from Hypack data collection software, which is commonly used on autonomous vessels with onboard computers. Hypack provides drivers for most standard equipment used in hydrographic surveying and can be set to output data from the interfaced sensors in the standardized NMEA format. This eliminates the need to write custom MOOS drivers for every proprietary data format, although it requires Hypack to be running for the autonomy system to function.

iSonar

The sonar interface driver (iSonar) accepts and interprets NMEA data strings from sonar systems. It can be configured for either network or serial port data input. This allows it to interface with any sonar that has an option to output data in this format (such as the CEEPULSE 100 used for the testing system). Hypack surveying software can also output depth data in NMEA format, so any sonar supported by Hypack can be used to measure nadir depths.

iZBoat

The Teledyne Oceanscience Z-Boat interface, iZBoat, sends commands to the Z-Boat Command and Control Module (CCM) to control the throttle and rudder angle of the propellers. As the CCM handles the low level control of the servos and motors, this interface driver sends only ASCII commands over a RS232 serial connection. In addition to the throttle and rudder, commands are sent to initiate and terminate autonomous mode. These commands are automatically sent when the system is initialized, and may also be triggered manually for operations that switch between human remote control and autonomous operation.

pLLTrackUpdate

The pLLTrackUpdate program accepts posts of new waypoints to update a track. The IvP helm handles waypoint coordinates in a local x-y grid system with an origin defined for the specific MOOS mission. This MOOSApp translates coordinates in Latitude/Longitude or Universal Transverse Mercator (UTM) to the local coordinate system and posts an updated track which can modify the mission during execution. It is designed to work in conjunction with a python script which reads Hypack planned line files (which are natively in UTM coordinates) and posts them to the appropriate variables for conversion by pLLTrackUpdate.

uSimNomoto

The simulator provided with the distribution MOOS-IvP program (uSimMarine) provides basic functionality, but contains a simplified method of determining heading and cannot simulate the effects of waves or noise in sensor readings. A modified version (uSimNomoto) is created to address some of the shortcomings. For determining the heading of a vessel from turns caused by a rudder, the linear Nomoto model is used. This model also forms the basis for the adaptive control system in this research and is further discussed in Section 4.2.2.

Wave Simulator

In order to test against some factors present in the environment, a wave simulator was developed. The simulator generates random waves of a specified significant height ($H^{1/3}$) and period (T). This is achieved by filtering Gaussian white noise with a second order band-pass filter to isolate the required spectrum. This method is used in similar simulations by Van Amerongen [2] and Velagic [32]. While the frequency response of the band-pass filter does not exactly match that of observed waves, it is sufficient for testing of response to environmental conditions.

Before applying the bandpass filter, an Infinite Impulse Response (IIR) filter implementing a second order Butterworth low pass transfer function is first applied to the Gaussian noise, to further reduce the effects of high frequency components that would be unusual in waves. The cutoff frequency for the low pass filter is based on the desired dominant wave period T as given in Equation 2.1.

$$f_c = \frac{3}{T} \tag{2.1}$$

The filter is implemented with the standard Butterworth second order transfer function

$$H(s) = \frac{1}{\left(\frac{s}{\omega_c}\right)^2 + \frac{\sqrt{2}s}{\omega_c} + 1} \tag{2.2}$$

where $\omega_c = 2\pi f_c$. This is implemented digitally with a bi-linear transform, resulting in the normalized discrete time transfer function

$$H(z) = \frac{1 + 2z^{-1} + z^{-2}}{\left(c^2 + \sqrt{2}c + 1\right) + \left(-2\left(c^2 - 1\right)\right)z^{-1} + \left(c^2 - \sqrt{2}c + 1\right)z^{-2}} \tag{2.3}$$

where c is a frequency warping factor given by

$$c = \cot\left(\frac{\omega_c T_s}{2}\right) \tag{2.4}$$

where T_s is the sample time specified by the MOOSApp iteration rate [33].

The center frequency ω_0 of the bandpass filter is based on the Bretshneither family, with

$$\omega_0 = \left(\frac{4B}{5}\right)^{\frac{1}{4}} \tag{2.5}$$

where B is defined from the Modified Pierson-Moskowitz family as

$$B = \frac{691}{T^4} \tag{2.6}$$

where T is again the dominant period of the waves [34]. This frequency is shifted to get an encounter frequency based on the motion of the ship. This is given in Equation 2.7, where U is the speed of the ship, γ is the angle between the heading of the ship and the direction of travel of the waves and g is the acceleration due to gravity [32].

$$\omega_e = \omega_0 - \frac{\omega_0^2 U}{g}\cos\gamma \tag{2.7}$$

The encounter frequency is used as the center of a second order bandpass filter defined in the Laplace domain in Equation 2.8, where H_{RMS} is the root-mean-square height of the waves, defined from significant wave height as $H_{RMS} \approx H^{1/3}/1.4$.

$$H(s) = \frac{2\zeta\omega_e H_{RMS}}{s^2 + 2\zeta\omega_e s + \omega_e^2} \tag{2.8}$$

The transfer function is transformed to the Z domain as given in Equation 2.9. This is applied in the MOOSApp as an IIR difference equation, the components of which are broken out in 2.9 for clarity.

$$
\begin{aligned}
H(z) &= G\frac{b_1 + b_2 z^{-1}}{1 + a_2 z^{-1} + a_3 z^{-2}} \\
G &= -\frac{2\zeta\omega_e H}{\sqrt{1-\zeta^2}} \\
b_1 &= -\sqrt{1-\zeta^2} \\
b_2 &= e^{-\zeta\omega_e T_s}\sin\left(\sqrt{1-\zeta^2}\omega_e T_s + \arccos\zeta\right) \\
a_2 &= -2e^{-\zeta\omega_e T_s}\cos\left(\sqrt{1-\zeta^2}\omega_e T_s\right) \\
a_3 &= e^{-\zeta\omega_e T_s}
\end{aligned}
\tag{2.9}
$$

The damping ratio ζ is determined to give a constant bandwidth, which transfers the same power from the Gaussian noise signal, allowing the amplitude of the result to be consistently scaled for the correct significant wave height. It is defined in Equation 2.10, where the numerical factor of 0.017 is found to give approximate RMS results to the desired wave height.

$$
\zeta = \frac{0.017\pi}{\omega_e} \tag{2.10}
$$

The simulated waves affect the speed and rate of turn of the vessel. The speed is most affected when the waves come from directly ahead or behind the vessel and the heading when they are at a 45 degree angle to the bow or stern. This means that when the waves are on the beam, they have their minimal effects on both speed and heading, as most of the energy would be translated into roll and sway in the vessel. In addition, the effect on vessels by waves of the same amplitude should be inversely proportional to the size of the vessel. These effects are achieved by multiplying the wave amplitude by factors given in Equation 2.11, where A_{wave} is the wave amplitude output from the bandpass filter. These scaled amplitudes are added to the speed and rate-of-turn otherwise determined by the vessel model. The scaling factors approximate the responses observed in the small ASVs of this research, and may not be directly applicable to larger vessels.

$$A_{\text{speed}} = \frac{0.3}{L}\cos(\gamma)A_{\text{wave}}$$
$$A_{\text{ROT}} = \frac{2.6}{L}\sin(2\gamma)A_{\text{wave}} \tag{2.11}$$

The effects of these simulated waves over time is seen in Figure 2.5. In this example, the simulated waves are from 000°T, so that the heading is the relative angle. It can be seen that the waves have a maximum effect on speed at 0° relative and minimum at 90° relative as expected. The heading is most affected at 45° and least at 90° and 0°.

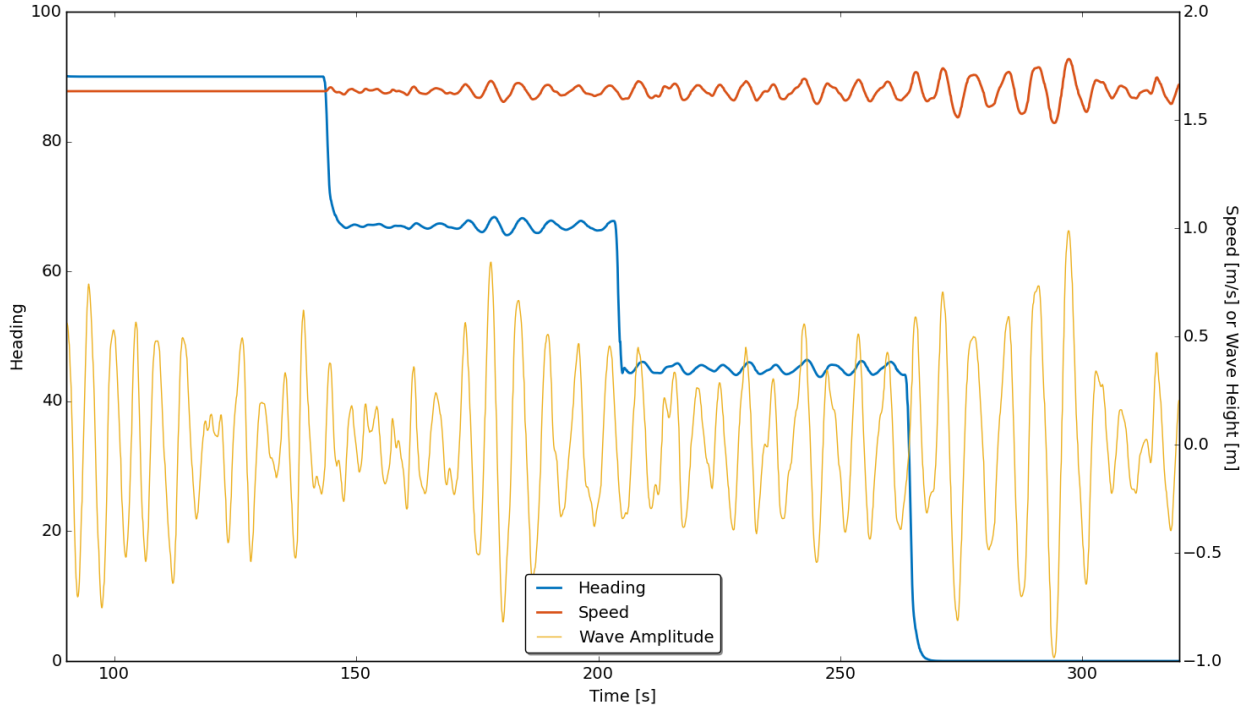

Figure 2.5: Effect of simulated waves on speed and heading, waves from 000°.

Sensor Noise Simulator

In addition to waves, the simulator can generate high frequency noise to mimic that found in some low cost motion sensors. Noise is prevalent in the GP9 sensor used for this research, so it is important to simulate the effects of the noise to ensure that the autonomous operation remains satisfactory. The noise simulator also uses Gaussian white noise as the input to a filter, in this case

a second order Butterworth high pass. The cutoff frequency is configurable; a default of 1.2 Hz is used in simulations for this research, which matches the observed response on the GP9. The filter as implemented in the Z domain, is given in Equation 2.12. Note that the denominator is the same as in 2.3, and c is the same as defined in 2.4.

$$H(z) = \frac{c^2 - 2c^2 z^{-1} + c^2 z^{-2}}{\left(c^2 + \sqrt{2}c + 1\right) + \left(-2\left(c^2 - 1\right)\right) z^{-1} + \left(c^2 - \sqrt{2}c + 1\right) z^{-2}} \tag{2.12}$$

The noise simulation is only applied to heading, as the speed measurements from the GP9 are from raw GPS measurements and do not suffer the same effect. An example of the noise effects is shown in Figure 2.6. The noise amplitude is configurable, and in this example is set to 0.8, which scales the output from the high pass filter, but does not specifically correspond to the amplitude of the effect on the rate of turn.

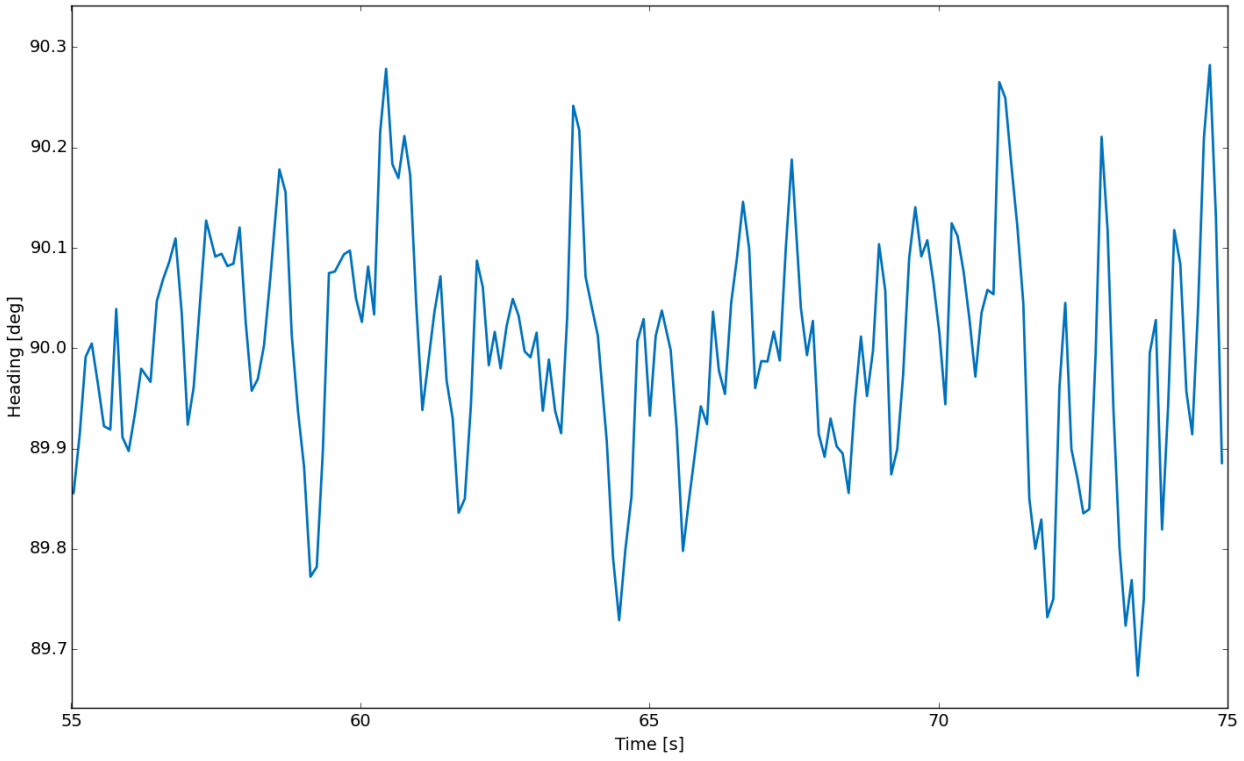

Figure 2.6: Effect of simulated noise on measured heading while ASV is navigating on a heading of 090°.

CHAPTER 3

AUTOMATED SWATH SURVEY PATH PLANNING

3.1 Introduction

Most current hydrographic surveys employ multibeam sonar systems for depth measurement, which provide a fixed swath angle viewing of the seafloor with a number of data points returned along the swath profile. Most multibeam hydrographic surveys require complete coverage, defined as "100% bathymetric bottom coverage with multibeam sonars" [35]. The fixed angle of the sonar causes the width of the swath across the seafloor to vary with depth. Therefore, in order to achieve complete bottom coverage, neighboring survey lines must be spaced more closely in shallow water than in deep water. AUVs avoid the problem of having to anticipate varying swath widths over a survey area, as they can be instructed to maintain a constant altitude above the seafloor.

Maintaining a constant altitude above the seafloor is not an option for ASVs, as their height above the bottom is determined by the full water depth. However, in most existing applications, survey planning for ASVs inherits fixed or preplanned line spacing from the AUV paradigm [36]. In more complex schemes, an area can be subdivided by depth ranges and different line spacings planned for each range [18] [37]. In order to achieve complete coverage, these parallel lines are still required to be spaced according to minimum depths in the region, leading to inefficient extra overlap elsewhere. Any preplanned adjustments for depth also require knowledge of the area, but usually the purpose for conducting a survey is due to uncertainty in the existing data. This chapter presents a method for comprehensive coverage path planning that does not require prior knowledge of the bathymetry in the survey area and that adjusts survey lines dynamically based on the data acquired during the survey. This method mimics that of how human-driven data is currently collected during NOAA surveys, where a coxswain steers a survey launch to match and overlap

realtime coverage reported from the sonar system with a graphical coverage map of previously surveyed area. It is similar to a method developed by Bourgeois [38] [1] but is intended for small autonomous platforms and uses a different algorithm to increase the probability of achieving complete coverage. An example of results from Bourgeois is shown in Figure 3.1. The terms "line" and "path" are used interchangeably in this thesis to refer to the desired survey path of the ASV.

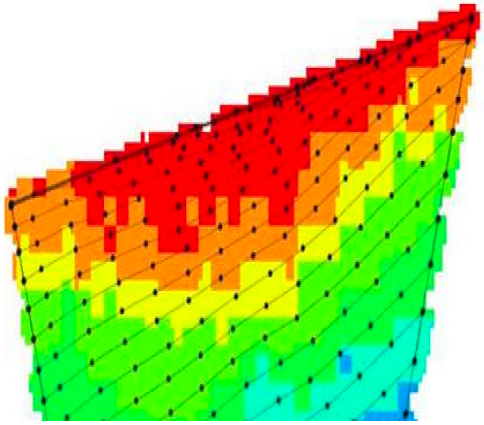

Figure 3.1: Results of automatic path planning designed by Bourgeois [1], using piecewise linear planning.

3.2 Adaptive Line Planning

The path planning process can be subdivided into two main steps: recording the swath data and planning the next survey line. The second step of planning the next path requires multiple subprocesses to generate the final path that will be driven by the autonomous surface vehicle. An operation region can be defined to specify limits for the survey, as is typical during human controlled acquisition.

3.2.1 Swath History Recording

Recording the data is a straightforward process, but incorporates some refinement during data collection to reduce the processing load at the end of the line. This allows the new line to be computed as quickly as possible and passed to the autonomy system, so that surveying can continue

without any delay. The data recorded are assumed to either come from a sonar with no errors (in simulation) or a filtered raw sonar record as discussed in Section 3.3.

While the ASV is following a survey line, it records the swath width from the sonar system uniquely on the port and starboard sides, along with the accompanying vehicle position and heading at the time of the depth measurement. This allows the edges of the swath to be positioned for later path planning. Each recorded point adds to an accumulated distance, which then triggers selection of a minimum swath when a specified interval is reached. This method is used to decimate the recorded points, and therefore reduce the processing load at the end of the line as mentioned previously. The selection of the minimum along a length ensures that the next planned path will be a conservative approach to complete coverage with the previous data. However, even with this method, it is possible that additional local minima within the decimation length would not be overlapped in subsequent swaths if they were planned with no overlap. The decimation process is shown in Figure 3.2. The subdivision of path for selection of minima can be set depending on the resolution needed for the final path. For the simulations in Section 3.4, a 10 meter decimation length is used.

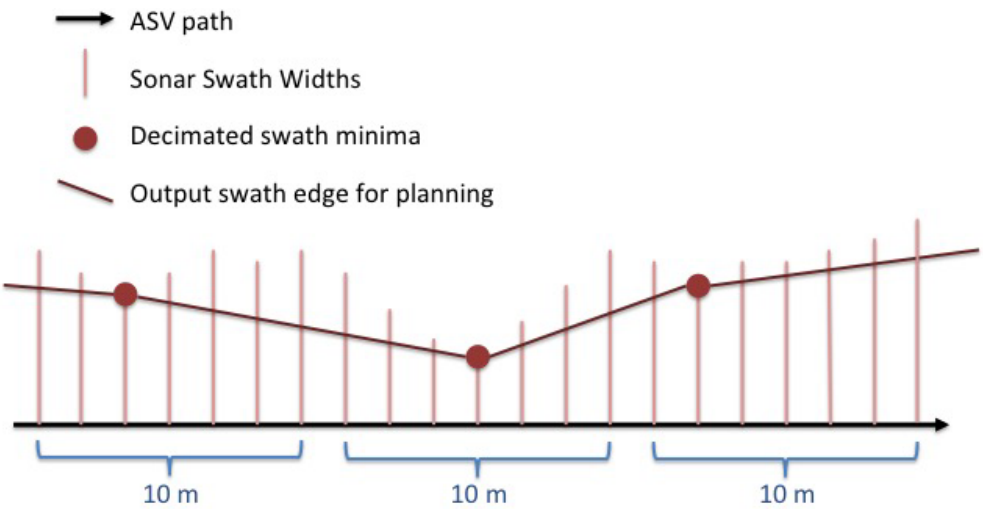

Figure 3.2: Illustration of the selection of swath minima points from full raw data record, which are then used as a basis for planning the next path.

In addition to maintaining the decimated swath record, the history recorder keeps a full data record for the purpose of determining what area has been covered by the sonar. This is stored as

a coverage polygon which can then be displayed or used in the path planning algorithm where knowledge of the area covered by data collection is required. The data coverage from each line is unioned with previous lines to form a single polygon (possibly containing inner holes), indicating areas from which data has already been collected.

3.2.2 Planning Subsequent Paths

When a survey line is completed, the swath recording module is signaled to output the minimum swath edge on the side of the next path to be planned (basis points) and their corresponding locations. The path planning module then uses this swath as a basis for determination of the next path. This process takes a number of steps, starting with an offset from the edge of the basis points.

Offset from edge of swath

The basis points are used to first create an offset path that forms the first pass on path planning for the subsequent swath. If an operation region is defined, basis points outside the region are first eliminated to ensure that the vehicle is not directed to survey outside the region. The basis points on either side of each point are then used to form vectors, and the perpendicular to the average heading between them is used to determine the direction of the offset vector. This translates the sequential minimum swaths to an offset direction. The offset distance is then calculated from the previous swath width at the basis point. The offset distance may also be reduced or enlarged by a factor to ensure overlap between outer beams where uncertainty is higher or to create a striping pattern if full bottom coverage is not required. The first offset step is shown in Figure 3.3.

This initial offset path is processed to filter track points that would lead to undesired operation of a vessel or incorrect survey methodology. Specifically, sharp turns and loops are not desired during data acquisition because they decrease data density on the outer side of the turn and can increase uncertainty in attitude measurements.

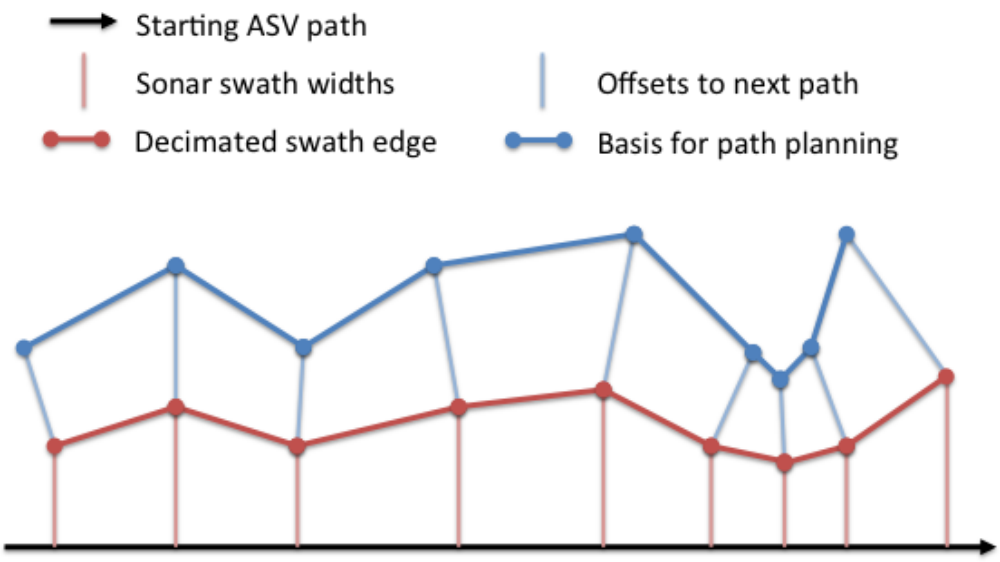

Figure 3.3: Illustration of the generation of an offset line for initial input into the refinements of the path planning algorithm. This shows a straight initial line for data collection, but the same process is used for subsequent segmented lines. No additional overlap is added in this example.

Removal of self intersects

The first step to refine the path is to remove areas where the path crosses over itself, which would not only cause unnecessary turns, but also duplicate coverage in some areas. These crossings can occur where the ASV executes a turn with a radius less than twice the width of the sonar swath at that point. Each segment is tested against following segments to see if it intersects them. If there are intersections, the portion of the path between the first and last intersect is removed. This process is repeated along the path until all self intersections are removed.

Removal of sharp bends

The processing algorithm next eliminates bends in the path that exceed a defined angle. Large angle turns are avoided because they cause increased spacing between sonar detections along the outside of the turn and force the ASV to turn in a smaller space than its physically possible turning radius, which could lead to undesired operation from the line following control system. For the simulation and testing discussed in Section 3.4, the maximum bend angle is 60°. To eliminate bends, the path is checked along the direction of travel. When an angle between segments is larger

than the threshold is encountered, test segments are formed by eliminating subsequent points until an angle with the first segment less than the maximum is found. Elimination of the end point of the first segment of the bend is also tested to see if it results in less points being removed from the planned path.

Even checking both these scenarios and selecting the minimum point removal strategy can sometimes result in large amounts of waypoints being removed. As a result, some alternative evaluations are built into the algorithm. If less than twice as many points as the minimum method are removed by the other method and the resulting path bend angle is smaller, then the smaller bend angle is chosen despite the fact that it will eliminate more points from the planned path. If testing to eliminate a bend reaches the end of the path, the beginning of the segment is assumed to be the problem, and the algorithm is run recursively on a path with this point removed. With these additional factors, this method of bend removal is found to give more desirable results than that of other methods, such as calculating gradients along the path.

An example of removal of both self intersection segments and sharp bends is shown in Figure 3.4. The resulting line is much smoother and better able to be driven by the autonomous waypoint navigation behavior without difficulty.

Fitting of path to operation region

With drastic bends and self intersections removed, the path is now ready to be fit to the defined operational region. The survey region can be irregularly shaped and turns near the ends can create swath edges that lie outside the regions; therefore, it is necessary to fit the path within the region. The path is first clipped to the region by finding the last segment that transitions from outside to inside the region on each end of the line and intersecting these segments with the region border. The intersection points are inserted as the new ends of the path. Points before (at the beginning of the path) or after (at the end) these intersection points are eliminated. As opposed to eliminating only points outside the region, this accounts for paths that could oscillate in and out along the edge.

If the path is entirely within the survey region on either end, the last segment is extended until

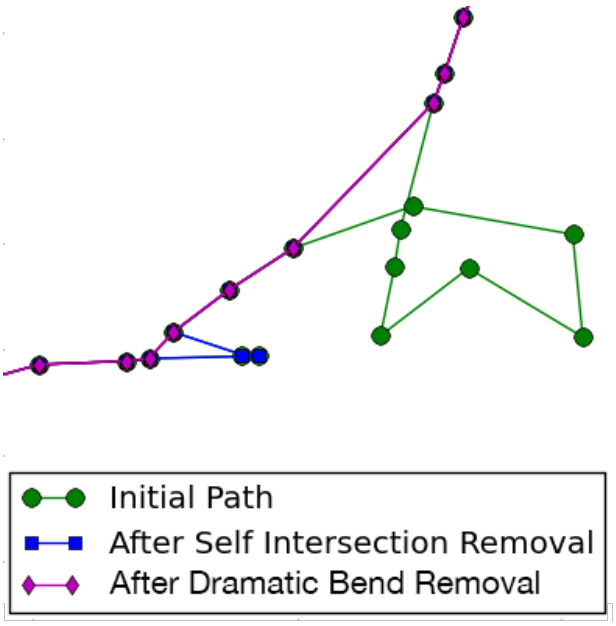

Figure 3.4: Example of path refinement from a simulated path, with removal of intersecting segments (green) and areas with sharp bends

it reaches the nearest edge of the polygon. Typically this results in a logical intersection, but turns at the end of the line can result in the nearest edge in the direction of extension being further than would be desired for operation, so the extension length is limited to 15 times the swath decimation interval. The extension and clipping processes are shown in Figure 3.5.

Elimination of points in existing coverage

A final step is taken that eliminates planned points that fall within existing coverage to try to prevent unnecessary duplication in data collection. Points can fall in existing coverage after turns in areas of rapidly changing depth, as a result of elimination of intermediate waypoints from the removal of intersections and bends or from the extension process of the previous step. While elimination of waypoints within existing coverage does not guarantee that the planned path will not overlap previous data, it helps reduce the amount of unnecessary data collection.

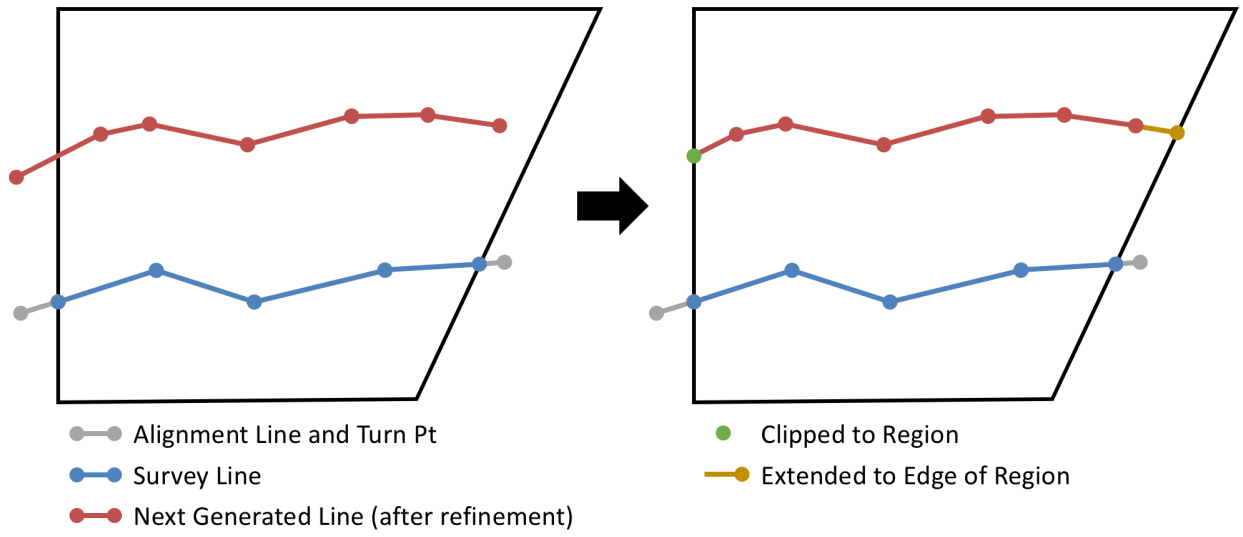

Figure 3.5: Diagram of path clipping and extension process, showing before (left) and after (right)

3.2.3 Completion Metric and Holiday Detection

The operating region is considered completed when the next planned path has all waypoints eliminated, either because they are outside the operating region or because they go through an area with existing coverage as described in Section 3.2.2. At this point, the vessel can be instructed to either hold its last position, return to the deployment location (or another specified meeting point), or continue to another operating region.

Another method will terminate the survey before completing the region if shallow areas are detected. Upon reaching a first precautionary threshold, the path planning algorithm commences a procedure known as half-stepping. Since the data coverage area is known and the sonar is continually monitored, it can be assumed that the previously surveyed area is safe for transit by the

ASV. Therefore, upon detection of a shoal, it will divert in the direction of the prior survey line and follow the edge of the previous swath, as shown in Figure 3.6. This is the same procedure currently followed by human coxswains. While half-stepping, if the depths increase, such as for an isolated shoal, the ASV resumes normal path planning operation. If the shoal is part of a natural rise toward shore and a shallower halt threshold is reached, the next path will be planned on top of the previous path for these locations. If all other areas in the operation region are completed but a shoal remains, or the shoal stretches along the entire line, the region is determined to be complete.

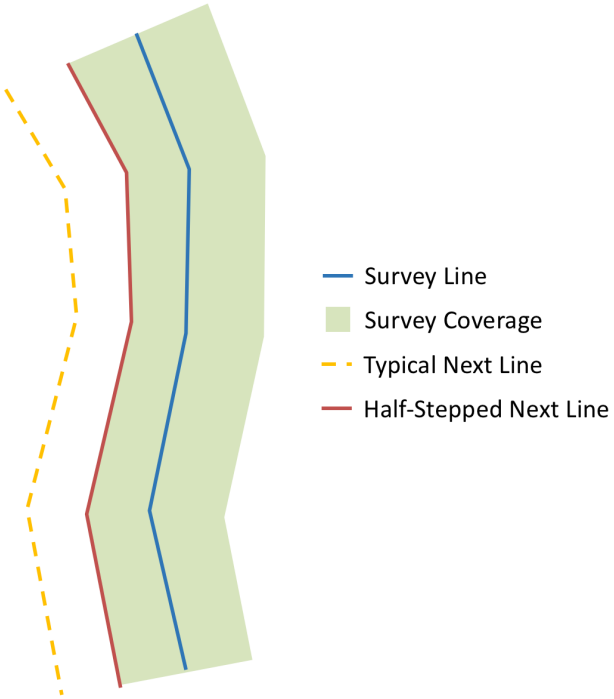

Figure 3.6: Half stepping behavior demonstrated, with next line planned along edge of previous swath coverage.

Within the operating region that has just been completed, the coverage record kept by the swath recorder can be used to identify where there are gaps in the data such that it would not meet complete coverage requirements. These gaps are known as holidays and are required to be filled before a survey area is deemed complete. The holidays can then be targeted for completion, which is currently achieved by planning a path among them after completion of the first pass of the region. The current algorithm only addresses holidays as point locations, but larger ones could be addressed as a separate set of operation regions.

3.3 Auxiliary Functionality

In addition to the core path planning routine, some functionality has been implemented to facilitate integration of the in situ path planning with physical systems and autonomy environments.

Between survey lines, an ASV must be directed to properly reach the next survey line. The ASV must turn from one line to the next in a logical fashion, which depends on the spacing between the lines and the possible turning radius of the vessel. For a typical turn, a single point is placed outside the survey operation region, along a line leading from the last segment of the survey path. For the simulations in Section 3.4, it is placed 50 meters from the edge of the survey area. This point is planned along with the line, so that the vessel can immediately begin transiting to the point while the next line is planned. After the path planning algorithm determines the next line, if the spacing is smaller than the turning radius of the ASV, two additional points are placed to create a modified Williamson turn pattern that directs the vessel onto the next line as shown in Figure 3.7.

On the end of the turn, an alignment line is planned that extends the first segment of the survey path beyond the operation region. This line forces the ASV to align its heading with the upcoming survey line so that it is not oscillating or completing a turn when entering the survey region, which increases data quality due to the decreased yaw motion. This line is also shown in Figure 3.7.

As mentioned in Section 3.2.1, the swath recording component of path planning assumes that the data are correct, but actual sonar systems report incorrect depths occasionally as a result of bubble sweepdown under the transducer or incorrect bottom detections on objects in the water column such as fish. Multibeam sonars are also susceptible to interference from the specular reflection of the main lobe at nadir being detected in sidelobes. All of these processes reduce the depth detected as compared to the actual depth and therefore would affect the minimum swath based decimation. To avoid this, some filtering of the raw data is necessary. For the system implemented, a standard deviation filter is used that maintains a history of the previous swath widths and rejects those that are above a set number of standard deviations from the mean. For the field tests of the algorithm, a limit of 2 standard deviations based on the past 4 seconds of recorded

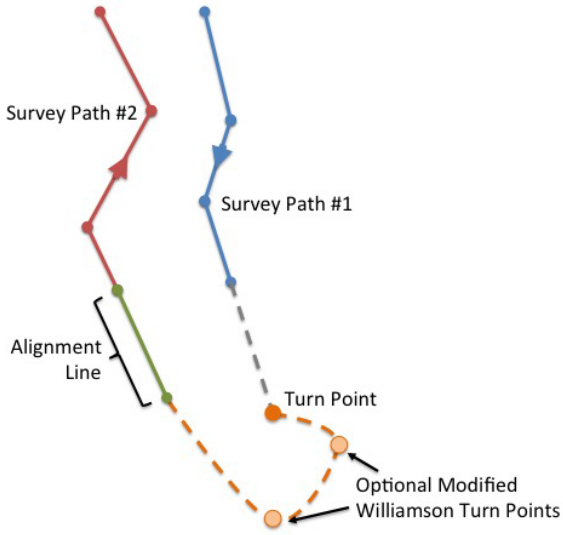

Figure 3.7: Example of a planned turn between subsequent survey lines showing the turn point extended from the end of the first line and alignment line extending from the beginning of the second line.

depths functioned well.

3.4 Simulation Results

The path planning algorithm is developed and tested using a custom simulation program created for this purpose. After the algorithm was determined to perform suitably, it was integrated into the MOOS-IvP autonomy environment for deployment on ASVs and further testing in simulation.

3.4.1 Custom Simulation Program

A custom vessel movement simulator is programmed in Python to support development of the path planning algorithm. The program developed for this research simulates a vessel following a trackline made up of waypoints and gives sonar depth and swath width values from either generated depth patterns or data imported from previous surveys. It implements the full sonar swath recording and path planning algorithm from Section 3.2.

An example of a simulation run on a generated pattern of an "X" shaped depression with a hole in the middle is shown in Figure 3.8. The survey lines are initially planned at an angle to the edge of the operation region in this example, showing how the lines will be extended and clipped as needed. The distance between lines increases in the deeper areas (blue) causing them to bend around the spot. The calculated coverage using this simulator shows gaps at the edges of the survey area, but this is because the turning points are not included when driving the simulated vessel. In an actual survey using the turning points and alignment lines, these planned paths would achieve full coverage of the assigned region. This issue is also discussed in more detail by Bourgeois in [1].

Additional examples with generated terrain are shown in Figure 3.9, where the differences in spacing between lines with depth are clear. Figure 3.9a shows a sharp bend elimination limit of 60° in effect, where the ridge slowly creates a sharper bend after the first line until the limit is reached, at which point they stay constant. As a result, small holidays are created in the areas around bends, but these are detected and could easily be addressed with a line before completion of the region, which is preferable over attempting to make turns that are not physically possible with the vessel.

The simulation developed for this research can also be run with previously collected and grid-

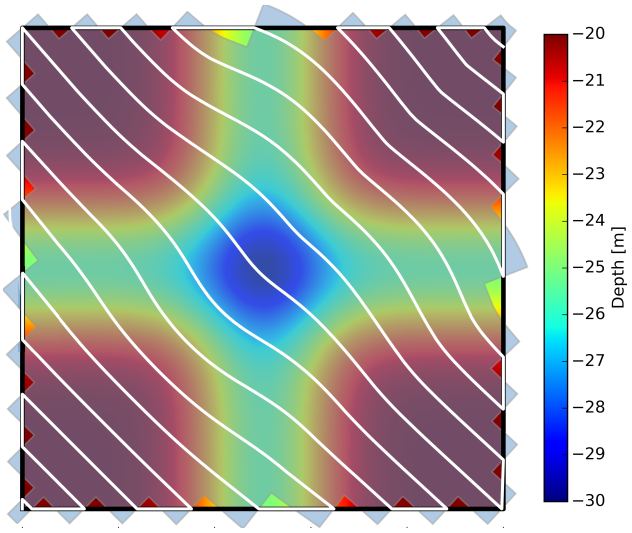

Figure 3.8: Custom simulation with generated terrain. Survey paths shown in white, coverage in transparent blue.

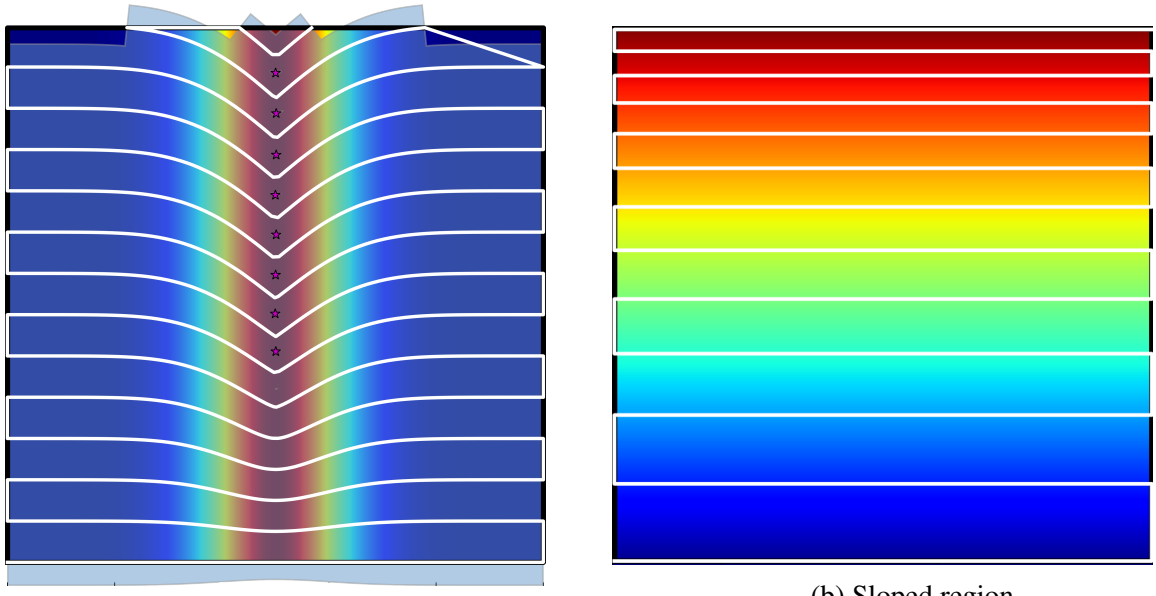

(a) Ridge in center

(b) Sloped region

Figure 3.9: Custom simulator with generated terrain, with vessel path in white and detected holidays marked with stars. Bathymetry is shown as a rainbow colored background where blues represent deeper depths and reds shallower.

ded data as a background. A GeoTIFF file is used as the input along with the survey operation region and starting line. The program uses data from near the coast of New Hampshire collected by the 2014 Summer Hydrographic Field Course at UNH [39], and the results are shown in Figure 3.10. In the relatively flat section on the left, the swaths are spaced closer as the simulated

vessel moves inshore, and the survey lines remain fairly parallel. In the more complex terrain of the right section, the paths become bent where the depths change and some holidays are left where dramatic bends were removed from the planned paths. These are marked with stars and can be addressed by additional data acquisition.

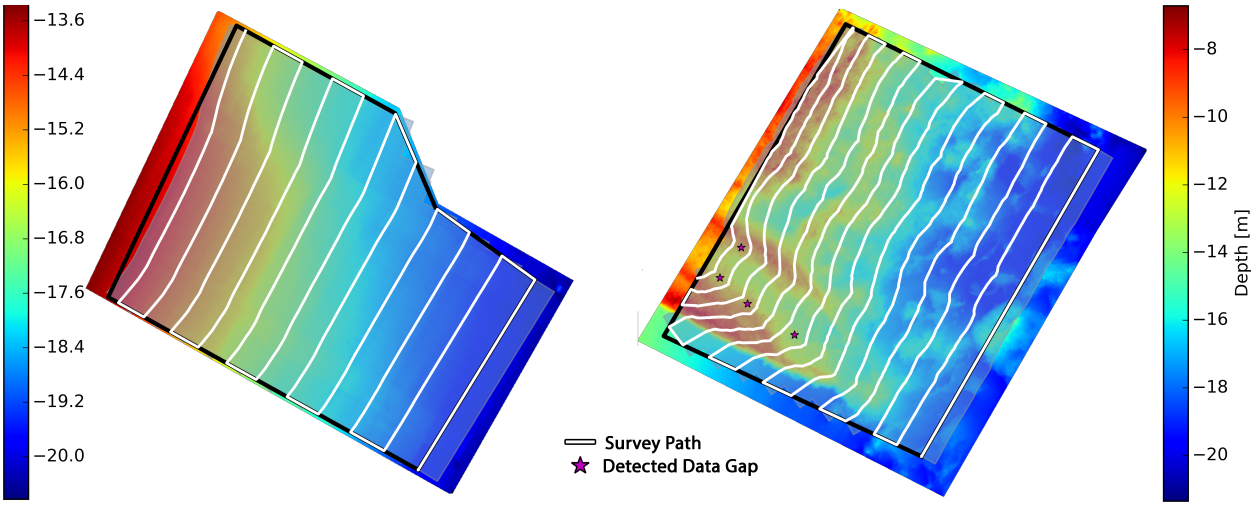

Figure 3.10: Custom simulation using actual terrain. Data coverage is shown in transparent blue and holidays marked with stars.

3.4.2 MOOS-IvP Implementation and Simulation

The implementation of these core and some auxiliary behaviors discussed in Section 3.3 is shown in Figure 3.11. The complete MOOS mission is structured as discussed in Section 2.2, this shows the execution during the survey portion. A starting line is first surveyed along an edge of the region, which can be selected automatically as the first side of the polygon or defined in the mission. When this line or any subsequent one completes, swaths continue to be recorded until both sides are outside the region, or the turn point is reached. This ensures that full coverage is achieved within the region as long as the turn points are sufficiently offset.

When recording ceases, the processing for the next line is initiated in a separate thread, while the vessel transits to the turn point if it has not yet reached it. At the turn point, if processing is complete, the next survey line and its associated alignment line and turn point are posted to update the associated IvP behaviors. If processing is incomplete, or was initiated by reaching the

turn point, the vessel holds station until processing completes and then posts the updates. The vessel continues to the beginning of the alignment line, which is defined as a separate behavior to facilitate addition of Williamson turn points and separate the transit from the alignment line. Upon reaching the beginning of the alignment line, swath recording commences so that the intersection of coverage with the edge of the survey region can be determined. After completing the alignment line, the survey line commences, starting the cycle again. This process is repeated until no points are within the region on the next planned line, or all offsets are zero due to reaching a depth limit as described in Section 3.2.3.

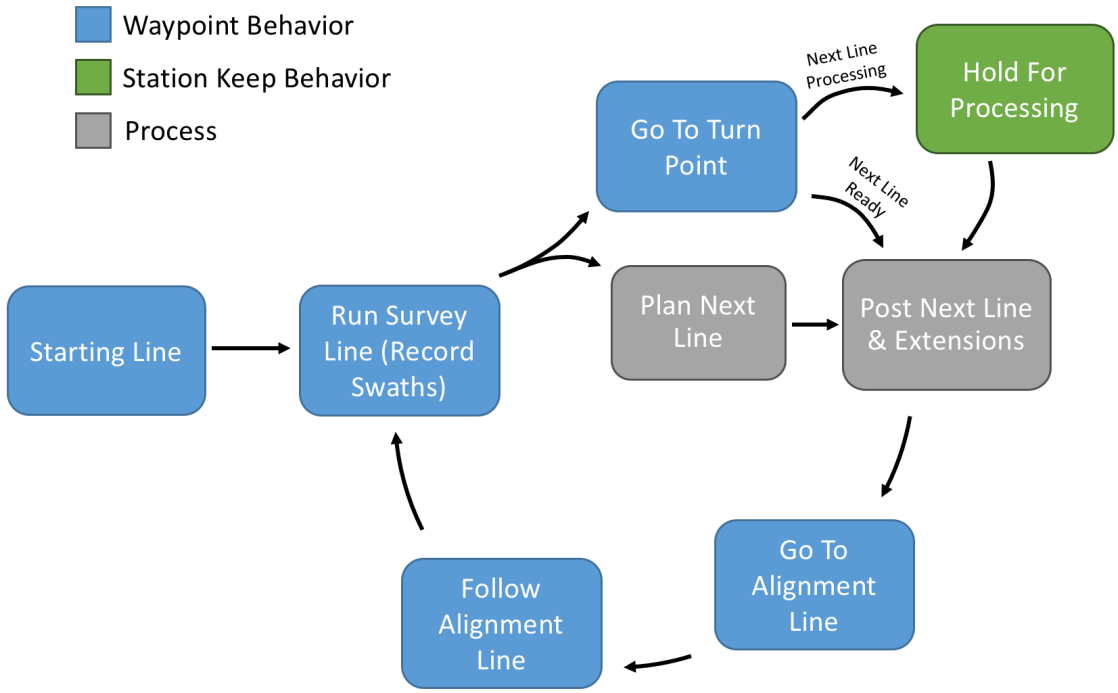

Figure 3.11: MOOS behavior and application flow diagram showing states during the survey portion of a path planning mission.

The path planning algorithm and simulation was first implemented into MOOS-IvP as three separate MOOS interfacing Python applications. This leveraged much of the existing code from the custom simulator discussed in Section 3.4.1, allowing further refinement of the algorithms within the actual autonomy environment to be used on the vessel. In this structure, the sonar simulator reads data from a gridded file of previously collected bathymetry, the swath recorder keeps track of both the full coverage and decimated swath records, and the path planner outputs

the next survey line based on the recorded swaths as well as the turn points and alignment lines.

After successful testing of the Python applications, a native C++ MOOSApp was created to handle the survey path planning. This combines 2 of the former Python programs and makes launching and configuration more intuitive as it is now the same as the other packaged MOOS-Apps. The C++ MOOSApp includes all functionality necessary to operate in the field, while the data simulation from previous bathymetry remains a separate Python program. A diagram of the implementation in MOOS is shown in Figure 3.12. The C++ app is also refined for faster processing of paths, enabling more reliable operation and larger areas to be surveyed.

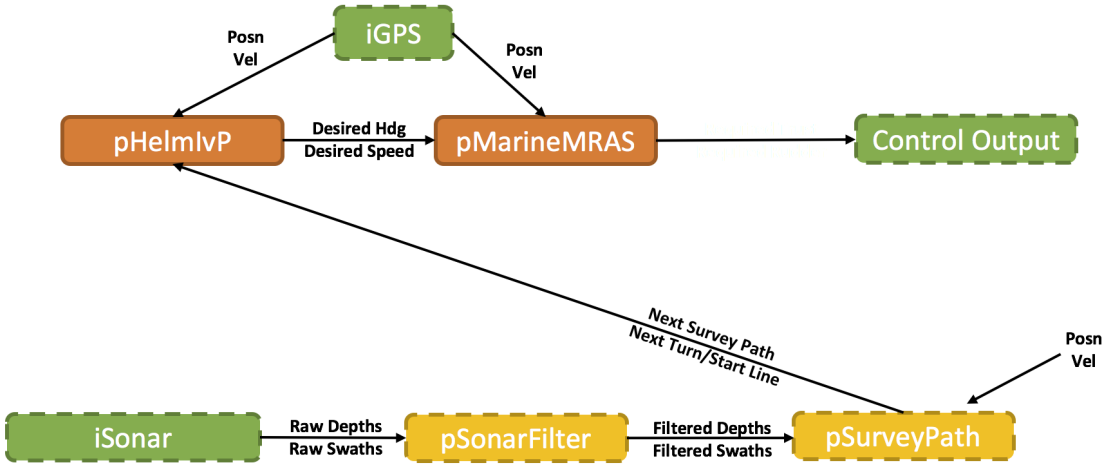

Figure 3.12: MOOS behavior and application flow diagram showing states during path planning algorithm and simulation execution.

Using this more realistic MOOS-based vehicle simulation, the path planning algorithm is tested on a variety of terrains and can be compared to the human directed survey efforts that produced the source bathymetry data. Selected areas that were originally planned as polygonal regions and surveyed using consistent line orientation are compared from a variety of locations. This provides diversity in the coxswains driving the launches, hydrographers directing data collection and methods of line planning.

The first areas for comparison are from the UNH 2015 Summer Hydrographic Field Course [40]. Due to requirements of the course, lines are required to be run parallel to each other, so a direct comparison with the shape of the lines cannot be made. In a southern region, the lines were

planned in the field based on observed swath widths (but still parallel lines). The lines were then driven using a heading autopilot on the vessel. In fairly featureless terrain, this method should be similar to the results obtained by the path planning algorithm. In this region, the path planning algorithm completed 16.5 lines, while the human survey used 17 lines. However, despite using more lines, the parallel method resulted in holidays and less overlap in the outer beams than the method presented in this research. The results of the depth adaptive path plan are shown in Figure 3.13a, with the human driven lines in light grey.

Comparison can also be made on the basis of total distance traversed during the survey operation. The IvP waypoint behavior maintains an odometer measure, which can be used for this purpose. Source data for the human driven operations was unavailable for many regions tested and the lines did not match exactly with the areas drawn for comparison, so the line were traced manually from either tracks in an image or by examining uncertainty plots for the nadir region, then adding estimated turns. The simulated MOOS-IvP operation used artificially enlarged alignment and turn point offsets over the capabilities of a small ASV to allow time for processing paths at high time warps, so the estimate of the vessel track is likely longer than required. In contrast, clicking along an approximate track will underestimate the actual human survey linear distance by simplifying the line. Therefore, comparisons with this method tend to underestimate the distance saved by using the automated line planning in conjunction with an ASV.

The region in Figure 3.13a shows a similar vessel travel distance for the human and automated surveys, but the automated survey still results in 8% less distance driven. This is the closest result obtained for the regions in which simulations are performed, and is due to the use of adjustable planned lines as mentioned previously.

In a second region within the UNH 2015 Summer Hydrographic Field Course survey, the survey lines for the field course were adjusted only for the shallowest depths expected in the region, a common method for preplanned ASV missions. In this region, the adaptive path planning travels 56% less distance to complete the survey. The shallower depths at the southern end of the region cause the adaptively planned paths to bend, but the northern portion is completed with less lines

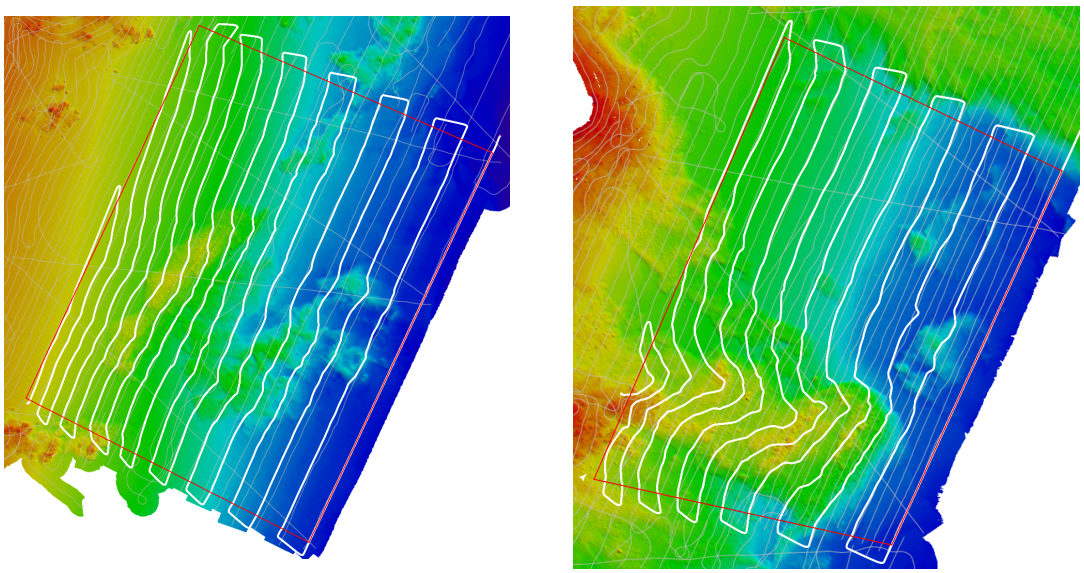

(a) Southern Region

(b) Northern Region

Figure 3.13: Simulation results from MOOS-IvP simulation showing survey behavior. A red box denotes the specified operation region and the white lines show survey paths. Human data collection paths shown in light grey. Bathymetry is shown as a rainbow colored background where blues represent deeper depths and reds shallower.

and only small holidays are left in the regions with tight turns. Assuming a survey speed of 7 kts, the depth adaptively planned survey requires almost 2 hours less underway time than the static spacing version, a dramatic time and fuel savings. The survey planning results for this region are shown in Figure 3.13b.

Surveys conducted by NOAA Ships *Fairweather* and *Rainier* are used to compare the path planning algorithm to human surveys conducted under an adaptive methodology, where the coxswain visually matches the current swath with the edge of previous coverage. Three regions are investigated that contain a variety of terrain. A fairly flat area with a few ridges near Chirikof Island, AK is shown in Figure 3.14. The general patterns of each data collection method are similar, but even here, the automated survey is able to reduce acquisition travel distance by 20%. The reduction is mostly due to the ability to more closely follow the desired path, reducing unnecessary overlap between swaths. While the environmental conditions may have dictated closer spacing at the time, it is also likely that less overlap was required in the human survey.

Surveys conducted near the Shumagin islands are also compared between human and auto-

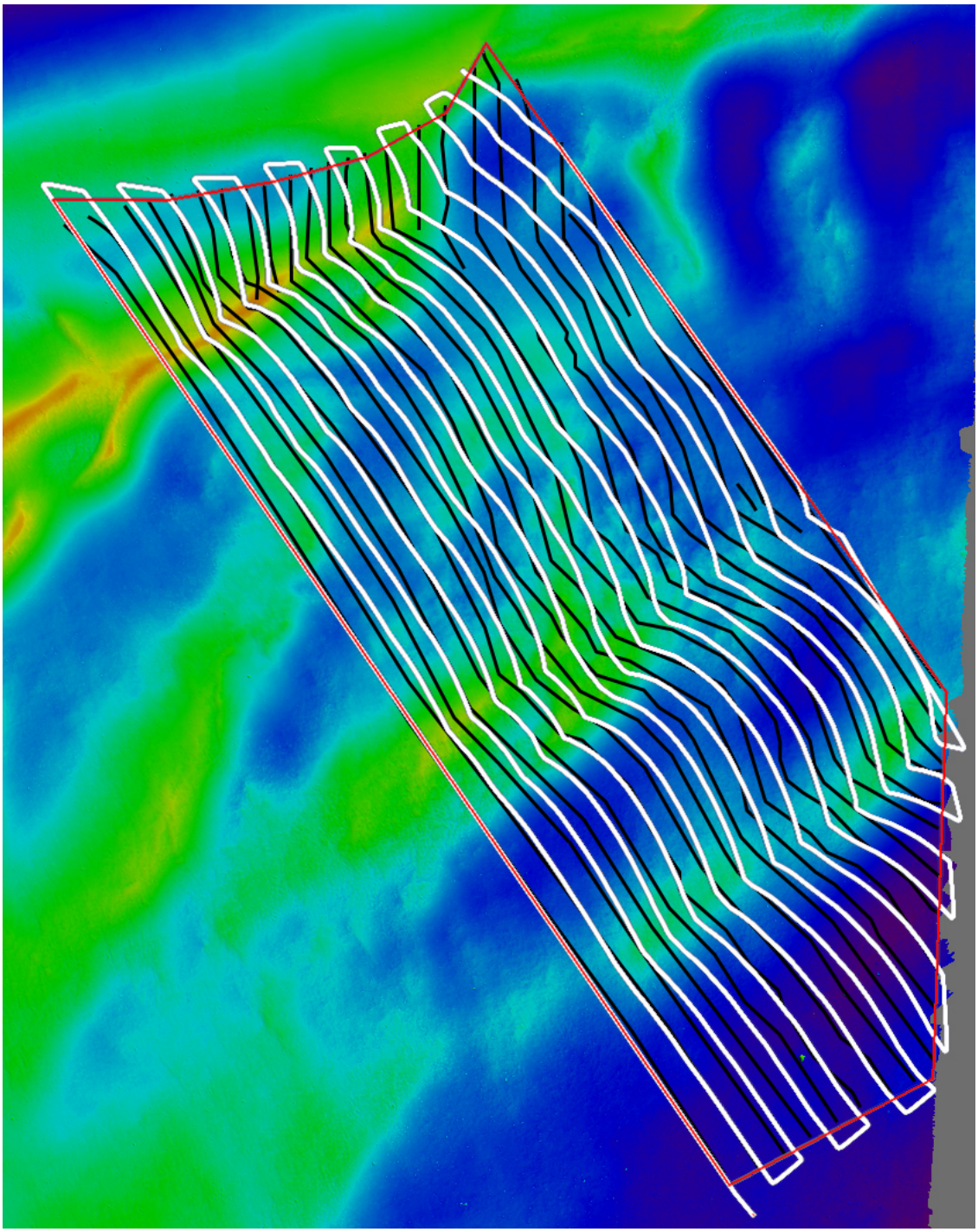

Figure 3.14: Surveyed polygon in H12450 from NOAA Ship *Rainier* launch near Chirikof Island, showing automated planning in white and human lines in black.

mated survey methods. The results are seen in Figures 3.15 and 3.16. Figure 3.15 shows a large but fairly flat region and Figure 3.16 shows and example with more relief and a non-rectangular

polygon shape. In both examples, the automated path planning reduced the distance traveled by the vessel by 23% over the human driven surveys. When combined with the other NOAA survey, this makes an average reduction of 22%. The survey distances and comparisons are summarized in Table 3.1.

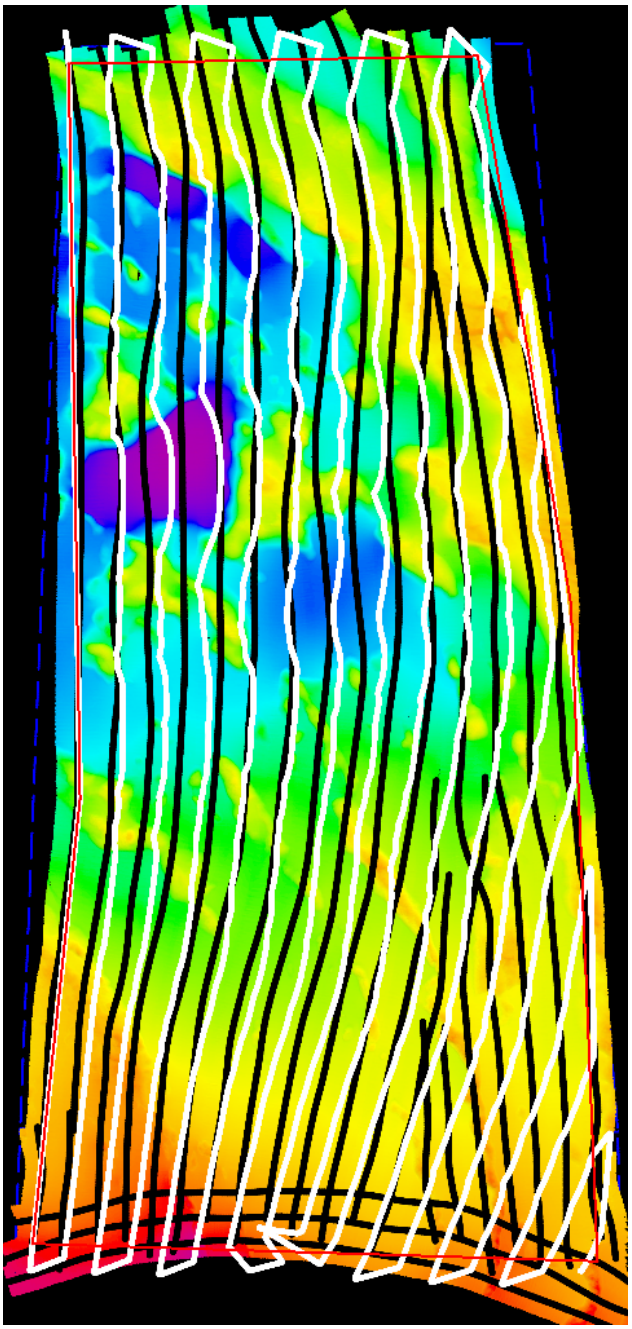

Figure 3.15: Surveyed polygon in H12758 from NOAA Ship *Fairweather* launch in the Shumagin Islands, showing automated planning in white and human lines in black.

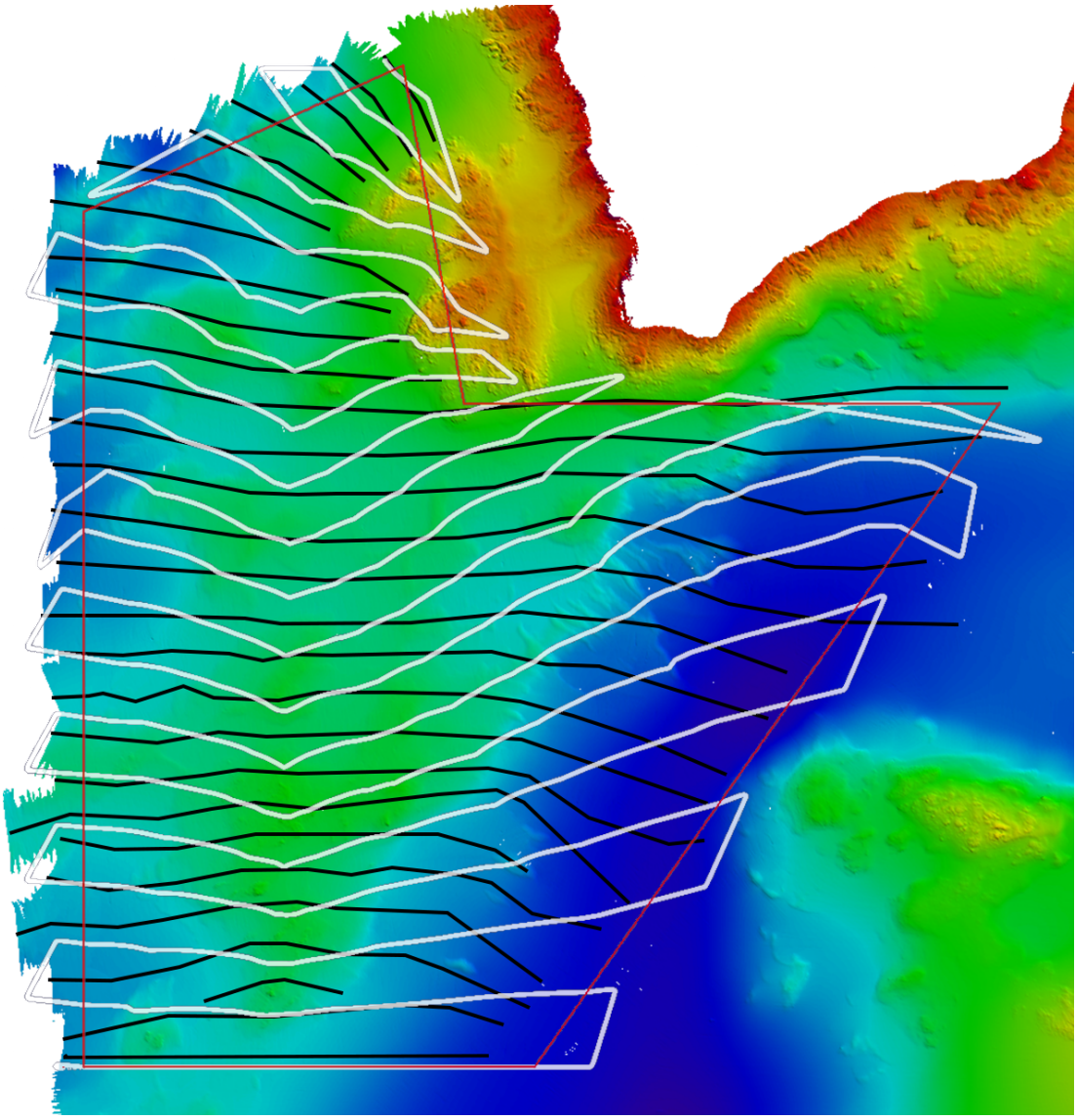

Figure 3.16: Surveyed polygon in H12472 from NOAA Ship *Rainier* launch in the Shumagin Islands, showing automated planning in white and human lines in black.

Survey	Human Survey [km]	Automated Survey [km]	Reduction	Time Reduction @ 7 kts [hrs]
Summer Hydro South	34.9	32.2	8%	0.2
Summer Hydro North	44.2	19.4	56%	2.0
H12450 Chirikof	71.0	56.8	20%	1.1
H12758 Shumagin *Fairweather*	169.0	130.8	23%	3.0
H12472 Shumagin *Rainier*	63.4	48.6	23%	1.2

Table 3.1: Comparison of survey methodologies in different regions

3.5 Field Testing Results

The path planning algorithm was able to be tested in the field during development on different Z-Boat vessels, with both single beam and multibeam mapping systems installed. Unfortunately, due to limited platform availability and hardware difficulties with the UNH ASVs, the final versions of the behavior are not able to be tested beyond simulations.

3.5.1 Single Beam Sonar Tests

While the algorithm is intended to be used with a swath sonar like a multibeam, it can also be tested with a single beam using the simulated swath angle option in pSonarFilter. While the vessel will not achieve full coverage with this scheme, it can be used to show the path a swath mapping vessel would take and visually verify the behavior versus what would be expected for a human operator. The first field tests were conducted on Z-Boats in conjunction with the NOAA Ship *Thomas Jefferson* at the Naval Station Newport in Newport, RI. These Z-Boats have a Teledyne Odom CV100 single beam sonar system installed, and through the module described in Section 1.3, depth data is passed to MOOS and the boat controlled to follow the planned paths.

At the time, the Z-Boats were new to the *Thomas Jefferson*, so operations were limited to the area around the piers where the ship docked to reduce risk from malfunctions. This area is dredged, and therefore very flat, so evenly spaced, straight paths could be expected. A rectangular operation region was designated for the survey within the area between two piers. The results of this survey from 28 August 2015 are shown in Figure 3.17.

This shows the depth map created from the single beam sonar data. As expected, a mostly linear path is followed. The survey had to be manually terminated before the final boundary was reached due to the presence of a barge in the designated region. To better visualize the autonomy system, a screenshot of the shoreside MOOS-IvP pMarineViewer monitoring window is shown in Figure 3.18 for a time toward the end of the survey mission.

Figure 3.18 shows the turn point and alignment line that are placed outside the survey region for the

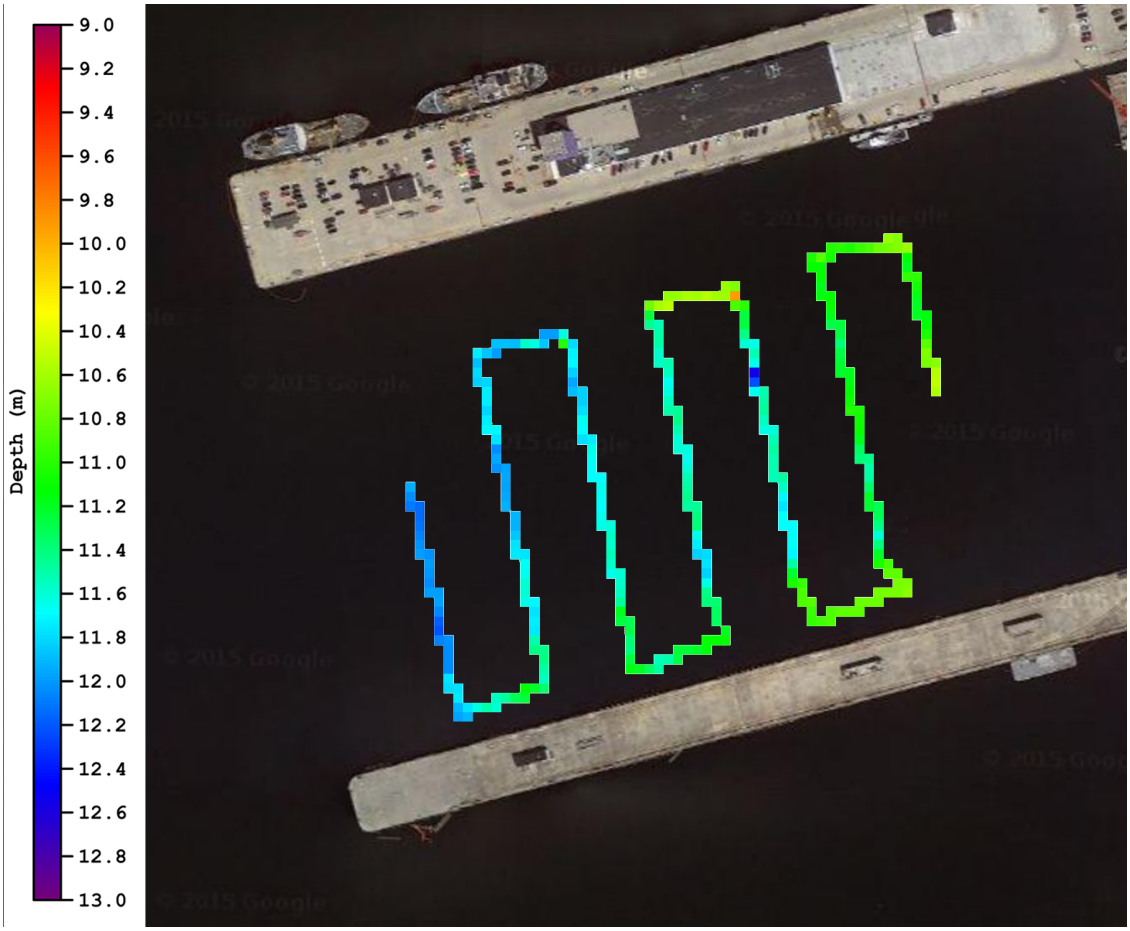

Figure 3.17: Automated survey path planning test at Naval Station Newport.

transition between the survey lines. While the paths are almost linear, the active line shows how it consists of multiple waypoints that are determined by the path planner from the sonar sensed depths of the previous line.

3.5.2 Multibeam Sonar Tests

A Z-Boat with a Teledyne Odom MB-1 multibeam sonar system was integrated with the autonomy module from Section 1.3 and operated around New Castle, NH in November 2015. Due to time constraints, no adaptively planned survey regions were completed, but data ingestion and vessel control by MOOS-IvP were verified. The same vessel was later operated at the Alliance for Coastal Technologies ASV Workshop in Solomons, MD. During the workshop, a demo day was held on 19 November where the Z-Boat ran adaptive path planning for its data collection. The region

Figure 3.18: MOOS-IvP pMarineViewer monitoring view of automated survey in progress. Operation region shown in red, current survey line in white and vessel track in yellow.

surveyed includes a channel with dynamic terrain, which better demonstrates the capabilities of the automated path planning. The weather conditions during this survey were fairly rough compared to the size of a Z-Boat, with about 0.3 m short period waves and winds up to 15 kts. Despite this, the boat was well controlled and yielded good data after some tuning. The results of the survey are shown in Figure 3.19.

The rough seas caused bubble sweepdown under the Z-Boat, leading to many data blowouts in the first portion of the survey (on the lower half of Figure 3.19). This affected the path planning, as multiple erroneously shallow measurements caused pSonarFilter to accept some incorrect depths. At these points, the subsequent path is planned very close to the previous one for some portions. This can be seen, for example, in the fifth survey line from the bottom of Figure 3.19. After some tuning of the sonar parameters, better results were obtained for the northern portion of the survey region, where the planning creates smoother lines with spacing expected for the depths. The

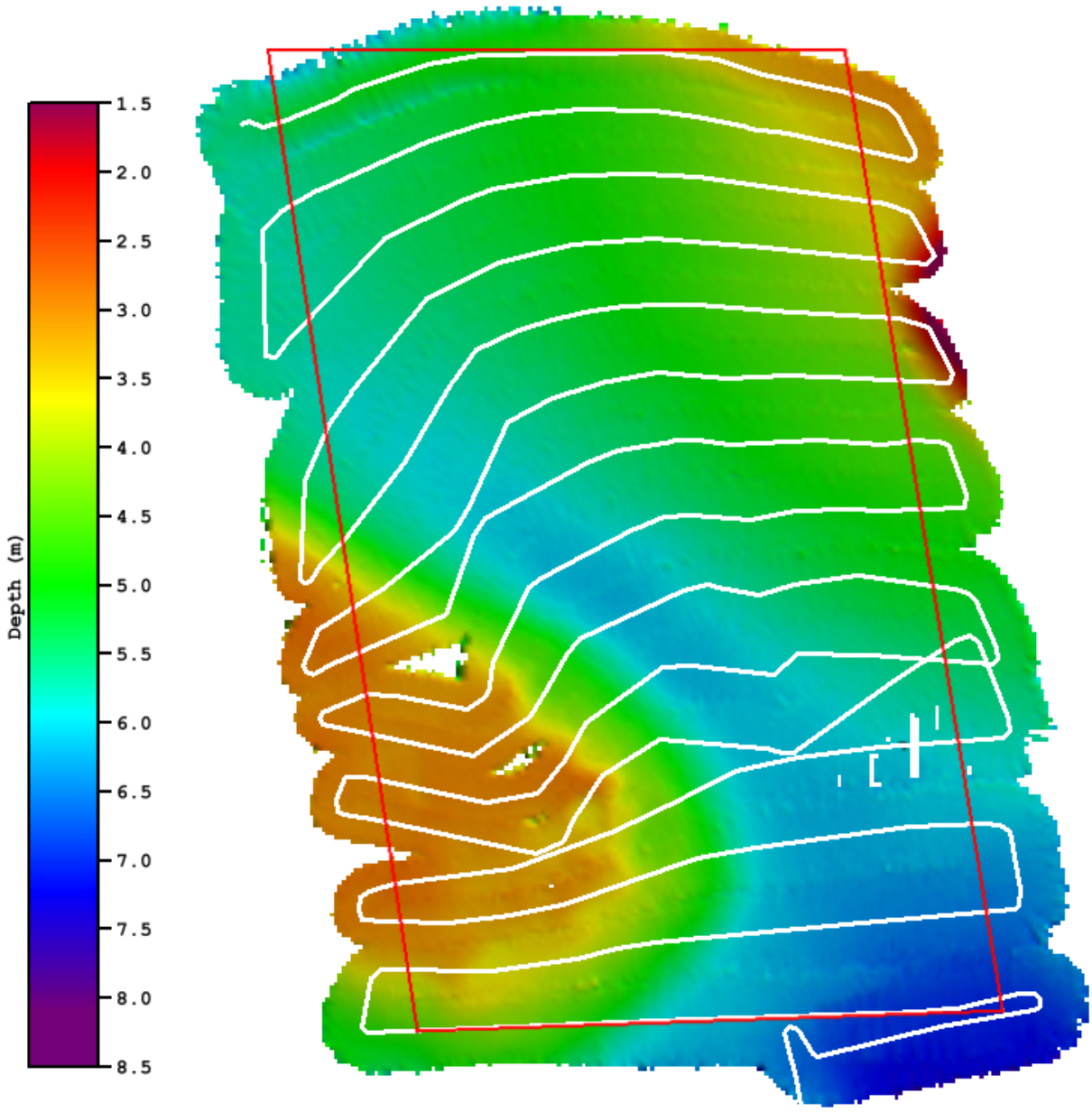

Figure 3.19: Automatically planned multibeam survey, showing survey region in red and vessel track in white.

holidays to the left side of the survey region are created by the sharp bend removal procedure of the path planning algorithm, and would have been incorporated into the coverage model. Therefore, they could have been addressed after the conclusion of the initial survey.

The survey data from this operation includes the turns and areas outside the designated region. This is a software limitation, as it is not currently possible to signal the commercial survey data

collection software (Hypack) to start and stop logging over a network or serial connection. In addition, the only output available at the time of survey provided the nadir (directly beneath the boat) depth, so the swath width had to be estimated. Discussions with Hypack representatives have yielded a method for transferring swath coverage and the possibility of future integration of automatic logging within a region and support for external logging commands.

NOAA full coverage requirements specify that each depth point in the final gridded product must have at least 5 individual soundings (sonar measurements) contributing to the calculated depth for greater than 95% of the grid cells [35]. In all areas where there are not holidays created by either blowouts or the path planning bend angle limit, the data density meets this criteria, as shown in Figure 3.20a. In addition, a scaled representation showing more detail on the range of data density is shown in Figure 3.20b. From this version, it is possible to see the amount of swath overlap, since these areas have slightly increased data density. The path planning algorithm adequately creates overlap throughout the survey, and is particularly effective at having minimal overlap in the northern portion where there is good quality input sonar data. Since it achieves the 5 sounding per node requirement with this small overlap, it is likely this survey is more efficient than a human driven one in the same area.

This survey reinforces the need for resurveying shallow, high traffic areas. In this busy port, a shoal was found that is not currently represented on NOAA nautical charts. On the raster chart (RNC), from which the survey was planned, the survey limits are deeper than the 6 ft contour on the eastern side. However, survey data revealed that both the channel and land in this area does not match the chart. The land outline is updated on the Electronic Navigation Chart (ENC), but the depths and contours are not, so they go through land at this location. The survey is shown in the context of these charts in Figure 3.21. It can also be seen that despite the shoal and land jutting into the surveyed area, the main channel has widened since the previous survey.

[Maybe include figure of the old survey from ACT paper]

Field tests of the path planning algorithm and associated MOOS-IvP behavioral structure show that its operation is robust to real world conditions and largely fault tolerant to intermittently er-

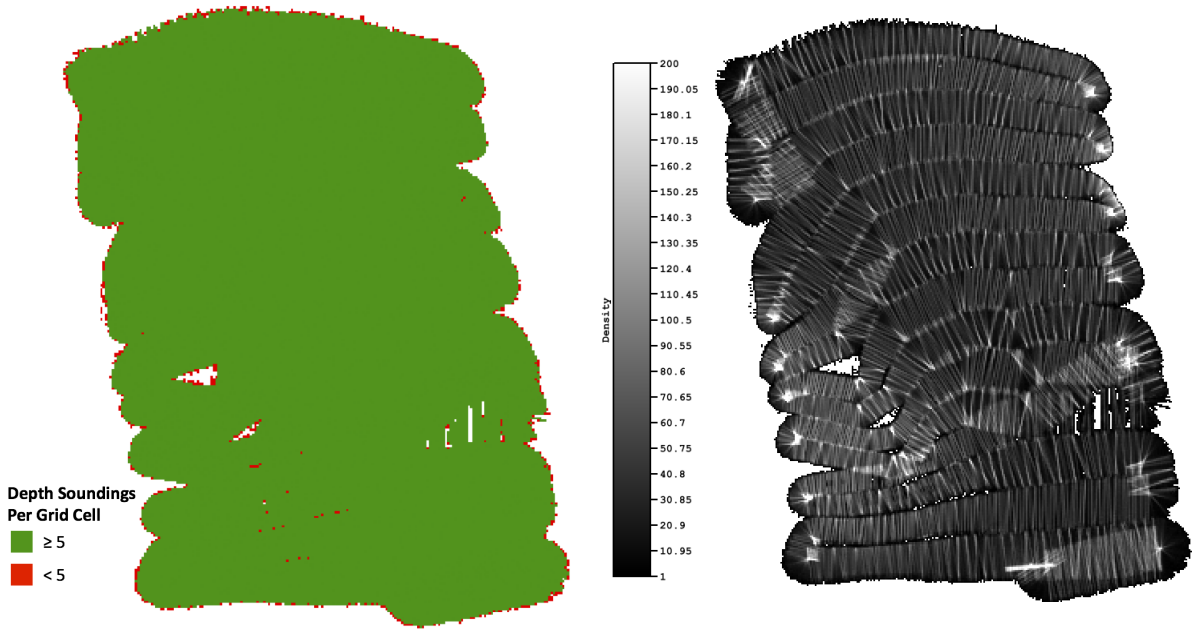

(a) Data density showing portion meeting NOAA specifications.

(b) Grayscale data density, showing swath edges and areas of overlap.

Figure 3.20: Data density information from multibeam sonar survey near Solomons, MD.

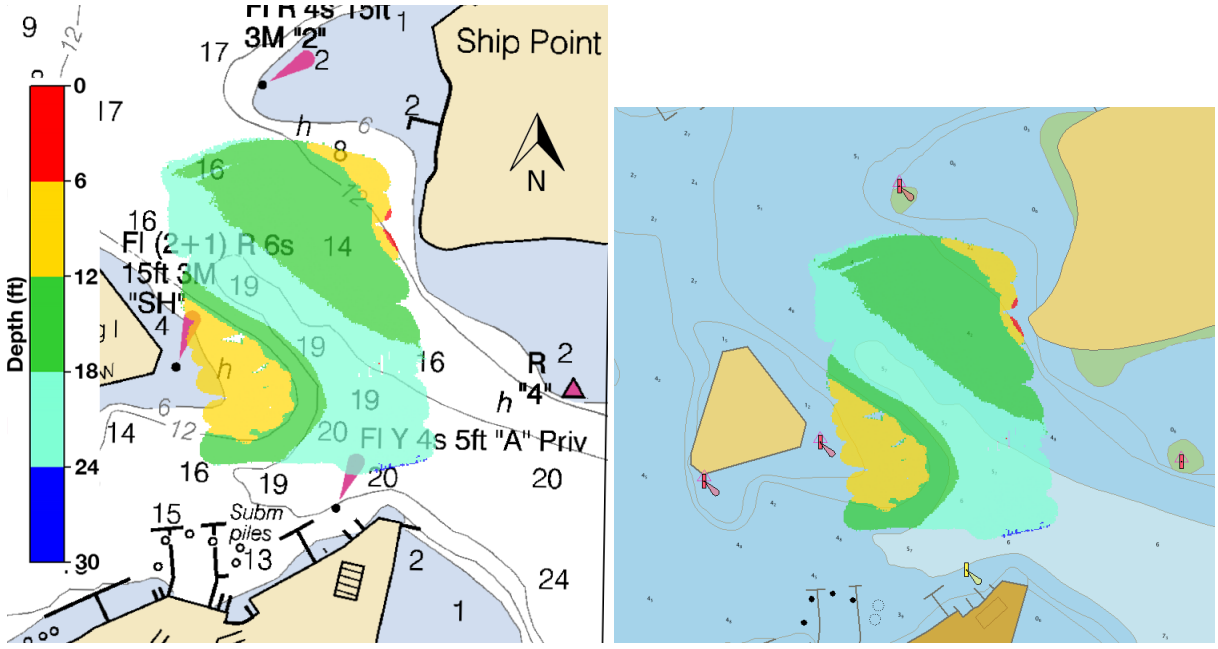

(a) Survey data over RNC, showing uncharted shoal in the north east.

(b) Survey data over ENC, showing updated land versus RNC, but uncharted shoal.

Figure 3.21: Chart representations of the area shown with survey data to illustrate changes since prior survey.

roneous data from the sonar system. Even when individual lines have mistaken trajectories due to poor data quality, future lines are able to recover and the survey completes satisfactorily. Additional reductions in data quality could compromise the performance, but under these conditions the sonar data would not be acceptable for charting either. With adequate quality data, the automated survey system can complete a designated polygonal region to meet NOAA specifications.

CHAPTER 4

CONTROL SYSTEM

Ship heading control systems have been an area of interest since the first gyrocompasses made accurate, electronically transferable heading measurements possible. Sperry and Minorski both applied PID type controls to ship steering in 1922, and many modern ship autopilots still have this system at their core [5]. Advancements have been made for steering large ships, which are mostly targeted at improving fuel efficiency for long transits and maintaining desirable turn characteristics under different loading and weather conditions. Only limited application of more advanced control systems have been investigated on smaller vessels like those used for this study, and most rely purely on simulation results.

To increase efficiency and reliability during survey operations, control systems were developed for heading and speed. By minimizing the actuations of turning mechanisms and maintaining more consistent thruster output, the endurance of the platforms is increased, allowing additional work to be completed on the same battery charge or amount of fuel. The heading control is based on designs for Model Reference Adaptive Control (MRAC) applied to larger ships, while the speed controller is custom designed to reduce the number of set-point changes in a variety of operational conditions.

4.1 Introduction to Control System Types

4.1.1 PID Control

Proportional-Integral-Derivative (PID) control is a standard methodology for control of dynamic systems. It is mathematically defined as given in Equation 4.1

$$c(t) = K_p e(t) + K_i \int_0^t e(\tau) d\tau - K_d \frac{de(t)}{dt} \tag{4.1}$$

where c(t) is the control output signal, and e(t) is the error between the system under control and the desired behavior. The proportional term (K_p) sets the output based on the currently known error, and the differential (K_d) and integral (K_i) terms provide anticipatory and historical error compensation, respectively. In physical terms for a vessel, the proportional feedback sets the initial non-zero desired rudder when a heading change is requested. As the vessel begins to turn, the differential feedback allows damping by reducing the desired rudder in proportion to the rate of turn. Finally, integral feedback compensates over time for static disturbances, such as rotational push from wind or an offset in the rudder positioning. Together, all the terms of the PID controller gives a defined characteristic to the response of the heading control and is able to compensate for both static and dynamic disturbances.

However, if the behavior of the vessel itself changes as a result of speed, thrust, or mass changes due to loading and fuel consumption, the PID controller gains will have to be changed to achieve the same response characteristic and avoid unwanted oscillation, course overshoot, or sluggish adjustment. With a simple addition to the PID controller and thorough testing under various conditions, gain schedules can be designed to compensate for some of these effects. However, this requires testing to be completed, which becomes increasingly difficult and time consuming with vessels that undergo many modifications, as is common on survey vessels with different sonar systems and other payloads. Therefore, an automatically adapting approach using model reference adaptive control is introduced.

4.1.2 Model Reference Adaptive Heading Control

Model reference adaptive control (MRAC) uses a mathematically defined model to approximate the behavior of the system under control, which in this case is the heading of the ship. The model is initialized with parameters close to those expected for the system and is continually fed mea-

surements of the inputs to the physical system, so that the model operates in parallel to the physical system. The differences between the model and the measured response of the system are used to adjust the model, which over time, should closely match the behavior of the physical system as long as the major dynamics are captured by the model [41]. The adjustment laws are derived to ensure stability in the system over time. The adaptation can be applied to either parameters of a model of the system or the feedback gains of the controller.

4.2 Implementation of MRAC

For this autonomy system, MRAC is implemented for heading control of the vessel. Two versions of a heading controller are implemented, which can be operated separately or as a hybrid combination. These two controllers are adapted from versions originally developed by Job Van Amerongen [2], [42]. Van Amerongen applied MRAC to larger ships (42 m to 168 m), for which two modes of operation were desirable. Throughout this section, the term rudder angle applies to both the physical rudder on systems with separate propulsion and rudder (common on larger vessels) as well as the angle of the thrusters or thrust nozzle on platforms where the thrusters are actuated (common on the smaller platforms of this study). The characteristics of each should be similar, with actuated thrusters likely performing closer to the simplified models due to less reliance on lift over the rudder for turning. Thrusters give a constant force at the angle to which they are turned, while rudders stall at high angles and do not provide a linear relationship between angle and force.

The controllers are implemented as part of the same MOOSApp, pMarineMRAS, which facilitates passing information when running in hybrid mode and simplifies deployment and configuration for users. The acronym MRAS in the application name refers to Model Reference Adaptive Systems, taking into account the multiple methods. The pMarineMRAS application subscribes to the desired heading and speed from the IvP Helm and uses measured heading and speed to provide feedback and control the vessel.

Both controllers use PID feedback to perform the rudder control, but use different methods to adjust the PID gains while operating. The PID control equation for each of the systems is the same, and provides feedback based on the measured and desired headings, as given in Equation 4.2.

$$\delta = K_p(\psi_r - \psi_p) - K_d\dot{\psi}_p + K_i \tag{4.2}$$

Each system initializes the feedback gains based on user supplied parameters, so if the adaptation is disabled by setting adaptive gains to zero the controllers will operate as fixed PID systems.

4.2.1 Course Change Controller

During large turn maneuvers, a specific transfer between the two headings is desired to be maintained, despite currents or waves that may be encountered during the turn. The turn starts with full rudder to begin the rotation of the ship, eases the rudder to where a desired rate of turn is maintained, and then applies counter rudder to end the turn without overshooting the desired heading. This behavior is shown in Figure 4.1.

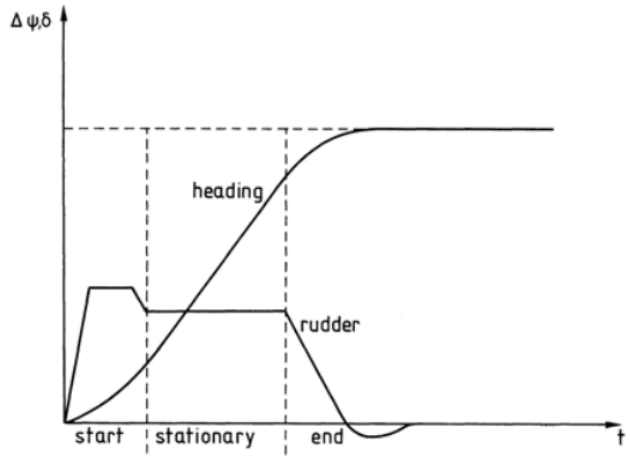

Figure 4.1: Course changing maneuver showing rudder and heading response. From Van Amerongen [2]

Theory

During the turn, it is important to maintain a specific path to ensure predictability of position, including advance and transfer, which is crucial to safe operation of large ships in narrow channels. To approximate the behavior of Figure 4.1, a second order transfer function relating the current and desired heading is chosen as the model and is based on a time constant (τ_m) and proportionality constant (K_{pm}) for the turn response. This is used as the model for the MRAC. This transfer function is given in Equation 4.3, where ψ_r is the desired (or reference) heading and ψ_m is the modeled heading for the desired characteristic of the boat.

$$\frac{\psi_m}{\psi_r} = \frac{K_{pm}/\tau_m}{s^2 + s/\tau_m + K_{pm}/\tau_m} \tag{4.3}$$

The time constant is chosen to be two to three times smaller than the time constant of the open loop ship turn dynamics (τ_s) at cruising speed, as it is assumed that rate feedback gain allows a similar change in the closed-loop system [42]. The proportionality constant can be derived from the damping ratio of the system, providing an analytical way to create the desired response. Using the coefficients of the transfer function in Equation 4.3 and comparing to a standard second order transfer function in the form

$$G(s) = \frac{\omega_n^2}{s^2 + 2\zeta\omega_n s + \omega_n^2} \tag{4.4}$$

the relationship is given as

$$K_{pm} = \frac{1}{4\zeta\tau_m} \tag{4.5}$$

The damping ratio controls the settling behavior of the turn. If $\zeta < 1$, the system is underdamped and oscillates, but reaches the set point crossing quickly. If $\zeta = 1$, the system is critically damped and it changes as quickly as possible without overshoot. Finally, if $\zeta > 1$, the system is overdamped and slowly approaches the set point without any overshoot. Some examples of these characteristics are shown in Figure 4.2.

The values of the constants used in Equation 4.3 are gain scheduled based on the speed of the

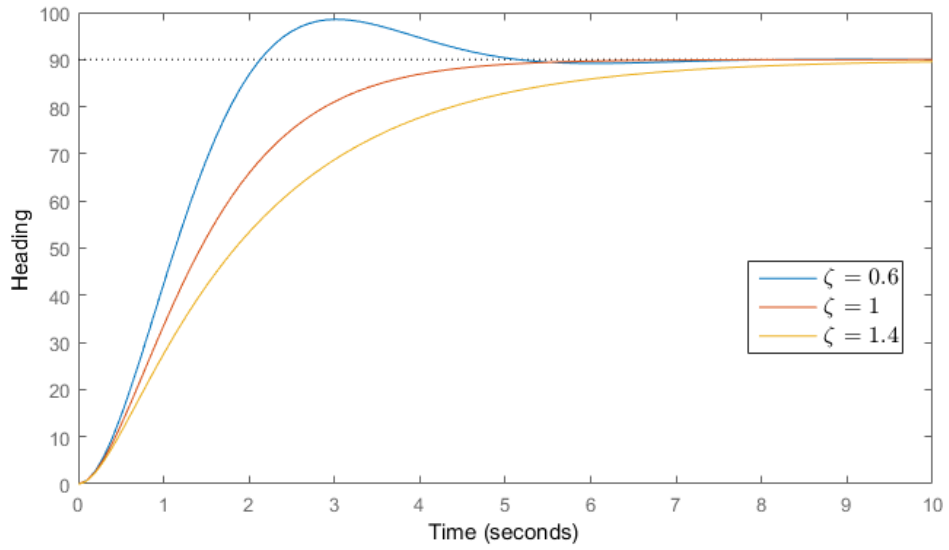

Figure 4.2: Effect of ζ on overshoot and settling, with example heading change of 90°.

vessel (U) as a ratio to the length of the vessel (L) using the relationships given in Equations 4.6. This accounts for the effect that higher thrusts will lead to greater rates of turn for the same rudder angle. These values, along with the desired damping ratio, form the initial conditions for the model reference in the control system.

$$K_{pm} = K^* \frac{U}{L}$$
$$\tau_m = \tau^* \frac{U}{L} \tag{4.6}$$

In these equations, K^* and τ^* are constants specific to the vessel, and must be determined through experimentation. For large vessels, Van Amerongen recommends values of 0.5 - 2.0 for K^* and τ^*. For the smaller vessels characterized for this study, the range was found to extend lower for τ^* and stay on the higher end for K^*. This corresponds to the fact that these platforms have lower moments of inertia for yaw and are able to turn more quickly at maximum rates. From results of the Z-Boat and small ASVs at UNH, recommended values for small ASVs are 0.2 - 1.0 for τ^* and 1 - 2 for K^*. Details for the ASVs in this research are presented in Table 4.2.

The gains of the PID controller must be initialized to a point from which to start the adap-

tation, which are intended to give the same response as the heading change transfer function in Equation 4.3 if the system is fully and correctly characterized. The presence of unknowns or differences in reality drive the need for an adaptive controller. The PID gains are therefore set using the variables dictating the reference model response, as given in Equations 4.7 - 4.9.

$$K_{p0} = \frac{U_0}{U} \qquad K_{p0} \leq 5 \tag{4.7}$$

$$K_{d0} = \frac{L}{U}\frac{2\zeta\sqrt{K_{p0}K^*\tau^*} - 1}{K^*} \qquad K_{p0} \leq K_{d0} \leq K_{p0}\frac{L}{U} \tag{4.8}$$

$$K_{i0} = \begin{cases} K_{i,m} & \text{Hybrid controller} \\ 0 & \text{Initial run, single controller} \end{cases} \qquad |K_{i0}| \leq 10\frac{U_0}{U} \tag{4.9}$$

where the subscript 0 indicates the initial condition, and U_0 is the standard operation speed of the vessel (survey speed). The integral gain is set to 0 when first initialized or if the course change controller is used alone. In the hybrid arrangement, it takes the most recent value from the course keep controller when initiating a turn. The limits on the gains are enforced to ensure that the controller output is bounded so that periodic increases in noise do not result in spikes in PID gains.

Once the initial values are set for the controller, adaptation is performed by laws given in Van Amerongen's design. The adjustment laws are given in Equations 4.10 - 4.12. For this adaptation process, the laws were designed using a Lyapunov stability method with a quadratic Lyapunov error function. A proof of this Lyapunov function can be found in Van Amerongen 1981 [41]. The parameters of the PID controller are directly modified to shape the response of the ship to match the desired transfer function. The adaptive laws each have a gain which controls the speed of adaptation: β, α, and γ. They are positive, and usually set to be very small. Results from simulation determine that maintaining these constants on the order of 0.0001 yields the most accurate adaptation behavior.

$$\frac{dK_p}{dt} = \beta\left(p_{12}e + p_{22}\dot{e}\right)\varepsilon \tag{4.10}$$

$$\frac{dK_d}{dt} = -\alpha\left(p_{12}e + p_{22}\dot{e}\right)\dot{\psi}_p \tag{4.11}$$

$$\frac{dK_i}{dt} = \gamma\left(p_{12}e + p_{22}\dot{e}\right) \tag{4.12}$$

where ε is the heading error and e is the error between the model and measurements such that

$$\begin{aligned} e &= \psi_m - \psi_p \\ \varepsilon &= \psi_r - \psi_p \end{aligned} \tag{4.13}$$

and their derivative is

$$\dot{e} = \dot{\psi}_m - \dot{\psi}_p \tag{4.14}$$

The terms p_{12} and p_{22} are elements of a matrix $\mathbf{P}$, which is defined such that

$$\mathbf{A_m^T P} + \mathbf{P A_m} = -\mathbf{Q} \tag{4.15}$$

where $\mathbf{A_m}$ is the system matrix for the reference model in Equation 4.3, and $\mathbf{Q}$ is an arbitrary positive definite matrix. The state space representation of the system for the transfer between model and desired heading is given as

$$\underbrace{\begin{bmatrix} \dot{\psi}_m \\ \ddot{\psi}_m \end{bmatrix}}_{\dot{x}_m} = \underbrace{\begin{bmatrix} 0 & 1 \\ -\frac{K_{pm}}{\tau_m} & -\frac{1}{\tau_m} \end{bmatrix}}_{A_m} \underbrace{\begin{bmatrix} \psi_m \\ \dot{\psi}_m \end{bmatrix}}_{x_m} + \underbrace{\begin{bmatrix} 0 & 0 \\ \frac{K_{pm}}{\tau_m} & 0 \end{bmatrix}}_{B_m} \underbrace{\begin{bmatrix} \psi_r \\ 1 \end{bmatrix}}_{u} \tag{4.16}$$

Using $\mathbf{A_m}$ from Equation 4.16 and $\mathbf{Q} = 2\mathbf{I}$, Equation 4.15 can be solved for $\mathbf{P}$. The choice of $\mathbf{Q}$ dictates the magnitude of the elements of $\mathbf{P}$, but since each adaptive law has a gain, the values of these would be adjusted and the same results obtained during adaptation.

$$\mathbf{P} = \begin{bmatrix} \frac{1}{K_{pm}} + K_{pm} + \tau_m & \frac{\tau_m}{K_{pm}} \\ \frac{\tau_m}{K_{pm}} & \frac{\tau_m^2}{K_{pm}} + \tau_m \end{bmatrix} \tag{4.17}$$

The elements p_{12} and p_{22} extracted from this matrix are used in Equations 4.10 and 4.11 for the adaptation of the PID controller. The full course change controller structure is shown in Figure 4.3.

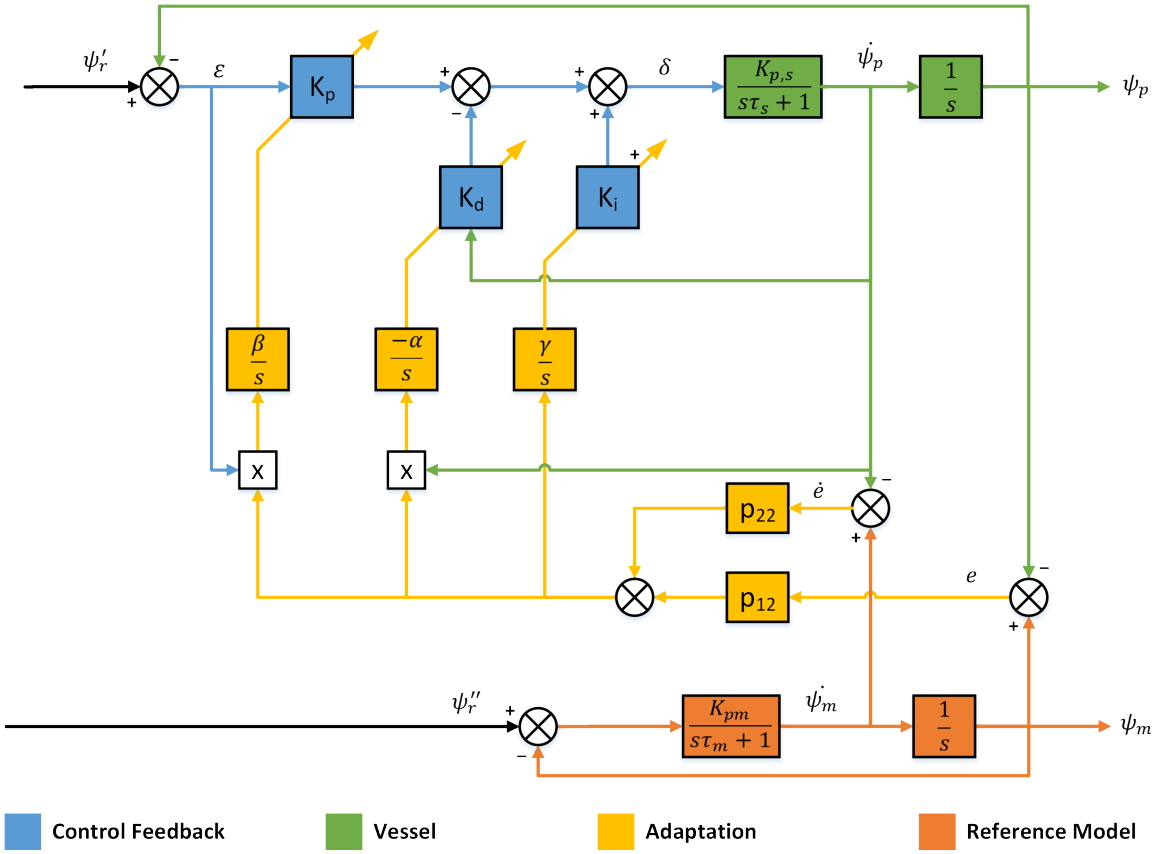

Figure 4.3: Course change controller block diagram.

Implementation

The core of the course change controller program implements the the equations of Section 4.2.1 through numerical integration and differentiation where appropriate. However, additional details are required for practical implementation of the course change MRAC. The transfer function in Equation 4.3 does not take into account any nonlinearities or limits of the physical system, so some of the major ones are accounted for through use of a series model with outputs that replace

the desired heading input ψ_r in Figure 4.3 for both the PID controller and MRAC model. The series model enforces absolute limits on rate of turn (ROT) and the angle of the rudder. The series model is shown in Figure 4.4.

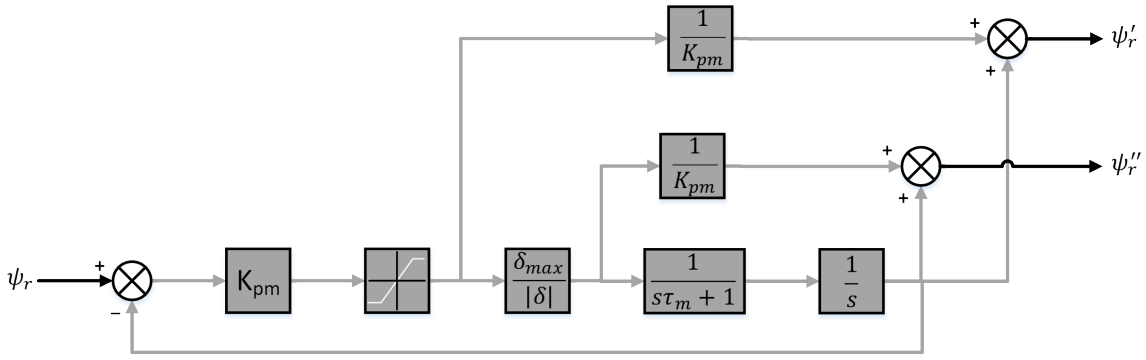

Figure 4.4: Course change controller series model for modification of reference input.

The rate of turn limiter sets a configurable maximum on the rate of turn, which should correspond to what is possible for the vessel, or a lower value if there is a desire to limit the rate of turn. The output from the ROT limiter (ψ_r') is used as the input to the PID controller. The ROT limited signal is then passed through a stage which accounts for the physical limits of rudder movement, using a ratio (f) between an unrestricted desired rudder angle out of the PID controller (δ) and the maximum rudder (δ_{max}), to give a continuous response at larger desired rudder angles. The ratio is capped to a maximum of 1, as there is no need to modify the reference heading when the desired rudder angle is physically possible. This relationship is summarized in Equation 4.18.

$$f = \frac{\delta_{max}}{|\delta|}, f \leq 1 \tag{4.18}$$

In addition to this limit on the rate of turn from physically unreasonable rudder values, the desired rudder output of the control system to MOOS is also limited to $\pm\delta_{max}$.

Since the adaptation in this controller is based on a defined transfer curve between the starting and desired heading for a turn, it provides no benefit to continue the adaptation after the turn, as the model will always converge the desired heading, while the vessel will be affected by waves and other disturbances which cause changes in heading. This leads to K_d growing without bound,

which can be seen from Equation 4.11. When the model has converged to the desired heading and the vessel heading approaches the desired heading, e is small and $\dot{e} = -\dot{\psi}_p$, since the model ROT is zero. This results in the adaptation of K_p becoming proportional to the square of the measured ROT $\dot{\psi}_p$, so K_d always increases while driving straight lines such that

$$\begin{aligned} \frac{dK_d}{dt} &\approx -\alpha p_{22} \left(-\dot{\psi}_p\right) \dot{\psi}_p \\ &= \alpha \tau_m \left(1 + \frac{\tau_m}{K_{pm}}\right) \dot{\psi}_p^2 \end{aligned} \tag{4.19}$$

To counteract this effect, the effect of the adaptation laws for both K_p and K_d are reduced over time by multiplying the adaptive gains β and α by a factor that decreases over time such that

$$\begin{aligned} \alpha &= \alpha_0 \frac{\xi}{1+T} \\ \beta &= \beta_0 \frac{\xi}{1+T} \end{aligned} \tag{4.20}$$

where T is the time since the start of the turn, and ξ defines the rate of decrease of adaptation. For the rapidly turning Z-Boat, values of ξ in the range 0.9 - 1.1 are found to be most suitable. The speed of reduction can also be controlled during operation by the magnitude of the heading difference and the expected time for the vessel to complete the turn. In this case, ξ is set during the initiation of a turn.

The final control parameter determines when the change in desired heading is large enough to begin the adaptation process. Unlike larger ships under human command, where heading orders are given fairly infrequently, the IvP Helm in these autonomous vessels continuously updates the desired heading. A threshold is set at 10° for a heading change indicating a new course where adaptation is to be initiated, as opposed to using the existing PID gains. A higher setting of up to 45 degrees would be relevant for the operation of small boats in complex scenarios or rough seas. When the threshold is reached between two subsequent iterations of the course change controller, the PID control gains are reset according to Equations 4.7, 4.8, and 4.9. This causes the adaptation process to be triggered when the IvP Helm jumps discretely between decisions, such as during a

turn between two lines of a lawnmower pattern or the activation of a new behavior, and standard PID action is to be maintained for the small adjustments required when following a line or driving to a waypoint.

4.2.2 Course Keep Controller

When maintaining a constant heading, as would occur on long transit legs, rudder action should be minimized, since oscillation around a desired heading adds length to the path and decreases speed, both of which lead to decreased efficiency. Since many of the vessels automated in this study use battery packs that provide relatively limited operating durations, any increase in path following efficiency means that more area can be surveyed with the same battery charge. To control the vessel most accurately, a model for how the vessel responds to changes in rudder is required so that the response can be tuned.

Theory

A simple linear model first presented by Nomoto [43] is used to represent the rate of turn of the vessel. The model is defined as

$$\tau_s \ddot{\psi}_m + \dot{\psi}_m = K_s (\delta - K_{i,m}) \tag{4.21}$$

This model defines the maximum rate of turn as $\dot{\psi}_{max} = K_s \delta$, which will be approached exponentially with time constant τ_s. This is easily observed from the equivalent time domain model

$$\dot{\psi}_m (t) = K_s \delta \left(1 - e^{\frac{t}{\tau_s}}\right) \tag{4.22}$$

As with the course change controller, the parameters of the model are gain-scheduled with respect to speed as given in Equation 4.23. This relies on the assumption that greater turn rates occur at higher speeds (a phenomenon observed in the experimental results with the small ASVs

of this study).

$$K_s = K_s^* \frac{U}{L}$$
$$\tau_s = \tau_s^* \frac{L}{U} \tag{4.23}$$

Unlike the course change controller, the model constants are directly adjusted for the course keep controller, resulting in the structure shown in Figure 4.5. This structure is known as a parameter identification MRAS, since it fits model parameters to the behavior of the vessel.

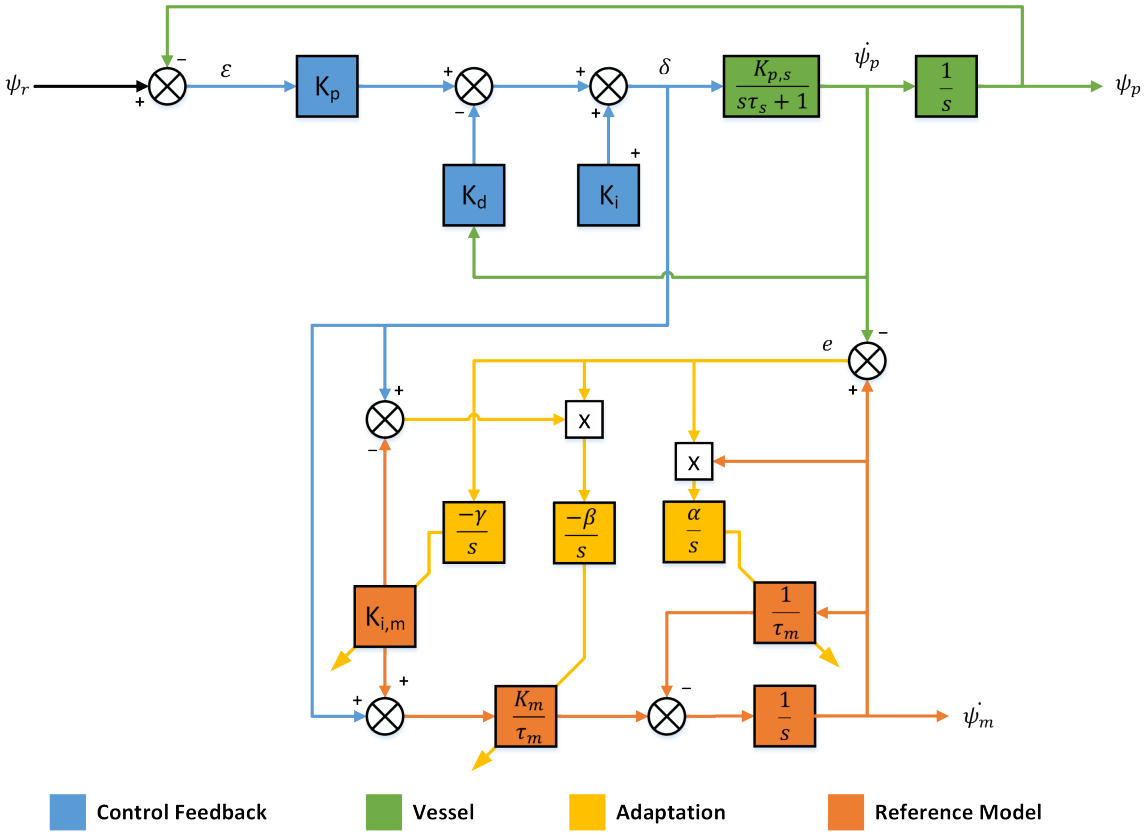

Figure 4.5: Course keep controller block diagram.

The adaptive laws are again derived using a quadratic Lyapunov function. The model first order (scalar) model is given as

$$\underbrace{\begin{bmatrix} \ddot{\psi}_s \\ \dot{\psi}_s \end{bmatrix}}_{\dot{x}_s} = \underbrace{\begin{bmatrix} -\frac{1}{\tau_s} \end{bmatrix}}_{A_s} \underbrace{\begin{bmatrix} \dot{\psi}_m \end{bmatrix}}_{x_s} + \underbrace{\begin{bmatrix} \frac{K_s}{\tau_s} \end{bmatrix}}_{B_s} \underbrace{\begin{bmatrix} \delta \end{bmatrix}}_{u} \tag{4.24}$$

The scalar state space equations mean that the **P** matrix also becomes a scalar, so to satisfy the

Lyapunov condition that $A_s P + P A_s = -Q$, one obtains

$$P = \frac{Q\tau_s}{2},\ Q > 0 \tag{4.25}$$

All of the constants in Equation 4.25 are positive, so P will always be a positive constant. Therefore, P can be consolidated into the adaptive gains, resulting in the following adaptive laws:

$$\frac{d}{dt}\left(\frac{K_s^*}{\tau_s^*}\right) = -\beta e\,(\delta - K_{i,s}) \tag{4.26}$$

$$\frac{d}{dt}\left(\frac{1}{\tau_s^*}\right) = \alpha e \dot{\psi}_s \tag{4.27}$$

$$\frac{d}{dt}\left(K_{i,s}\right) = -\gamma e \tag{4.28}$$

where

$$e = \dot{\psi}_s - \dot{\psi}_p \tag{4.29}$$

and the adaptive gains are again small (on the order of 0.0001). The initial values for K_s^* and τ_s^* are user defined and should be estimated from characterization trials of the vessel. Unless the rudder is known to be physically offset from the hull axis when set to zero angle, $K_{i,s}$ is initialized to 0. While the adaptation system is designed to adjust these time-varying parameters, the initial operation will not be correct unless the parameters are chosen to be near the known characteristics of the vessel. Incorrect initialization can lead to instability in the PID control of the vessel, in which case the adaptation will likely fail.

While the adaptation law in Equation 4.28 provides for direct calculation of the integral gain for the PID controller, the other laws determine the open loop dynamics of the vessel, which can then be used to create desired behavior when under control. Using the PID control Equation 4.2 and approximating the vessel response with the model parameters, the controlled rate of turn is

$$s\psi_p = \frac{\delta K_s}{s\tau_s + 1} = \frac{K_s\left(K_p\left(\psi_r - \psi_p\right) - sK_d\psi_p + K_i\right)}{s\tau_s + 1} \tag{4.30}$$

where $s\psi_p$ is the rate of turn of the vessel. If K_i is properly compensating for long term effects of wind, current, or rudder inaccuracy, it will not affect individual turns, so it can be assumed to not affect the transfer function. Using this and solving for the transfer between desired and controlled ship heading gives the following transfer function:

$$\frac{\psi_p}{\psi_r} = \frac{K_p K_s/\tau_s}{s^2 + s\left(1 + K_d K_s\right)/\tau_s + K_p K_s/\tau_s} \tag{4.31}$$

This determines the response of the ship when it is given a new heading input, which can be modeled as a step input since it changes instantaneously. Through comparison to the standard format second order transfer function given in Equation 4.4, the parameters can be determined with respect to natural frequency and damping ratio. Since the natural frequency and damping ratio dictate the shape of the response to inputs, these can be used to calculate values for the PID control gains, which will cause the vessel to respond accordingly. Solving for the PID gains gives

$$K_p = \frac{\omega_n^2 \tau_s}{K_s} \qquad K_p \leq 2.5 \tag{4.32}$$

$$K_d = \frac{2\zeta\sqrt{K_p K_s \tau_s} - 1}{K_s} \quad 0 \leq K_d \leq K_{p0}\frac{L}{U} \tag{4.33}$$

$$K_i = K_{i,s} \tag{4.34}$$

Note that Equation 4.33 is the same as Equation 4.8, since they both dictate responses based on the characteristics of the system. The physical interpretation of the damping ratio ζ is straightforward and has the same effects described in Section 4.2.1. As long as the other parameters are determined, it is independent of the vessel itself and only determines the overshoot characteristic of the response. The natural frequency is related to how quickly the vessel can yaw but is specific to the vessel and difficult to measure directly. It dictates the speed of response, with higher ω_n corresponding to a quicker turn. However, just as with the τ_m of the course change controller, it is possible to specify a value which is too fast to be physically achieved by the vessel. As such, some experimentation is required during implementation of the controller on a new vessel. Van Ameron-

gen suggests that for large vessels, ω_n should be approximately equal to the ratio of the ships speed to length [2], but this is found to not be true for the smaller vessels tested in this research. Some examples of how the response between headings changes are given in Figure 4.6.

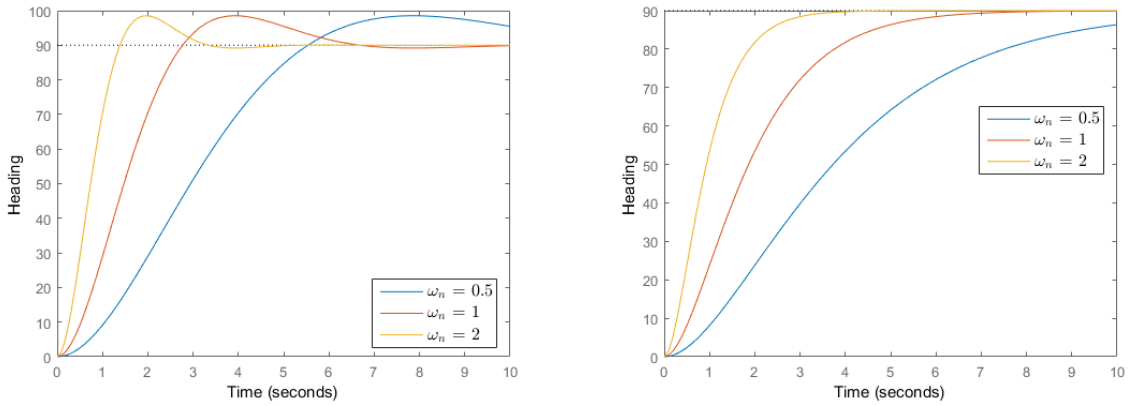

(a) $\zeta = 0.6$ (b) $\zeta = 1.0$

Figure 4.6: Effect of ω_n with varying damping ratios during a heading change of 90°.

Implementation

Similarly to the Course Change controller, some additional considerations are necessary for implementation of the Course Keep controller. Since the only external excitation to the model is the rudder, the model only accounts for yaw motions which are driven by the rudder. Any environmental disturbances to the vessel from waves or wind will not be reflected in the model, creating a rate-of-turn error through Equation 4.29, and therefore causing incorrect adaptation of the model parameters. On larger vessels, this effect can be partially removed through low pass filtering of the heading rate-of-turn signal, since excitations from the rudder are of lower frequency than those by waves. Low pass filtering also minimized the effect of high frequency noise that is present in some lower cost inertial measurement systems used to determine heading. Particularly for the second reason, the ability to use a low pass filter on the ROT is included in the control system. However, it is found that frequency separation of rudder and wave effects is not always possible on small vessels, which respond particularly quickly in the case of movable thrusters. Of the tested vessels, it is

most difficult to differentiate the frequencies for the Z-Boat, as it has the ability to generate rudder driven oscillations up to about 1.3 Hz. The frequency spectra of selected tests for the Z-Boat and ASV3 are shown in Figure 4.7.

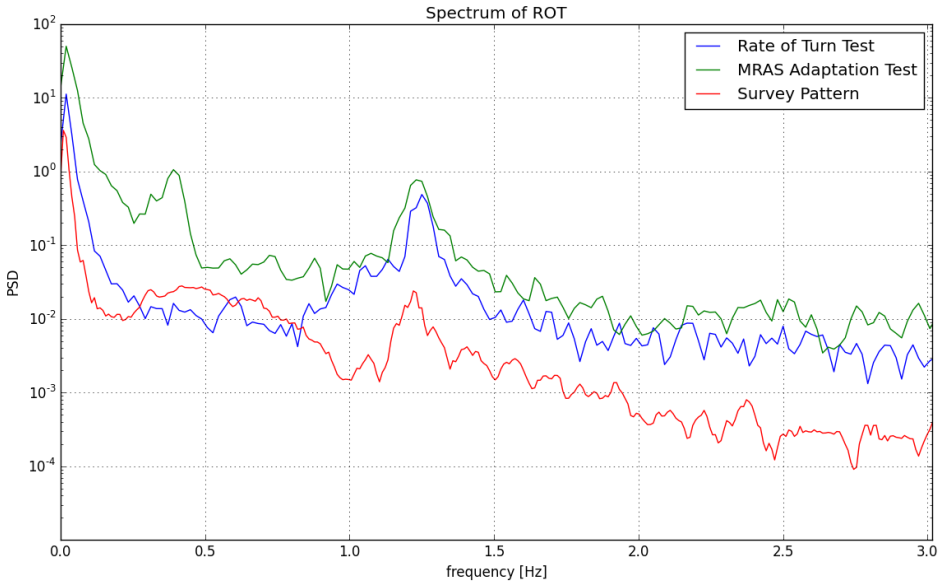

(a) ASV3

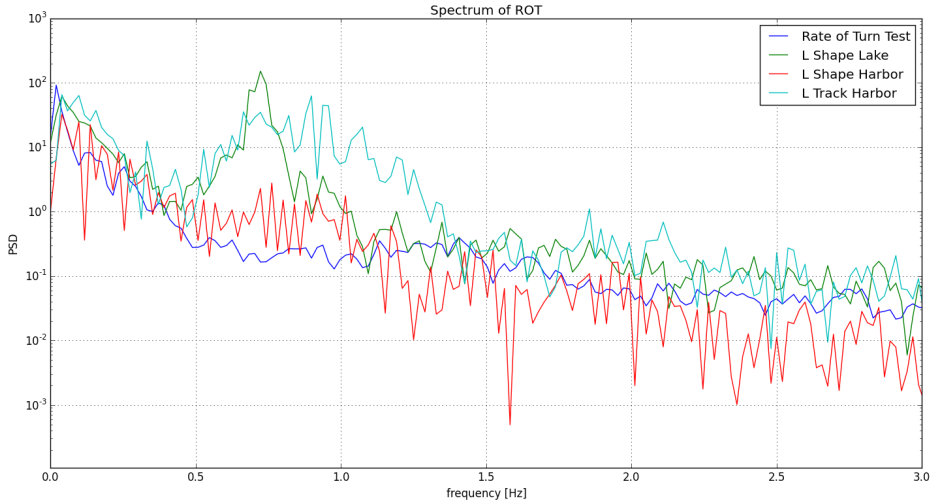

(b) Z-Boat

Figure 4.7: Power spectra of various trials with different vessels, exhibiting characteristics of the vessels, environment and measurement noise.

For both of the vessels, low frequency components dominate, which result from the turns that

have periods in the multi-second range ($< 0.5\,\text{Hz}$). In the MRAS adaptation test plot for ASV 3 in Figure 4.7a, a second distinct low frequency component corresponding to an oscillatory behavior of the rudder when course keeping is seen with a peak at 0.4 Hz. This is still easily separable from the measurement noise introduced by the low quality IMU, which causes the peak around 1.25 Hz, and a low pass filter with a cutoff frequency of 0.65 Hz can be used. For the Z-Boat, through comparison with rudder plots, the higher frequency components present between 0.6 and 1.3 Hz are caused by oscillation of the rudder, and little noise is present around these frequencies due to the use of a more accurate heading sensor. However, this frequency also corresponds to that of wave motion exciting the vessel, so it is difficult to separate the two motions with a low pass filter. A low pass filter with a cutoff frequency of 1.3 Hz is nonetheless found to improve noise rejection and performance of the adaptation process.

To further minimize the effect of environmental disturbances on incorrect adaptation, adaptation is only enabled during maneuvers where the rudder is over a limit chosen a priori. This ensures a high the signal-to-noise ratio (SNR) of the rudder signal, as motions caused when the rudder is at a small angle are dominated by environmental effects and unmodeled nonlinearities not included in the simple model of Equation 4.21. For the purpose of most experiments, the minimum rudder is selected to be 25% of the maximum rudder. Conversely, $K_{i,s}$ is chosen to not adapt during turns, as this could incorrectly cause wind up due to extended large rudder angles in the presence of error.

K_p and K_d are not updated during turns so that the characteristic of a large turn is not affected by adaptation during that turn. Instead, they are recalculated from the adjusted K_s and τ_s after the turn has settled. The settling time is chosen to be $7\tau_s$ to ensure that it is close to the final heading if the model is correct. In addition, the speed used for Equation 4.23 is set with a lower bound of $0.5\text{m}/\text{s}$ to eliminate unrealistically large τ_s as the speed approaches zero. At slow speeds, the effect of K_s reaching zero must also be avoided to prevent singularities in Equations 4.33 and 4.32. The effect of this limit is shown in Figure 4.8. In addition to these limits, K_p and K_d are independently limited according to Equations 4.32 and 4.33.

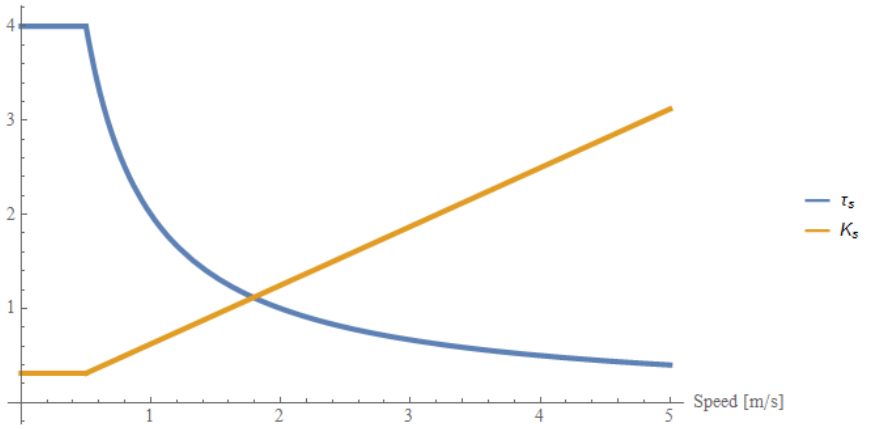

Figure 4.8: Relationship between τ_s and K_s and speed of the vessel, showing minimum limit of $U = 0.5\,\mathrm{m/s}$. For this example $L = 2.5$, $K_s^* = 1.56$, $\tau_s^* = 0.8$.

4.2.3 Hybrid Heading Control System

In addition to being able to run each control system separately, the course keep and course change control systems may be combined into a hybrid system. Under this mode of operation, the course change controller is used to enact large turns, which are defined as course changes of more than 20°. While conducting the turn, the course keep controller is run in parallel, but the output is ignored so that it can adapt while the SNR is high. The course keep controller is allowed to steady the heading (with decreasing adaptive gains) until the same settling time as defined above ($7\tau_s$) is reached. The course keep controller is then selected for output, as the course change controller would otherwise result in a static PID controller as the adaptive gains approach zero.

4.3 Speed Control

The MRAC combined with PID approach works well for heading control where continual response to conditions with respect to the desired direction is necessary for reliable operation of a vessel. In many circumstances, it is not as critical to maintain an exact speed, and doing so can lead to detrimental performance in other metrics such as power consumption. For example, while surveying an approximate speed may be maintained while the effects of waves and currents modify

it slightly. As long as the speed is within the limits of the sonar system to produce good quality, dense data, it does not matter if the speed is maintained within tight limits. Allowing the speed to vary a small amount without compensation is preferable so that the engine or thrusters are not constantly adjusting and therefore drawing more current or using fuel to compensate for periodic effects that naturally reverse in direction.

To handle these circumstances while still providing adequate control for operations where continual speed adjustment is unnecessary, a new speed control system is developed. The control system incorporates stages of adjustment that allow it to respond quickly to speed changes while not adversely reacting to short period disturbances. It also estimates environmental effects in order to better predict speeds when turning and alert the system to possible mechanical failures.

In order to properly function, tests of the vessel speeds corresponding to the range of possible thrust conditions are required. This can be done fairly simply by measuring the steady state speed at a number of thrusts in benign environmental conditions, or taken from tables that are often provided with larger vessels. These thrust and speed pairs are used to create a thrust map that is supplied to the controller. Some examples of thrust maps for the vessels used in this research are given in Table 4.1

		Thrust				
	Vessel	0%	25%	50%	75%	100%
Speed [m/s]	Z-Boat	0	0.9	1.6	2.1	2.25
	ASV3	0	0.45	0.68	0.84	1.0

Table 4.1: Thrust to speed relationships of systems used in this thesis

4.3.1 Initial Setting Stage

The first stage of the control response is initiated when a new heading or speed is set by the helm, or when the vessel first runs. If it is the first time a speed has been set, the thrust is directly taken by linearly interpolating the desired speed from the thrust map. If the controller has been running, it will use the environmental effect estimate to compensate the speed.

The environmental effects are estimated from two different methods depending on available data. If the vessel has previously traveled within a threshold of the desired heading (10° by default), the average offset from the expected speed based on the thrust map is used. This accounts for effects that depend on the relative heading between the vessel and the disturbance, such as wind or waves.

If the vessel does not have any history of previous runs near the desired heading but has been operating on other headings, an estimate is made of the average effect of disturbances. This can again be done with two methods. If the positioning system provides a course over ground measurement in addition to heading, the average vector difference between the expected speed (from the thrust map or speed through the water measurement if available) at the heading, and speed over ground on the course over ground is used to find an average disturbance vector. The effect of this at the new heading is used to compensate the initial speed setting.

A final method is used if no course over ground signal is available. During operation, the speed difference from the thrust map value at the current heading is averaged into angular sector bins distributed at equal intervals around the compass, by default every 10°. The direction and magnitude of the disturbance are taken to be the heading bin with the maximum difference from expected speeds. In practice, this tends to give similar results, as the vector is oriented in the direction of greatest effect.

4.3.2 Coarse Adjustment

After the initial setting, the control system waits until the speed has reaches steady state to make any more adjustments. This is in contrast to a PID controller that continually adjusts based on the differences between desired and actual speeds. The first adjustment is based on an average speed over a short period of time selected as an averaging period (T_{avg}). For most small vessels a value of approximately $T_{avg} = 3\,\mathrm{s}$ performs well. A longer period is applicable to larger vessels since settling times are longer and they may have a throttle that takes time to adjust the actual engine output.

The time for the first adjustment is determined by when the average slope of the speed over a length of time is below a threshold. The time range for the slope is determined from a setting for how quickly an operator wishes the vessel to respond, and is set as $2T_{avg}$ by default. This threshold can be configured to account for sea state, as movement of the vessel in waves causes the speed to fluctuate even when it has been fully accelerated by the thrusters. For the Z-Boat, values of $0.05\,\mathrm{m/s^2}$ for calm seas and $0.10\,\mathrm{m/s^2}$ for 1-2 ft seas performed well.

In addition to ensuring the speed has reached a steady value, the controller does not make an adjustment until the heading is steady after a turn, which is defined as being within a configurable threshold for T_{avg}. A threshold of 10° works well for small vessels, and this may be set smaller for larger vessels which are less affected by environmental disturbances.

The amount of adjustment is based on the difference between the average speed for the last T_{avg} seconds and the desired speed. If the difference is within a configurable tolerance ($0.1\,\mathrm{m/s}$ used for testing), no adjustment is made. Otherwise, this difference is added to the initial speed setting and fed back into the thrust map to determine an offset thrust.

4.3.3 Fine Adjustments

Subsequent adjustments are spaced out by at least a time specified for the long adjustment period (T_{long}). T_{long} defaults to $5T_{avg}$, or can be set longer if frequent adjustments are not desired and a higher speed tolerance is acceptable. For further speed changes to take place, the heading and speed must also be steady as defined in Section 4.3.2.

Since the adjustments at this stage are intended to be small, it is assumed the vessel will settle within T_{avg}, so the average speed from the last $T_{long} - T_{avg}$ seconds is used for the difference from desired speed. Again, if this is within the set tolerance, no adjustment is made, otherwise the speed offset is again put into the thrust map to determine a new thrust. The thrust map is still used for these later adjustments because it is assumed that even if the exact value of the thrust to speed mapping is not correct (hence the need for adjustment), the slope of the measured relationship is close to the actual response of the vessel, so small changes will approximate the same change in

speed. This makes for more accurate adjustments on vessels that do not have a linear thrust map, which is the case for most physical systems, since drag increases nonlinearly with speed.

The states and adjustments discussed in this section are summarized in the state diagram in Figure 4.9. Note that a heading or speed change from the IvP Helm causes the controller to immediately generate a new required thrust estimate regardless of its current operation state.

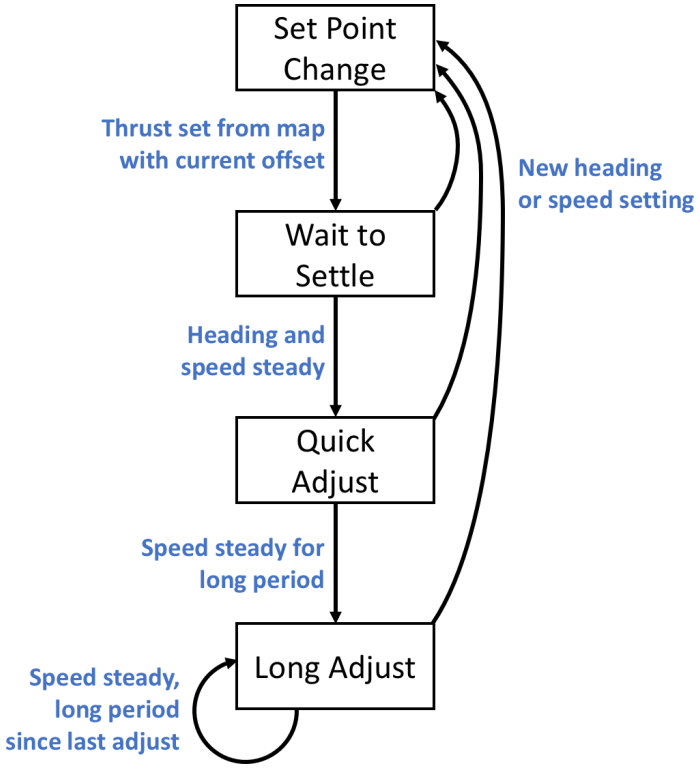

Figure 4.9: Averaging speed controller state diagram.

4.4 Control System Simulation Testing

Repeatedly testing the control system on vessels during development can be difficult since it requires excessive time and effort in addition to good environmental conditions. As a result, a simulator is developed based on the packaged MOOS-IvP simulator (uSimMarine). This core speed and heading propagation of the simulator were modified to use the Nomoto Model (Equation 4.21), in an effort to correspond more closely to actual vessel behavior. The ability to simulate waves and sensor noise is also added to increase the realism of tests. However, while the simulator provides a

useful tool for testing the qualitative performance of a controller, it is a marginal predictor of true vessel response.

4.4.1 Heading Control Tests

Both the course keep and course change controllers were tested separately and together in the hybrid mode. For small vessels, it is determined that use of the course change controller is not ideal and, therefore, the primary focus of additional refinements is the course keep only mode, where the MRAC determines the vessel model. The course change controller only uses adaptation while turning, and for small vessels, the turning times are not long enough for the adaptation to behave as desired without being overly sensitive to noise. For example, the Z-Boat can complete a 90° turn in 6 seconds, which does not allow enough time for accurate adaptation in the presence of waves and sensor noise.

Course Change Controller

The course change controller attempts to follow specified dynamics by adjusting K_p and K_d as explained in Section 4.2.1. For testing the 45 m ship characterized by Van Amerongen [2] (a model with a slower turn response) is used, allowing more time for the controller to adapt. An example of this for different damping ratios is shown in Figure 4.10.

The model transitions smoothly between the previous and new desired headings, and the course change controller adjusts PID gains to follow this curve. As expected, the model for the under damped case shows overshoot. The critically damped and the overdamped systems show no overshoot, with the overdamped system having a slower response. Due to the adjustments from the adaptation, all of the vessel headings exhibit overshoot, but the overshoot is minimized as the damping ratio increases as is expected. When the heading difference and rate of turn are small, as in the final stage of the vessel reaching the desired heading, even major adjustments of the PID control gains do not have much effect, since they are multiplied by small differences. This results in the setpoint overshoot, as the adaptation tends to oscillate about the correct value for the con-

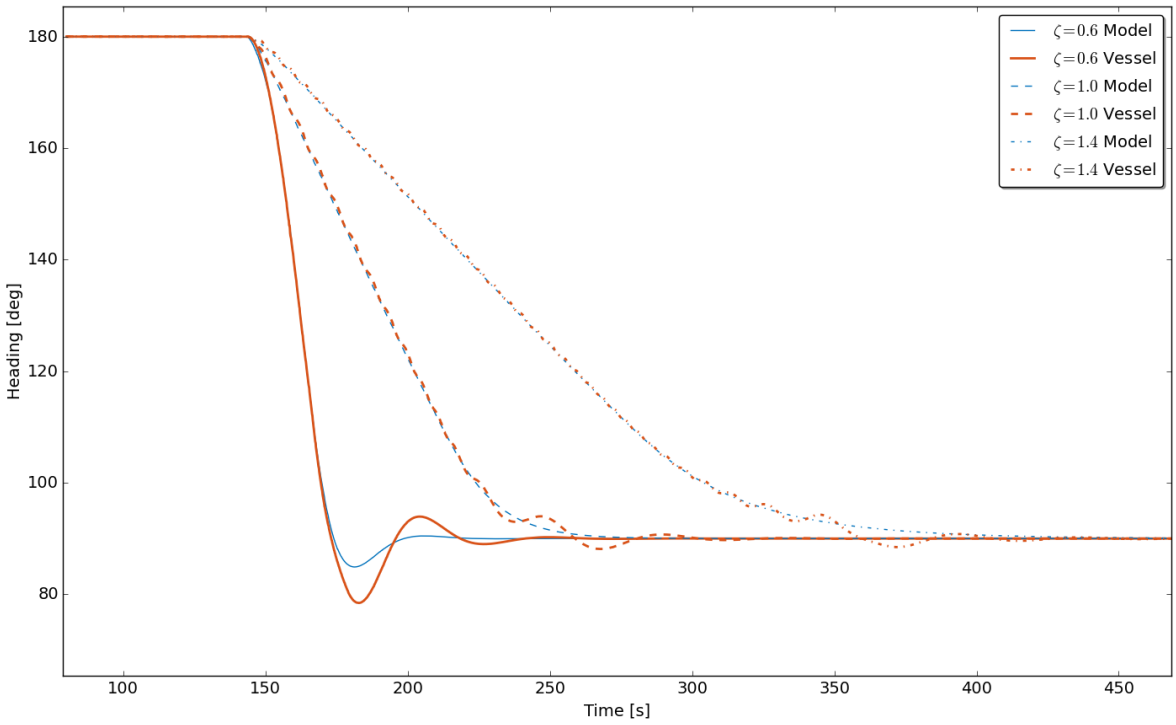

Figure 4.10: Course change controller maneuver with $\zeta = 0.6, 1.0, 1.4$

troller gains that would cause the vessel to exactly match the desired response due to the delay in vessel yaw response after rudder action.

The control gains over the same time period as Figure 4.10 for the $\zeta = 1.0$ case can be seen in Figure 4.11. K_i is not shown as there is no rudder offset in this simulation so it remains at zero. It is noted that the gains sometimes become negative. This phenomenon occurs when the ship is turning more quickly than its model, so the gains decrease in an attempt to slow the rate of turn. In the negative values cases, the rudder is actuated in the opposite direction from that necessary for the overall turn to reduce the rate of turn, bringing it back in line with the model. Since the overshoot and oscillation of the gains is due to the delay in response of the vessel compared to rudder angle, it is difficult to overcome this in the controller without dramatically reducing the adaptive gains α and β. However, the vessel then does not follow the model response as closely, so there is a trade off when choosing the adaptive gains. Limits to prevent the control gains from becoming negative are not seen to improve performance, so this behavior is permitted.

Some of the differences in response from various adaptive gains are shown in Figure 4.12.

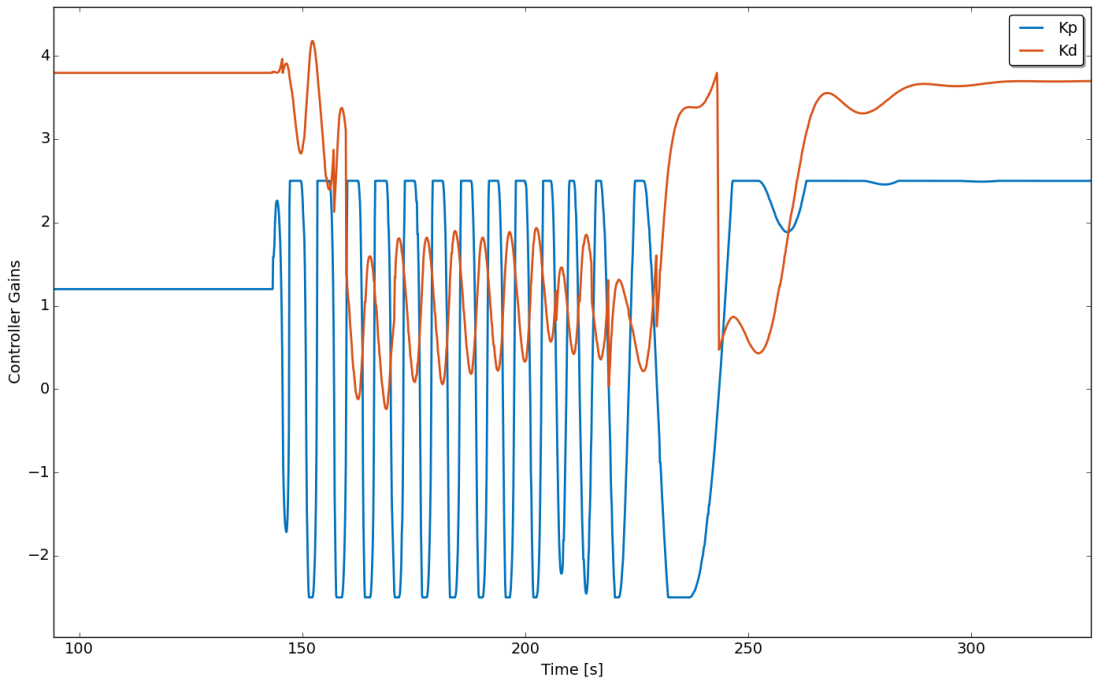

Figure 4.11: Adaptive parameters for course change controller maneuver with $\zeta = 1.0$.

It can be seen that higher adaptive gains lead to better model tracking at the expense of greater parameter oscillation and would, thus, not operate well in the presence of disturbances such as waves. These scenarios all use the same model constants and damping ratio, but higher adaptive gains also lead to a slower response. This is due to the effect of the series model discussed in Section 4.2.1. When desired rudder angles are larger than physically possible, which occurs when the PID gains oscillate through rapid adaptation, the series model slows the rate of turn of the course change model accordingly since it would otherwise respond more quickly than physically possible. However, when this oscillation is faster than the rate at which the rudder can turn, as is the case in the high adaptive gains, the reduction is incorrect and artificially slows the response.

The issues with speed of response in the course keep controller depending on adaptive gains and oscillation of parameters due to unaccounted time delays in the system lead to the course keep controller being the main focus of this research. The course change controller is also more applicable to vessels with slower turn response than small ASVs, as it restarts adaptation with each execution and quick turns provide little time to adapt, whereas the course change controller adapts

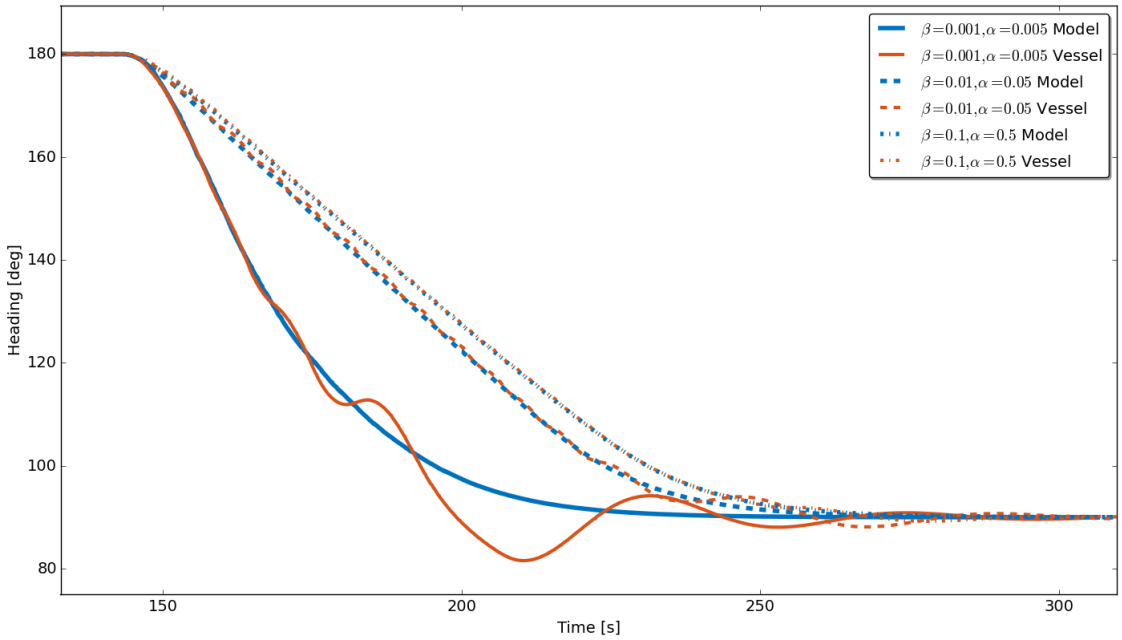

Figure 4.12: Effect of different magnitudes of adaptive gains

progressively over time.

Course Keep Controller

The course keep controller provides better overall control of small vessels since it characterizes the response and is able to use this to create both turns and straight areas that fit desired response characteristics. Many characteristics of the response can be tested under different conditions with the simulator and some examples are given here.

The adaptation behavior of the controller can be tested by starting it with known incorrect values of K^* and τ^*. Since the controller only adapts during turns and other large rudder angle maneuvers, the simulated vessel is instructed to run in an L shaped pattern with periodic turns greater than 80 degrees. An of adaptation is shown in Figure 4.13.

As expected from Equation 4.33, the final values for K_d when the controller has adapted are different for the different values of ζ. However, K_p does not have any dependence on ζ, so all of the parameters end near the same value. The spikes to large values of K_p and K_d near the beginning of the plot are caused by the low speed while the vessel is first accelerating and exceeds

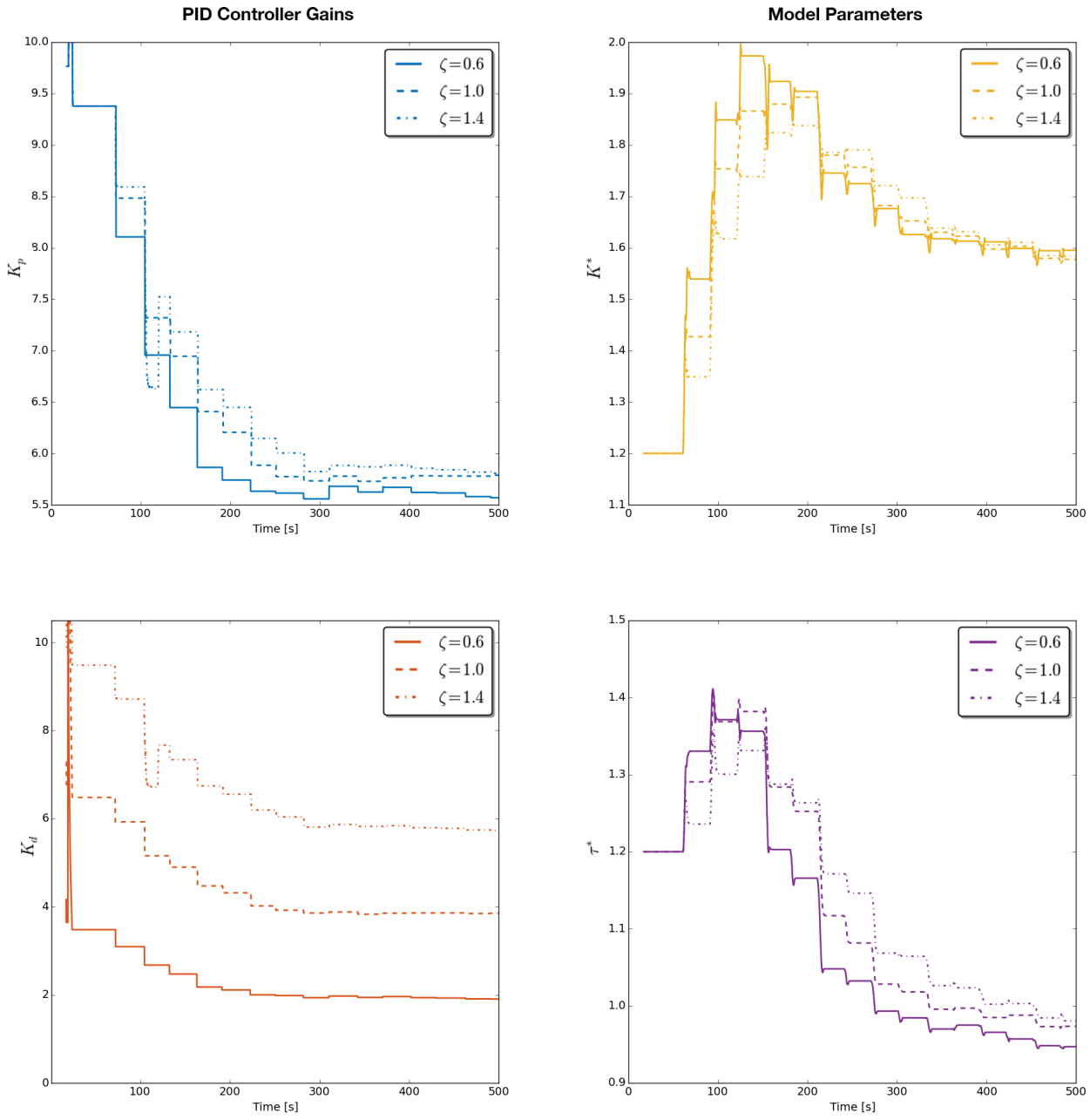

Figure 4.13: Adaptation of course keep controller with $\omega_n = 2.4$ and different values of ζ

the 0.5 m/s minimum. At slow speeds, more rudder is necessary to make turns, so this follows physical expectations. The values of K^* and τ^* all settle to similar values as would be expected with correct adaptation. The simulation vessel values for this example are $K^* = 1.56$ and $\tau^* = 0.8$.

The final response curves after adaptation are shown in Figure 4.14. The $\zeta = 0.6$ underdamped response shows overshoot as expected, and the $\zeta = 1.4$ overdamped case has the longest settling

time. Since all simulations use the same value for ω_n, they all have similar settling times with the variation mostly coming from the damping, as expected. Rudder output from the controller is included in the plot to show how the responses differ in their application of counter rudder to slow the turn while approaching the desired heading. Larger values of ζ lead to earlier application of counter rudder, and less magnitude is then necessary to stop the turn at the desired heading.

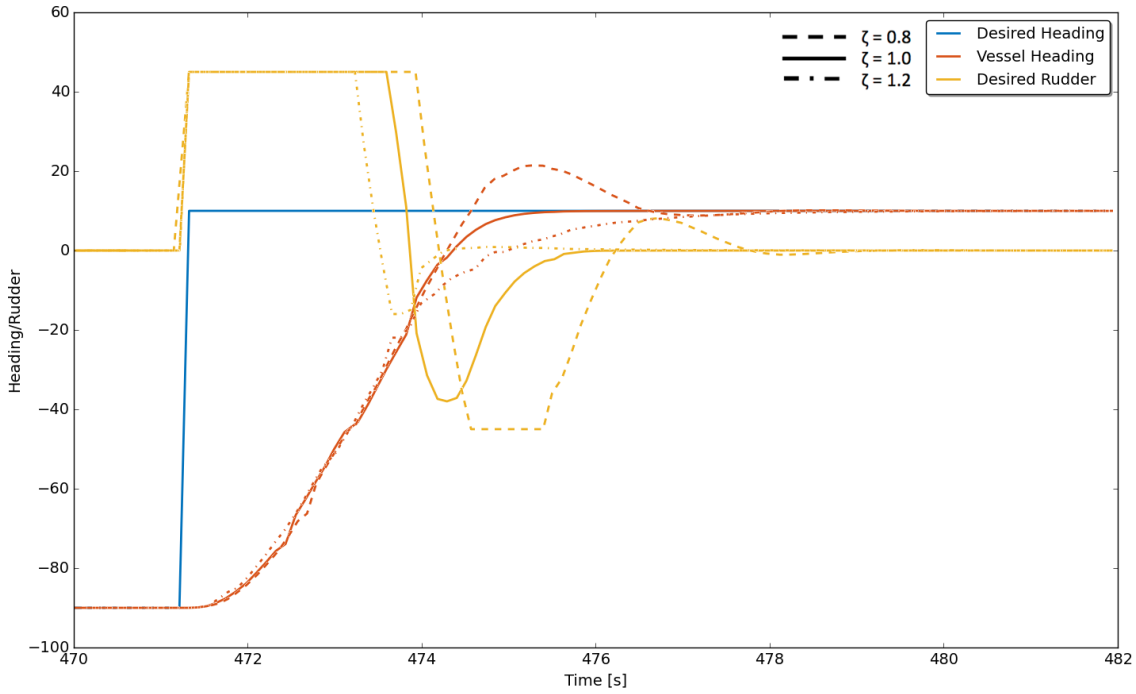

Figure 4.14: Controlled heading response for turns $\omega_n = 2.4$ and different values of ζ

In addition to adapting K_p and K_d when the model parameters are incorrect, K_i adapts if there is a consistent rate of turn offset from that expected by the rudder angle, such as if there is a physical offset or consistent wind. An example plot, with an initial simulated rudder offset of 5° is shown in Figure 4.15.

While the adaptation works properly under these ideal conditions, where the simulator does not have sensor noise or any environmental conditions, it does not test the performance in real world conditions.

To improve performance under simulated noisy sensor conditions and in the real world, a low pass filter is run for the rate of turn determination. Both the noisy signal and filtered version are shown in Figure 4.16. This filter uses a cutoff frequency applicable to the vessels tested of 0.25 Hz.

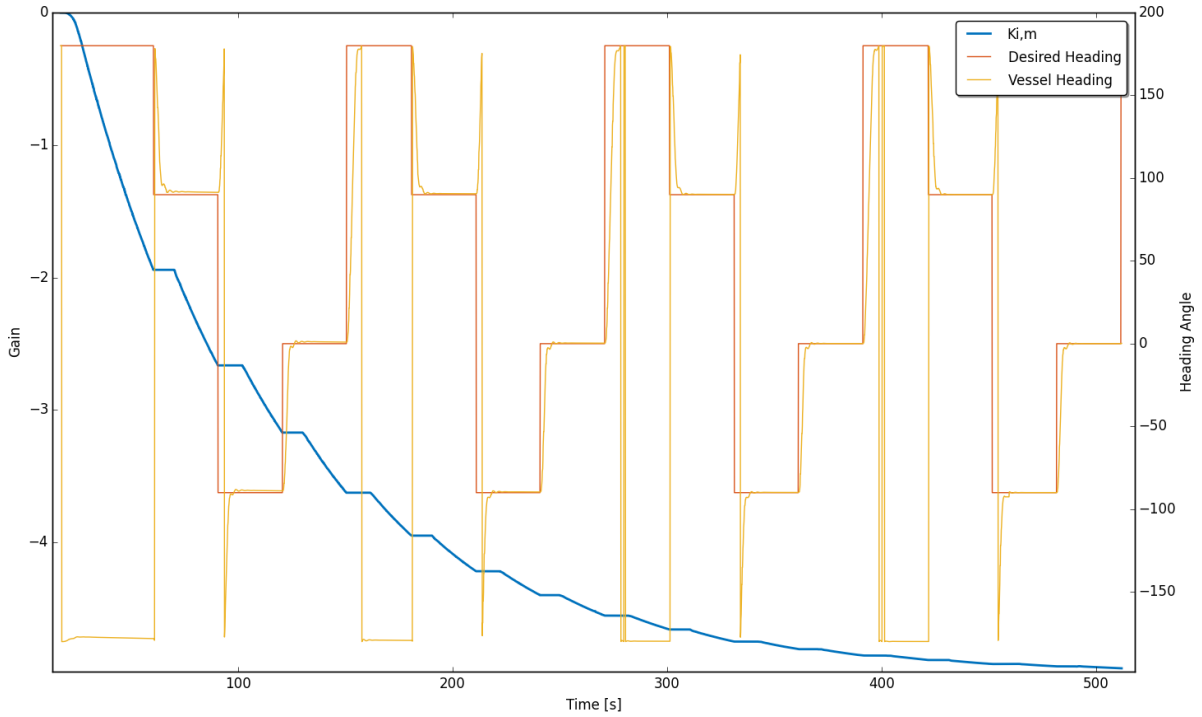

Figure 4.15: Adaptation of K_i with rudder offset of 5°

Note that waves are also present in this simulation and are still visible in the signal after filtering. As with any real-time filter, a delay is introduced, but this is somewhat compensated for by also delaying the model signal before comparison in the adaptation process.

All of the simulation effects can be combined to give an idea of how the system will operate on a vessel. An example is shown in Figure 4.17. It can be observed that $K_{i,m}$ adapts quickly and smoothly, while the other parameters are more affected by the speed changes from the waves. The parameters for the simulation model in this case were Rudder Offset = -5, $K^* = 1.6$ and $\tau^* = 0.8$. By the end of the simulation, the rudder offset has been correctly compensated by $K_{i,m}$ and K^* trends toward the correct value. The time constant τ^* adapts to a slightly larger value than that of the model, likely as a result of the limited rudder speed in the model, which effectively increases τ_s. This effect would be present on real vessels as well.

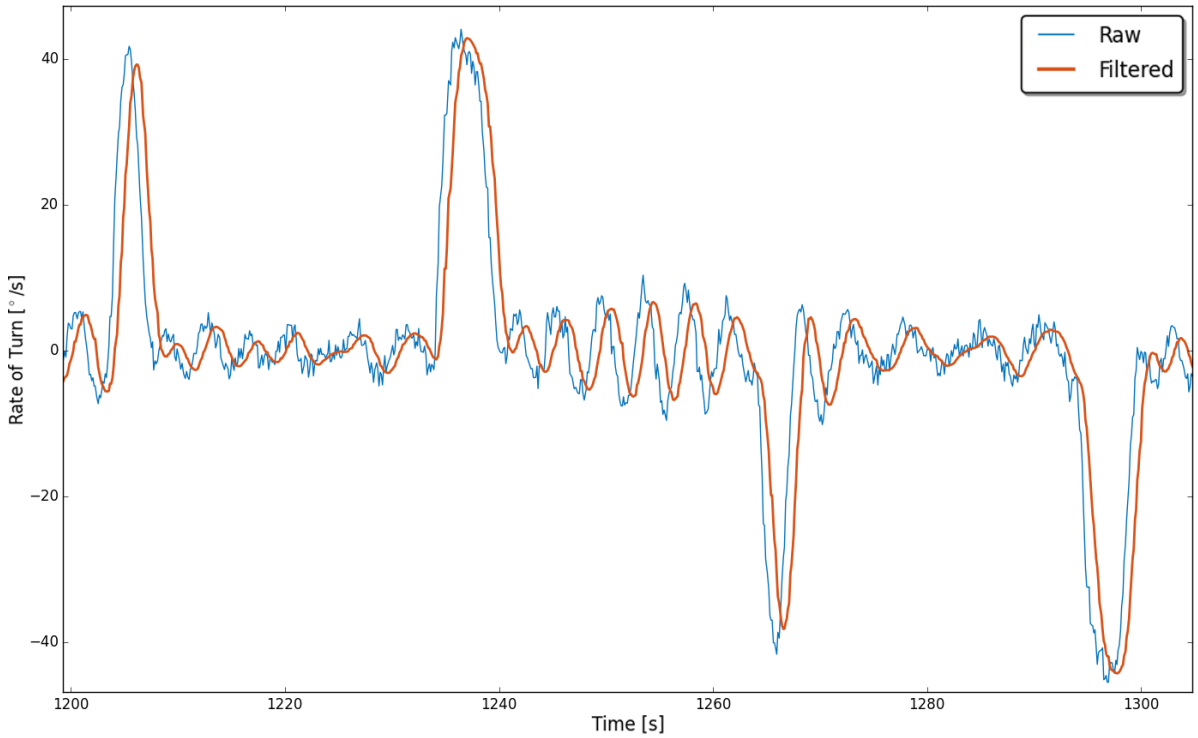

Figure 4.16: Simulated noise and low pass filtered rate of turn

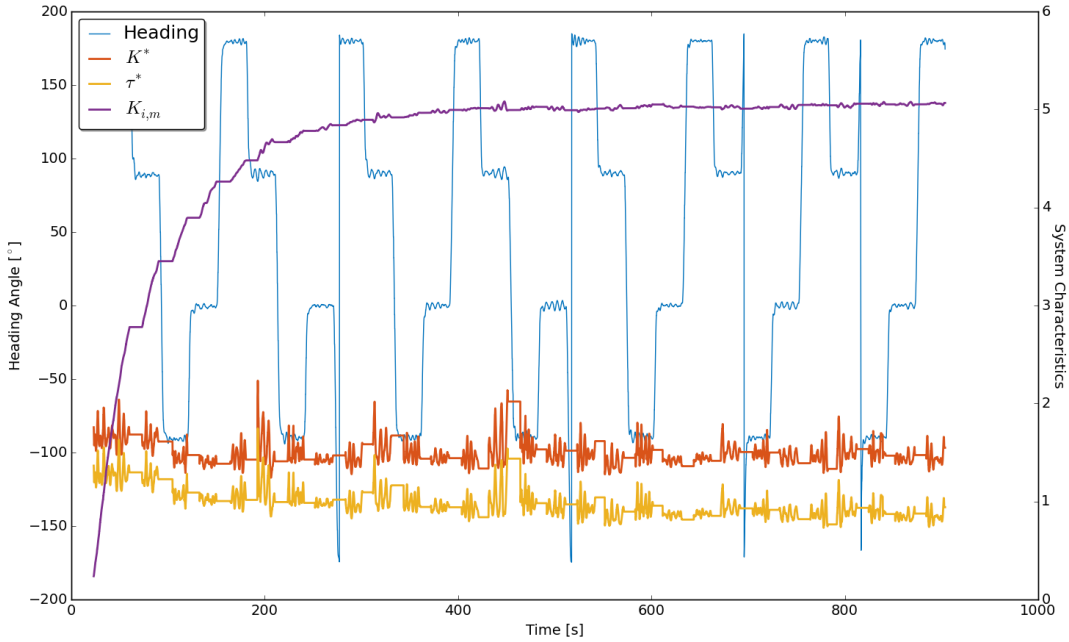

Figure 4.17: Full conditions simulation, including waves, rudder offset and sensor noise

4.4.2 Speed Control Tests

The speed control system is also tested using the same simulation architecture. When compared to a standard PID controller, it creates many fewer setpoint adjustments and also does not react to transient effects. A comparison with a PID controller is shown in Figure 4.18. In this scenario, speed changes result from turns and cause the PID controller to respond, but the survey controller anticipates the speed after the turn and does not run faster than necessary through the turn. This eliminates the spikes in thrust seen in the PID controller example, increasing battery life. In addition, the controller developed in this research does not respond unnecessarily to temporary fluctuations due to waves, while still maintaining a speed within $0.2\,\mathrm{m/s^2}$

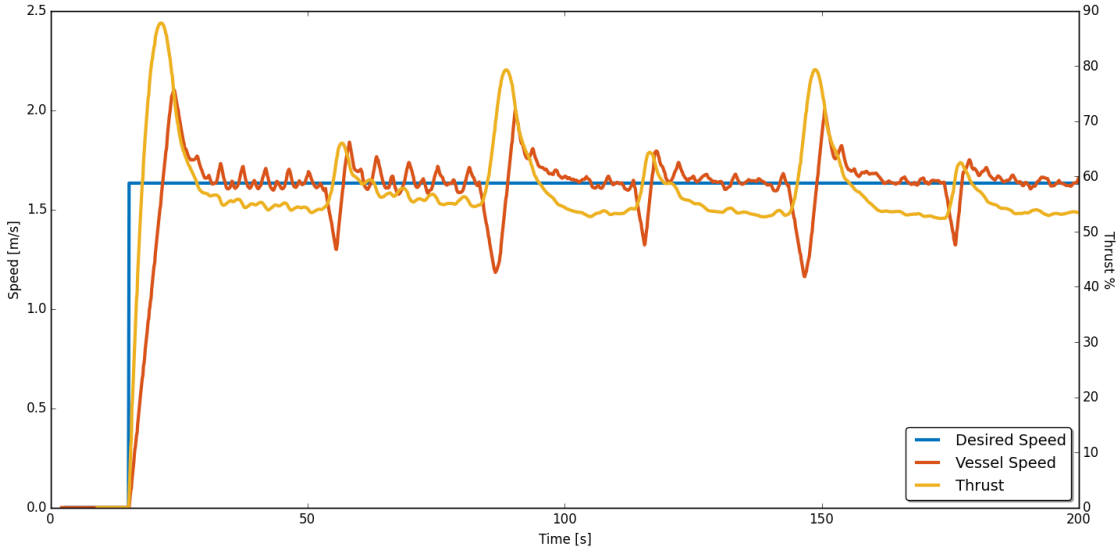

(a) PID controlled speed

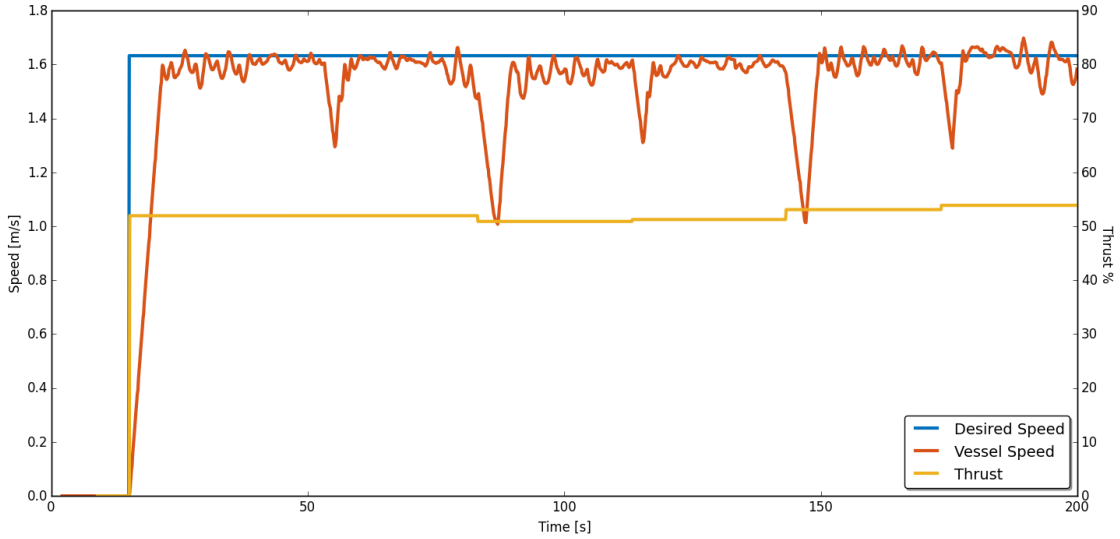

(b) Custom controller speed

Figure 4.18: Speed control comparison with waves and vessel turns but no currents in simulation

Currents can also be added to the simulation, letting the directional offset estimator be tested, as shown in Figure 4.19. While minor adjustments are needed after the first couple of turns, the current is anticipated afterwards and avoids the need to constantly compensate as in the case of the PID controller. This test operates on the same L-Shaped pattern as the previous example, so currents are increased or decreased with each turn.

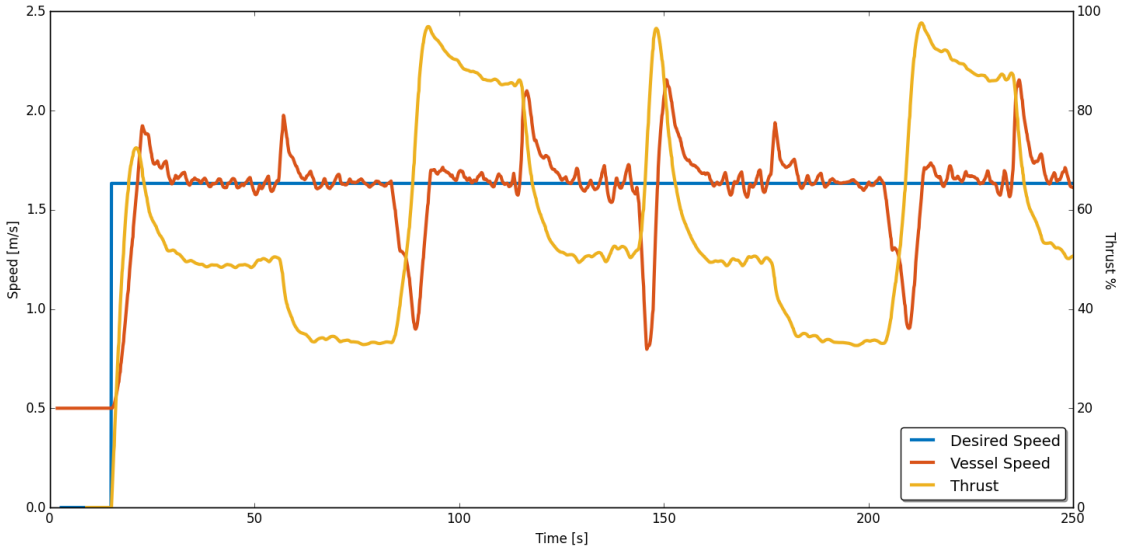

(a) PID controlled speed

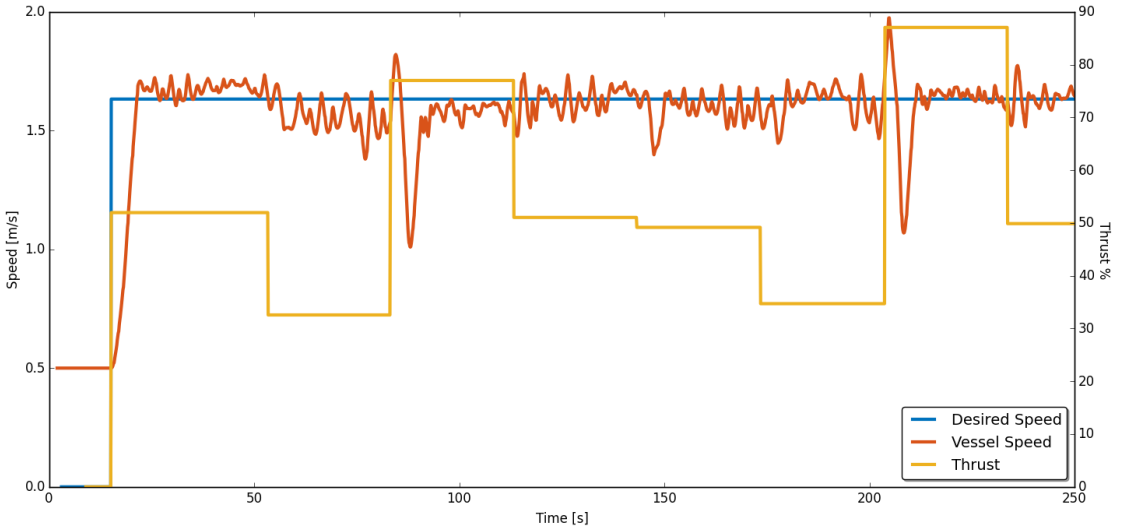

(b) Custom controller speed

Figure 4.19: Speed control comparison with waves, currents, and vessel turns in simulation

4.5 Field Tests

Due to limited ASV availability and hardware issues with vessels at UNH, only limited field tests were performed. A Z-Boat from NOAA Ship *Thomas Jefferson* was available for some initial control system tests and operations on UNH ASV3 were attempted but unsuccessful due to hardware failures in the propulsion system and rough environmental conditions. The Z-Boats transitioned to

consistent operational use and were also unavailable for final tests.

4.5.1 Rate-of-Turn Characterization

Both the UNH ASV3 and the Z-Boat were first operated at a variety of thrust and rudder settings to determine an approximate K^* and τ^* values for the control system. The results for the Z-Boat are shown in Figure 4.20. The two plots are different ways to visualize the same data and illustrate that both thrust and rudder have essentially linear effects on the rate of turn. Linear trend lines are shown as the dotted lines in Figure 4.20. This linear response validates the use of the simple Nomoto Model and the speed scaling of the K_s and τ_s per Equation 4.23. Since the vessel responds in the same manner as the model, the model reference adaptive system is expected to function correctly.

The ROT test is also conducted on the UNH ASV3, with the results shown in Figure 4.21. The response is fairly linear to 75% rudder, after which the rate of turn does not appreciably increase. There is also minimal variation with thrust. Both of these effects may be partially accounted for by the use of an old, degraded battery on ASV3 at the time of the tests. Unusual behavior resulted from the inability of the battery to provide high currents, including undesired rudder movements at high angles, so this test would likely present results more similar to the Z-Boat if rerun with the replacement batteries that have since been installed.

From the data for these rate of turn plots, the value of K_s can be calculated for each thrust and rudder pair, then Equation 4.23 is used to find K^*. Similarly, the time response of the vessel can be analyzed from logged data and the value of τ^* determined. Average values for these model constants are given in Table 4.2. Both vessels have similar values of the uncompensated (starred) parameters, but the differences in size and speed of the platform dictate the actual vessel response. As expected for its larger size and slower speed, under normal operation ASV3 turns more slowly than a Z-Boat.

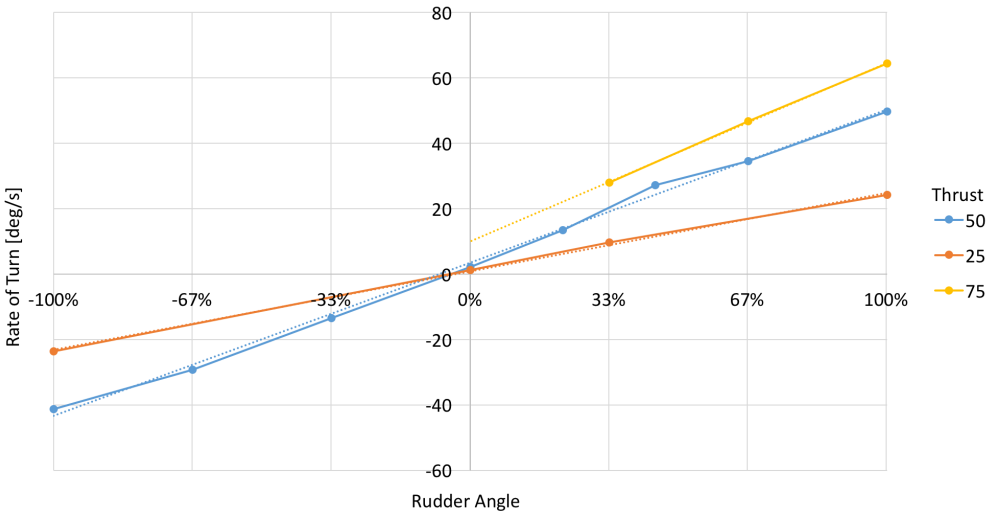

(a) Z-Boat rate-of-turn versus rudder angle at various thrusts

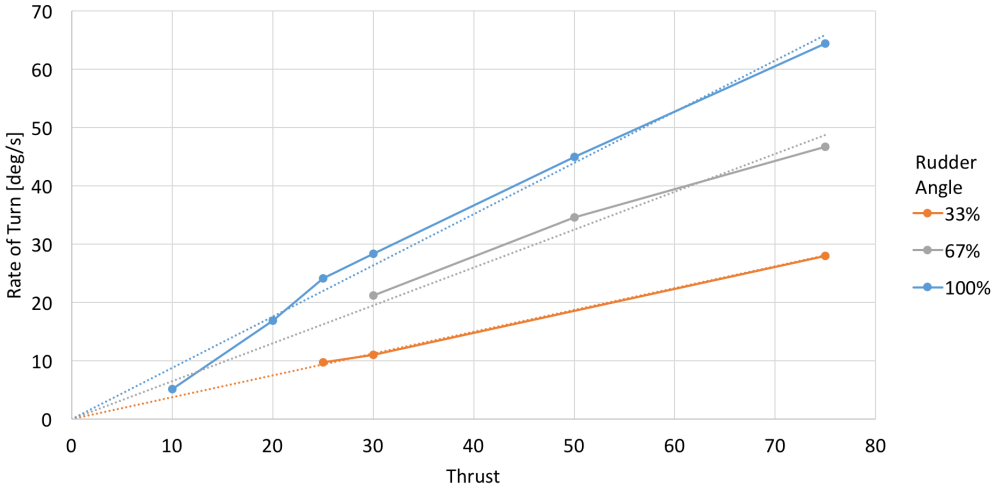

(b) Z-Boat rate-of-turn versus thrust at different rudder angles

Figure 4.20: Z-Boat rate-of-turn effects from rudder and thrust settings

Vessel	K^*	τ^*	Operation Length [m]	Operation Speed [m/s]	$K_{p,s}$	τ_s
Z-Boat 1800	1.3	0.6	1.8	1.6	1.1	0.7
UNH ASV3	1.8	0.5	2.9	0.7	0.4	2.0

Table 4.2: Measured vessel response characteristics

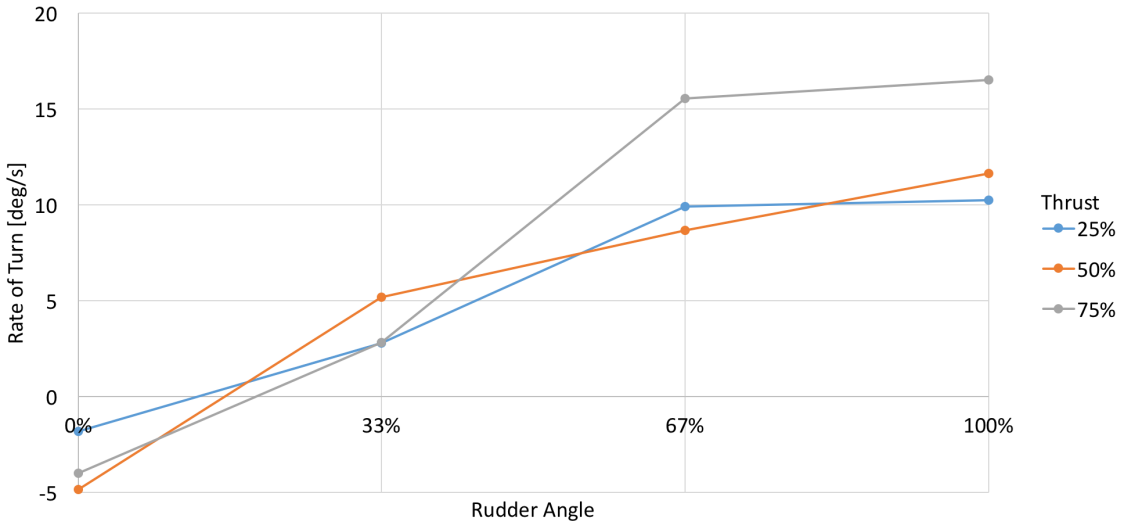

Figure 4.21: ASV3 rate-of-turn response to rudder angle and thrust

4.5.2 Course Change Controller Field Test

A preliminary version of the course change controller was tested remotely on a Z-Boat in Norfolk, VA on January 20, 2016. The result for a single turn is shown in Figure 4.22. In this instance, the response of the vessel is not as fast as the MRAS model, so the value of K_p increases as the turn progresses, but does not adapt quickly enough for the vessel to more closely follow the model. Decreasing adaptive gains, as specified in Equation 4.20, with $\xi = 0.9$ were used in this test. As a result, the PID gains are seen to change less rapidly over time.

During this field test, the course keep controller is also tested through the use of the hybrid arrangement. However, mathematical errors in the controller implementation at the time of testing prevented the vessel from fully behaving as desired. Despite this, the results of early tests on Z-Boats led to the sole use of the course keep controller to achieve the best performance. Due to the hardware limitations mentioned previously, tests on the final controller were not possible.

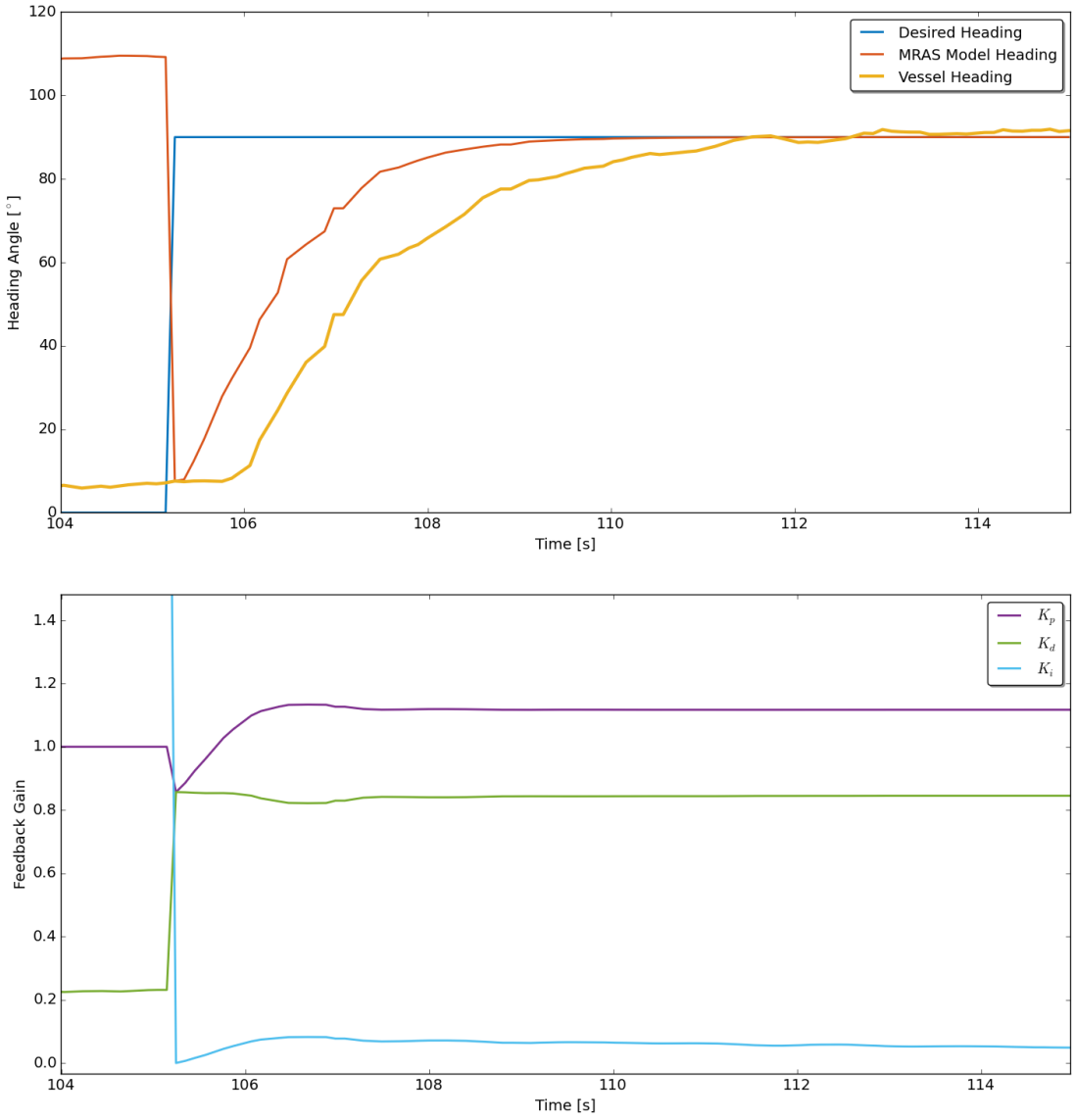

Figure 4.22: Course change controller field test, showing heading and PID feedback gains during a 90° turn.

CONCLUSION AND FUTURE WORK

Summary of Research

A complete package for autonomous marine operations, focused on executing hydrographic surveys, is developed in this research. A hardware and electronics system, capable of being packaged for integration on vessels of opportunity provides flexibility for deployment. This system provides full autonomous functionality and the ability for a human operator to monitor or manually control the vessel when desired, and can be entirely constructed for under $1200. Core autonomy functionality is provided by the open source MOOS-IvP framework, with additional applications supporting integration on multiple platforms.

A new approach to autonomous hydrographic survey line planning is developed that provides full bottom coverage when used in conjunction with a swath sonar system. This system was field tested on multiple Z-Boat platforms with positive results. Simulations show expected performance on a variety of terrains when compared to human surveys of the same areas.

The Model Reference Adaptive Control system is able to determine model parameters for a simplified vessel, which show promising application for the control of small ASVs in simulation and field tests. A second controller performs controlled turns for larger vessels, and can be used in conjunction with the model identification controller for reduced rudder actuation while course keeping. Specialized speed control for applications where constant adjustment is unneeded increases power efficiency while still maintaining speeds within a designated threshold

Together, these components form an autonomy and data acquisition system that can be easily deployed in the field for rapid survey operations in shallow water with small ASVs. The modular nature of the system permits installation on a range of vessels and much of the research is also applicable to large ships and high integrity sensors.

Future Work

The control system and survey path planning aspects of this research present opportunities for improvement. The path planning algorithm could be extended to automatically partition larger irregular polygons, which would further simplify the human planning element. The behavior when isolated shallow areas are located could be improved to deal with them in a more systematic manner, instead of halting progress on the survey in that area. More work could be done on optimal path refinement and processing of the sonar data, particularly in regions with greatly varying depths that lead to significant repeated bends in survey lines.

The control system could be extended with a fuzzy logic intelligence or neural network, as other research has investigated in relation to MRAC. Frequency analysis of the heading history could provide diagnostics and removal of unwanted oscillation. The speed based gain scheduling of system parameters could be improved, as this does not appear to always be a linear effect. In addition, the speed control could be better applied to fault detection through analysis of long term speed trends and comparison with expected behavior. More field testing is required for refinement of the controllers, as well as testing on a wider range of vessel sizes and types.

In order for any component of the autonomy system to be more accessible to an unfamiliar user, an improved graphical interface and configuration tools will need to be developed. Some work has begun in this effort, including work toward universal mission planning file structures and visual mission planning tools.

LIST OF REFERENCES

[1] B. S. Bourgeois, D. L. Brandon Jr *et al.*, "Efficient hydrographic survey planning using an environmentally adaptive approach," DTIC Document, Tech. Rep., 2006.

[2] J. Van Amerongen, "Adaptive Steering of Ships," Ph.D. dissertation, Delft University of Technology, 1982.

[3] A. Motwani, "A Survey of Uninhabited Surface Vehicles," Tech. Rep., 2012.

[4] G. Roberts, R. Sutton *et al.*, "Intelligent ship autopilotsA historical perspective," *Mechatronics*, vol. 13, pp. 1091–1103, 2003.

[5] S. Bennett, "Nicolas Minorsky and the Automatic Steering of Ships," *IEEE Control Systems Magazine*, vol. 4, no. 4, pp. 10–15, 1984.

[6] V. Bertram, "Unmanned Surface Vehicles A Survey," *Skibsteknisk Selskab, Copenhagen, Denmark*, pp. 1–14, 2008. [Online]. Available: http://www.skibsteknisk selskab.dk/public/dokumenter/Skibsteknisk/Downloadmateriale/2008/10marts08/USVsurvey{_}DTU.pdf

[7] ASV Global. C-worker 6. ASV Global. [Online]. Available: http://asvglobal.com/product/c-worker-6/

[8] Teledyne Oceanscience. Z-boat 1800-rp. Teledyne Oceanscience. [Online]. Available: http://oceanscience.com/Products/Z-Boat/Z-Boat-RP.aspx

[9] J. Manley and S. Willcox, "The Wave Glider: A persistent platform for ocean science," in *OCEANS 2010 IEEE - Sydney*. IEEE, May 2010, pp. 1–5.

[10] C. Meinig, N. Lawrence-Slavas *et al.*, "The use of saildrones to examine spring conditions in the bering sea: Vehicle specification and mission performance," in *OCEANS'15 MTS/IEEE Washington*. IEEE, 2015, pp. 1–6.

[11] K. Woerner, "COLREGS-Compliant Autonomous Collision Avoidance Using Multi-Objective Optimization with Interval Programming by," Ph.D. dissertation, Massachusets Institute of Technology, 2014.

[12] Y. Kuwata, M. T. Wolf *et al.*, "Safe Maritime Autonomous Navigation With COLREGS , Using Velocity Obstacles," *IEEE Journal of Oceanic Engineering*, vol. 39, no. 1, pp. 110–119, 2014.

[13] P. Svec, B. C. Shah *et al.*, "Dynamics-aware target following for an autonomous surface vehicle operating under COLREGs in civilian traffic," *IEEE International Conference on Intelligent Robots and Systems*, pp. 3871–3878, 2013.

[14] L. P. Perera, J. P. Carvalho, and C. Guedes Soares, "Autonomous guidance and navigation based on the COLREGs rules and regulations of collision avoidance ." *Advanced Ship Design for Pollution Prevention*, no. 1999, pp. 205–216, 2010.

[15] U. Siwe. (2016) Sea Traffic Management. The Swedish Maritime Administration. [Online]. Available: http://www.stmvalidation.eu

[16] Rolls-Royce. (2016) Rolls-Royce reveals future shore control centre. Rolls-Royce. [Online]. Available: http://www.rolls-royce.com/media/press-releases/yr-2016/pr-2016-03-22-rr-reveals-future-shore-control-centre.aspx

[17] D. W. Hodo, D. M. Bevly *et al.*, "Optimal path planning with obstacle avoidance for autonomous surveying," in *IECON 2010-36th Annual Conference on IEEE Industrial Electronics Society*. IEEE, 2010, pp. 1577–1583.

[18] E. Galceran and M. Carreras, "Efficient seabed coverage path planning for asvs and auvs," in *Intelligent Robots and Systems (IROS), 2012 IEEE/RSJ International Conference on*. IEEE, 2012, pp. 88–93.

[19] T. Wilson and S. B. Williams, "Adaptive Path Planning for Depth Constrained Bathymetric Mapping with an Autonomous Surface Vessel," 2016. [Online]. Available: http://arxiv.org/abs/1603.06324

[20] Hydronalix EMILY. Hurricane tracker. Hydronalix. [Online]. Available: http://emilyrobot.com/hurricane-tracker

[21] M. Head, S. Smith, and D. Manda, "Into the Blue (Tint): Unmanned Survey Boats Complement Multibeam, Lidar, and Satellite Derived Bathymetry on the NOAA Ship Thomas Jefferson," in *Canadian Hydrographic Conference - Halifax, NS*. Canadian Hydrographic Conference, May 2016.

[22] Bass Hunter. EX. Bass Hunter. [Online]. Available: http://www.basshunter.com/index.php?option=com_content&view=article&id=11

[23] J. Perrella, T. Panella *et al.*, "Autonomous surface vehicle senior research project."

[24] Raspberry Pi Foundation. Raspberry Pi 2 Model B. [Online]. Available: https://www.raspberrypi.org/products/raspberry-pi-2-model-b/

[25] Arduino. Arduino mega 2560. [Online]. Available: http://arduino.cc/en/Main/ArduinoBoardMega2560

[26] K. Parsons. MCS Index for 802.11n and 802.11ac Chart. [Online]. Available: http://www.wlanpros.com/mcs-index-802-11n-802-11ac-chart

[27] CHRobotics LLC. GP9 GPS-Aided AHRS Datasheet, Revision 1.3. [Online]. Available: http://www.chrobotics.com/docs/GP9Datasheet.pdf

[28] C. Chamberlain, personal communication.

[29] International Hydrographic Bureau, *IHO Standards for Hydrographic Surveys, 5th Edition*, International Hydrographic Organization. [Online]. Available: http://www.iho.int/iho_pubs/standard/S-44_5E.pdf

[30] SBG Systems, "Hydrographic Test Result: Ellipse, Ekinox," SBG Systems, Tech. Rep., 2015. [Online]. Available: http://www.sbg-systems.com/docs/Ellipse_Ekinox_Test_Hydrography.pdf

[31] M. Benjamin, H. Schmidt, and P. Newman. (2015, May) An Overview of MOOS-IvP and a Users Guide to the IvP Helm - Release 15.5. MIT. [Online]. Available: http://oceanai.mit.edu/ivpman/pmwiki/pmwiki.php

[32] J. Velagic, Z. Vukic, and E. Omerdic, "Adaptive fuzzy ship autopilot for track-keeping," *Control Engineering Practice*, vol. 11, no. 4, pp. 433–443, 2003.

[33] B. T. Boulter, "Digital Filter Design Writing Difference Equations For Digital Filters," 2000. [Online]. Available: http://www.apicsllc.com/apics/Sr{_}3/Sr{_}3.htm

[34] T. Perez and T. Fossen, "Modelling and Simulation of Environmental Disturbances," Bol, Croatia, 2007. [Online]. Available: http://www.marinecontrol.org/pdf/Tutorial/CAMS{_}M5{_}disturbances.pdf

[35] National Oceanic and Atmospheric Administration, *NOS Hydrographic Surveys Specifications and Deliverables*, May 2015.

[36] Spatial Integrated Systems, Inc, "Demonstration of autonomous maritime navigation (amn) in support of noaa surveying missions," Spatial Integrated Systems, Inc, Technical Report, March 2012.

[37] C. Fang and S. Anstee, "Coverage path planning for harbour seabed surveys using an autonomous underwater vehicle," in *OCEANS 2010 IEEE-Sydney*. IEEE, 2010, pp. 1–8.

[38] B. S. Bourgeois, P. J. Alleman *et al.*, "Autonomous bathymetry survey system," *Oceanic Engineering, IEEE Journal of*, vol. 24, no. 4, pp. 414–423, 1999.

[39] K. Wylie and T. Ketter, "Summer hydrographic field course 2014," University of New Hampshire, Descriptive Report, July 2014.

[40] D. Manda, O. Irish *et al.*, "Summer hydrographic field course 2015," University of New Hampshire, Descriptive Report, July 2015.

[41] J. Van Amerongen, "MRAS: Model Reference Adaptive Systems," *Journal A*, vol. 22, no. 4, pp. 192–198, 1981.

[42] ——, "Adaptive steering of ships: A model reference approach," *Automatica*, vol. 20, no. 1, pp. 3–14, jan 1984. [Online]. Available: http://www.sciencedirect.com/science/article/pii/0005109884900608

[43] K. Nomoto, T. Taguchi *et al.*, "On the steering qualities of ships," *Int. Shipbuilding Progress*, vol. 4, 1957.